Alma Mater Studiorum – Università di Bologna

DOTTORATO DI RICERCA IN
INGEGNERIA BIOMEDICA, ELETTRICA E DEI SISTEMI

Ciclo 35

Settore Concorsuale: 09/G2 - BIOINGEGNERIA

Settore Scientifico Disciplinare: ING-INF/06 - BIOINGEGNERIA ELETTRONICA E INFORMATICA

COMPUTATIONAL MODELING OF HUMAN ATRIAL CARDIOMYOCYTES: INTEGRATION OF ELECTRO-MECHANICAL & MECHANO-ELECTRIC FEEDBACK PATHWAYS

Presentata da: Fazeelat Mazhar

Coordinatore Dottorato

Michele Monaci

Supervisore

Stefano Severi

Co-Supervisore

Cristiana Corsi

Esame finale anno 2023

This page is left black intentionally

Acknowledgments

Words cannot express my gratitude to all those people who supported me during the time of my PhD and made this thesis possible.

I am deeply indebeted to have a supervisor like Dr. Stefano Severi, who mentored me and lifted me up. I am extremely thankful for his invaluable guidance, continuous support and patience during my PhD study. He was the one who transformed my thinking from merely gathering knowledge to creating knowledge and taught me learning from others. I am also grateful to my co-supervisor, Dr. Cristiana Corsi, it was her level of dedication towards research from which I learnt to be an enthusiastic researcher.

I would like to express my deepest gratitude to the reviewers of this thesis and to my PhD committee members for their valuable suggestions that helped me to refine my research.

I would like to acknowledge my collaborators from Politecnico di Milano, Dr. Francesco Regazzoni, Dr. Luca Dedè, and Prof. Alfio Quarteroni for sharing their expert level of knowledge with me. Many thanks to Dr. Michelngelo Paci for sharing his knowledge, ideas and spending his time on useful discussions.

I will extend my sincere thanks to my colleague and friend Dr. Chiara Bartolucci, she was always available for guiding me and improving my basic knowledge.

Lastly, I would like to mention that I started my PhD during the peak COVID era that caused unplanned delay to the work. It was a hard time to survive while leaving my 3 months old daughter behind in my country. I could not have undertaken this journey without the support of my husband, Muhammad Arslan Munir and my family.

Keywords

Computational modeling

Electrophysiology

Contraction

Human atrial cardiomyocytes

Stretch activated currents

Integration

Mechano electric feedback

Table of Content

List of Abbreviations

AF	Atrial fibrillation
ANM	Alternans normalized magnitude
AP	Action potential
APD	Action potential duration
AV	Atrio-ventricular node
BB	Bachman bundles
BC	Bulk cytosol
BCL	Basic cycle length
cAF	Chronic atrial fibrillation
CaMKII	Ca/Calmodulin dependent kinase II
CaT	Ca^{2+}-transient
CDI	Calcium dependent inactivation
CE	Contractile element
CG	Cheng 2014
CICR	Calcium Induced Calcium release
CMDN	Calmodulin
CMs	Cardiomyocytes
CRN	Courtemanche 1998
CS	Coronary sinus
CT	Crista terminalis
CTMC	Contonous-time Markov Chains
CV	Conduction velocity
DADs	Delayed afterdepolarization

DF	Driving force
EADs	Early afterdepolarization
EM	Electro-mechanical
EM	Ellinwood 2017
EP	Electrophysiology
ERP	Effective refractory period
FDAR	Frequency dependent acceleration of relaxation
FDUF	Fire diffuse uptake fire
GB	Grandi 2011
HF	Heart failure
ICV	Inferior caval vein
KM	Koivumaki 2011
LA	Left atria
LAA	Left atrial appendage
LAVi	LA volume indexed to body surface area
LI	Left inferior
LRd	Luo-Rudy
LS	Left superior
LV	Left ventricular
MACs	Mechano-activated channels
MCF	Mechano-calcium feedback
MEF	Mechano-electric feedback
MHCs	Myosin Heavy chains
MLCs	Myosin Light chains
MMCs	Mechano-modulated channels
NSO	Non-single Overlap Zone
ODEs	Ordinary differential equations

ORd	O'hara rudy
PB	Priebe-beuckelmann
PE	Parallel element
PKA	Protein kinase a
PLB	Phospholamban
PM	Pectinate muscles
PoAF	Post-operative Atrial Fibrillation
PP	Plateau potential
PVs	Pulmonary veins
RA	Right atria
RDQ-MF	Regazzoni dede quarteroni-mean field
RI	Right inferior
RMP	Resting membrane potential
RS	Right superior
rt	Relaxation time
RU	Regulatory unit
SAC	Stretch activated channels
SAC_k	K^+ selective stretch activated channels
SAC_{NS}	Non-selective stretch activated channels
SAN	Sino-atrial node
SCV	Superior caval vein
SE	Series element
SERCA	Sarcoplasmic Reticulum atpase
SL	Sarcomere length
SO	Single overlap zone
SR	Sarcoplasmic reticulum
SS	Subspace

T_{ca}	Total time
Tm	Tropomyosin
ToR-ORd	Tomek-ORd
Tr	Trachea
TRPN	Troponin
TT	Twitch time
TTP	Ten Tusscher Panfilov
ttp	Time to peak
VDI	Voltage dependent Inactivation
VOCs	Voltage operated Ca^{2+} channels
XB	Cross bridge
Xb_{cy}	Cross bridge cycling

Thesis Introduction

Abstract

The cardiomyocytes are very complex consisting of many interlinked non-linear regulatory mechanisms between electrical excitation and mechanical contraction. Thus given a integrated electromechanically coupled system it becomes hard to understand the individual contributor of cardiac electrics and mechanics under both physiological and pathological conditions. Hence, to identify the causal relationship or to predict the responses in a integrated system the use of computational modeling can be beneficial. Computational modeling is a powerful tool that provides complete control of parameters along with the visibility of all the individual components of the integrated system. The advancement of computational power has made it possible to simulate the models in a short timeframe, providing the possibility of increased predictive power of the integrated system. My doctoral thesis is focused on the development of electromechanically integrated human atrial cardiomyocyte model with proper consideration of feedforward and feedback pathways. In particular, the thesis compiles following findings:

1) Coupling of the existing human atrial action potential (AP) models with available contraction models and highlighting their rate dependent characteristics. Analyzing the AP models, we also identified the dependence of extracellular Ca^{2+} variation on the intracellular Ca^{2+} homeostasis.

2) We proposed a novel electromechanically coupled human atrial cardiomyocyte model that has been calibrated and validated with a wide range of human atrial experimental data. The model demonstrates the effect of CaMKII based phosphorylation for atrial specific targets. The model highlights the insight mechanisms behind the biphasic rate dependency of contraction.

3) Using our novel coupled model we have analyzed the role of possible parameters contributing in the formation of arrhythmogenic substrate for post-operative atrial fibrillation condition. The model was analyzed to dissect the role of each component from Ca-handling and contractility in the vulnerability to alternans incidence and threshold shifting.

4) The role of mechano-electric and mechano-calcium feedback effect was analyzed on the AP and Ca-handling characteristics under iso-sarcometric and isometric conditions. Using the coupled model the role of stretch in contrubting for arrhythmogenic substrate formulation favouring atrial fibrillation was quantified.

The developed electromechanically coupled computational model has the potential for investigating the key mechanisms underlying the physiological and pathological conditions.

Thesis Outline

The aim of the thesis is to shed light on the importance of coupling electrophysiology and contraction and to study it as an integrated system. In this regard, thesis begins by highlighting the indifferent behavior of the existing models when compared with the human atrial experimental data highlighting the need of a novel electro-mechanically coupled model. Later, the thesis presents a novel model development, calibration, and validation based on various tests under physiological conditions. The role of mechanical feedback pathways on the excitation and Ca-handling transport has been quantified. At the end, the thesis highlights the therapeutic potential of the model by showing the predictive power of reducing the atrial fibrillation induced burden under post-operative conditions. Thesis outline is as follows,

Chapter 1 reviews the theoretical, experimental and modeling aspects necessary to understand the *cross-talk* between electrical and mechanical process on a cellular scale under physiological and pathological conditions. While looking into the importance of studying human atrial modelling, the chapter also highlights the key cellular mechanisms that differ between atrial and ventricular myocytes. At the end a state-of-the-art review for existing human electromechanically coupled model has been compiled presenting the major development produced by each model.

Chapter 2 discusses the electromechanical integration and Ca^{2+} homeostasis involved in human atrial coupling using the existing computational models both from electrophysiology and contraction. In this chapter, using the coupled model, we have identified the indifferent behaviour of the model for rate adaptation when compared to the experimental data.

Chapter 3 presents the development of a novel electromechanically coupled human atrial cardiomyocytes model and calibration techniques based on biomarkers from human atrial experiments. The chapter highlights the characterictic features of the model that includes CaMKII based phosphorylation effect, mechano-calcium and mechano-electric feedback pathways that produced a physiological Ca-transient followed by a physiological twitch having biomarkers in agreement with human atrial data.

Chapter 4 comprises of the validation tests for the developed coupled model presented in Chapter 3. In this chapter we aim to simulate the possible mechanisms found in literature that favour in the development of an arrhythmogenic substrate and can lead to post-operative atrial fibrillation, a post cardiac surgery complication. In this chapter we have presented a detailed analysis of the factors from Ca-handling, contraction, coupling and CaMKII effect that can contribute to the development of a arrhythmogenic behaviour at higher rates.

Chapter 5 demonstrates the modeling of mechano-electric feedback in the our coupled model using stretch activated channels. The chapter presents the calibration of the stretch activated current followed by its role on the coupled model characteristics at basal frequency. The role of stretch induced arrhythmias at higher rates was also analysed with some insights on the cellular mechanisms.

Chapter 6 presents a optimization run of the developed model that improves the dynamics of SR uptake. Using the optimized model, the therapeutic potential was evaluated by analyzing the anti-arrhythmic effect of atrial-specific I_{Kur} current block. We have presented a comparison of I_{Kur}-

specific and less specific blockers effect on the model characteristics, and its effect on rate adaptation of APD. The atrial specific I_{Kur} blockers was found as a suitable treatment for atrial contractile dysfunction arising due to atrial tachyarrhythmias.

Chapter 1

Electromechanical Coupling in Physiological and Pathological conditions: a fresh perspective from *in-vitro* and *in-silico* studies

1.1 Introduction

The heart depolarizes electrically to trigger the mechanical contractions by a forward pathway namely electro-mechanical (EM) coupling. Being a mechanical pump, the heart has intrinsic ability to adjust its performance to the constantly changing mechanical environment by modifying electrical, mechanical, and structural properties ranging over a time scale. The heart's propensity of being mechanosensitive is because of the feedback pathway known as mechano-electric feedback (MEF). This bidirectional regulatory phenomenon is manifested at both cellular and whole heart scales. On the whole heart scale, the normal mechanical activation follows the timing of electrical activation resulting in a fairly synchronized contraction pattern. Similarly, the acute changes in mechanical environment like the cardiac contraction, venous return to the heart (the preload), the work done against which the heart pumps the blood out (afterload), and the external factors that contribute to these variations can modulate the heart rate and rhythm. On the cellular scale, the changing length of cardiac muscle increases the contraction, which is the basis of the macrolevel Frank-Starling law of the heart.

On the cellular level, the crosstalk between electrical and mechanical process can be conceptualized using Figure 1.1. The forward connection, excitation-contraction, mediates the alterations of excitation and Ca-handling on the contraction whereas, the feedback, mechano-electric or mechano-calcium regulates the mechanical variation effect on the electrophysiology and Ca-handling. In this chapter, I will review the cellular aspects of EM and MEF phenomena under physiological and pathological conditions by highlighting the cellular mechanisms and the work done in *in-vitro* studies. Given the theoretical and clinical importance of this bidirectional regulatory mechanism, I will present a state-of-the-art review of the role of computational modelling in EM coupling highlighting the current perspective of *in-silico* studies.

1.2 Electrical modulation of Contraction

The application of action potential (AP) produces a transient rise in Ca^{2+} concentration $[Ca^{2+}]_i$ via calcium induced calcium release phenomenon thanks to the sarcoplasmic reticulum (SR) that acts as a control signal to activate contraction at the basic level of contractile unit i.e. a sarcomere. A sarcomere is composed of thin and thick filaments that regulate the cooperative activation of cross bridge (XB) cycling that activates the contractile force (F_{active}).

The thick filament of the sarcomere is named myosin that has a α-helical tail and a globular head structure. The tail is formed by two myosin heavy chains (MHCs) coiled around each other and forms the main axis of the thick filament. The head has binding sites for the thin filament, the actin and the site for ATP hydrolysis and has two myosin light chains (MLCs) associated with each head. One of the MLC is the regulatory light chain, MLC2 that is phosphorylatable and alters its function in response to Ca binding. The Ca^{2+} dependent activation of acto-myosin interaction is demonstrated in Figure 1.2 (adapted from Bers 2001) under diastolic and systolic conditions. The actin filament is composed of a long protein structure named tropomyosin (Tm) that spans about 7 actin monomers and a troponin (TRPN) complex residing at every seventh actin monomer. TRPN is made up of three units: TnC (Ca^{2+} binding site unit), TnT (Tm binding unit), and TnI (Tm inhibitory unit). With the rise of Ca^{2+} levels in the cytosol, Ca^{2+} binds to TnC and that is sensed by TnI and TnT resulting in allosteric shift of the Tm to allow myosin head to interact with

actin. In the literature, many myofilament protein isoforms are reported that vary among species and in cell type and are also considered a measure of cardiac energetics and performance i.e. ATPase rate or muscle fiber shortening rate. In human ventricular tissue, the slow (β) MHC predominates whereas, atrial tissue has a mixture of fast (α) and slow (β) isoforms resulting in 5-fold economical but nine times slower contraction in human ventricular muscle (Narolska et al. 2004). This difference in myofilament protein isoforms impacts the maximum unloaded shortening velocity (V_{max}) that was found to be lower in ventricles fiber than V_{max} of atrial fibers for both human and pig (Morano *et al.* 1988).

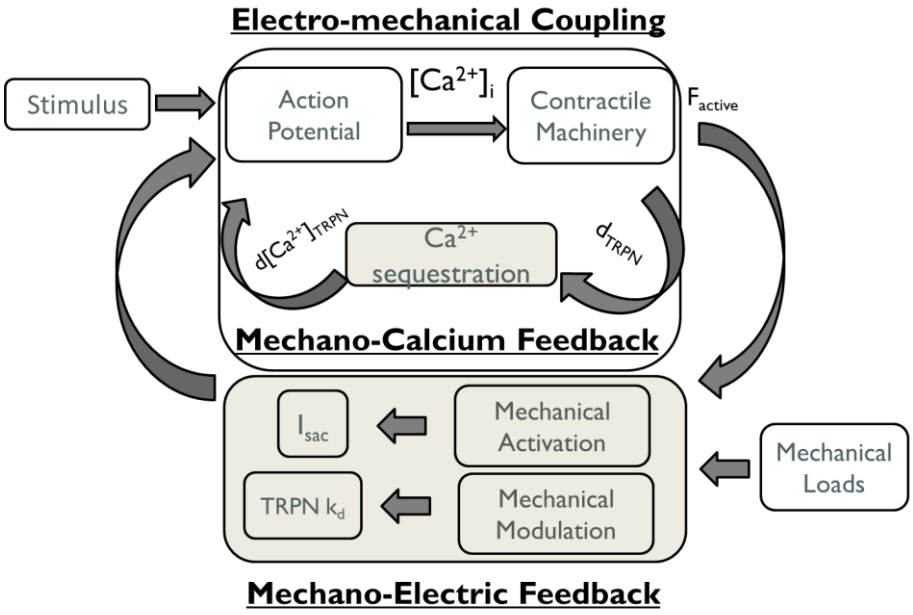

Figure 1.1: Mechano-electric regulatory loop along with feedforward (Electro-mechanical coupling) and feedback (Mechano-calcium and Mechano-electric) pathways.

The Ca^{2+} based activation of acto-myosin binding can give arise to additional XB bindings independent of Ca^{2+}, that is termed as cooperativity, because the bound myosin head can push the Tm into actin groove deeper than that of the open state condition of filament produced by Ca-TnC (Campbell *et al.* 2010). The well-known steady state non-linear steep force-pCa relationship demonstrates a slope factor of more than one or even 5 to 9 indicating a high level of cooperativity involved in the Ca-dependent activation of force (Dobesh *et al.* 2002). The length dependence increase in force/XB formation can increase the affinity of myofilament but does not impact the cooperativity level. The myofilament Ca^{2+} sensitivity modulation can also be related to the resting tension produced by giant protein titin other than sarcomere length and inter lattice spacing (Lee *et al.* 2013) as was observed (Cazorla *et al.* 1997, Methawasin *et al.* 2014).

The Ca^{2+} sensitivity of myofilament is highly variable among species, muscle preparations and cell types. The reduced Ca^{2+} sensitivity of rat skinned ventricular muscle when compared to intact preparation was associated with altered MLC2 phosphorylation resulting in modified XB kinetics (Gao *et al.* 1994). Isometric tension and its Ca^{2+} sensitivity was smaller in skinned preparations of atrial than in ventricles (Velden *et al.* 1999). The acto-myosin XB kinetics also varies based on

the cell type preparations and the failing/non-failing hearts. Dynamic stiffness frequency as measure of XB interaction and kinetics was higher in atrial than in ventricular human myocardium and lower in failing than in non-failing left ventricular human myocardium (Ruf *et al.* 1998).

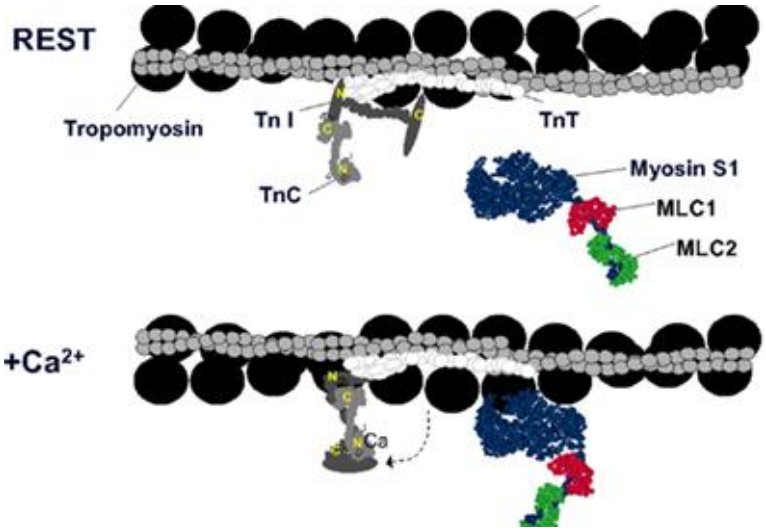

Figure 1.2: Ca^{2+} dependent regulation of actin and myosin interaction in a sarcomere. Adapted from (Bers 2001).

1.3 Mechanical modulation of Electrophysiology and Ca-handling

On the cellular scale, the varying mechanical conditions regulate the electrical activity (Peyronnet *et al.* 2016, Quinn & Kohl 2020) and the Ca^{2+} handling (Calaghan & White 1999, Neves *et al.* 2015) under both physiological and pathological conditions (Varela *et al.* 2020, Pfeiffer *et al.* 2014, Ravens 2003, Taggart & Sutton 1999). Physiologically, the variations in mechanical conditions are a subject of intrinsic ability of the contraction itself or extrinsically varying circulatory parameters (also shown in Figure 1.1 as a mechanical load). The intrinsic mechanisms can be either because of the modulation of length and/or tension developed in the cell/tissue, the *inotropic response*, or modulation in the timing of subsequent beats, the *chronotropic response*. In this chapter, the focus will be on the inotropic response of contraction on electrophysiology under both physiological and pathological conditions.

1.3.1 Mechanical modulation of Electrophysiology

The mechanical modulation of cardiac electrophysiology can be divided into systolic, i.e. amplitude, plateau and repolarization duration of the AP and diastolic effects i.e. changes near the resting membrane potential (RMP) of the AP. Moreover, the mechanical changes can be instantaneous followed by additional slow response.

The mechano-sensors that majorly affect the AP are the ion channels that can be either activated by a mechanical stimulus referred as mechano-activated channels (MACs) that can be volume or stretch activated currents (I_{sac}); or can be modulated by a mechanical stretch i.e. requires a coactivation by a non-mechanical stimuli too, and are referred as mechanically modulated channels (MMC). MMC can affect the voltage gated ion channels including K^+ (Kv1.5, Kir channels), Na^+ (Nav1.5), the ligand activated channels (K^+ ATP inactivated channels). A detailed review of MMC related modulation of cardiac cells can be found in (Peyronet *et al.* 2016, Ravens

2003). On the cellular scale, MACs are the stretch activated gates (SAC) whose open probability is modulated as a response to stretch. Very often, the SAC are subdivided in K^+ selective (SAC_K) and non-selective (SAC_{NS}) cations channels. SAC_{NS} allows Na^+, Ca^{2+} and K^+ to enter the cells and the reversal potential, based on the relative permeability of ion channels, is halfway between the RMP and the plateau potential i.e. 0 and -50mV and has a near-linear voltage dependence (Kim 1993). Hence, the activation of SAC_{NS} can depolarize the cells, while during the plateau phase can cause repolarization of the AP. In contrast, the reversal potential of SAC_K is close to RMP hence, can modulate the repolarization phase more than the RMP of the AP.

In experimental studies, the electrophysiological response of stretch is complex and is dependent on magnitude, duration, and timing of the stretch with respect to the AP dynamics. During the AP diastole, moderate level of stretch can produce a lengthening of APD (Tavi *et al.* 1998) and for high stretch magnitude delayed afterdepolarizations (DADs) effect was found in rat atria (Tavi *et al.* 1996) along with an increase in relative conduction velocity. Stretch applied in guinea pig atria early in the diastole resulted in early afterdepolarization (EADs) and shortening of APD during mid repolarization phase (Nazir & Lab 1996). Similarly, stretch applied in ventricles during the onset of contraction shortens the APD whereas stretch applied during the peak activity produced minimal effect as was observed in frog (Lab 1980) and rabbit hearts (Zabel *et al.* 1996). The stretch induced shortening of APD in dilated rabbit ventricles was also observed during the rate adaptation of the effective refractory period (ERP) and the late repolarization phase (Eckardt *et al.* 2000). Acute atrial stretch induced enhanced vulnerability of arrhythmias like atrial fibrillation (AF) was observed in rabbit atria (Bode *et al.* 2003).

In human hearts, the varying cycle length of atrial flutter was associated with raised atrial pressure during ventricular contraction (Ravelli *et al.* 1996) that confirms the existence of MEF in humans too. Hypertrophied ventricular cardiomyocytes demonstrated higher stretch-sensitivity providing an increased risk of stretch induced arrhythmias (Kamkin *et al.* 2000). A similar finding was observed in atrial myocytes where SAC_{NS} preferentially with Na^+ influx was observed as a stretch induced arrhythmogenic phenomena (Kamkin *et al.* 2003). In another study, acute atrial dilation was found to be associated with conduction slowing and hence vulnerable to AF (Ravelli *et al.* 2011). Recently, increased activity and expression levels of SAC_{NS} were associated with atrial fibroblast in patients with sustained AF and the SAC_{NS} were identified as Piezo1 channels (Jakob *et al.* 2021).

1.3.2 Mechanical modulation of Ca-handling

Mechanical stretch increases the inward flow of Na^+ ions in the myocytes either through SAC_{NS}, or (and) by the activation of Na^+/H^+ exchanger, or (and) by MMC gate (Nav1.5) (Del-Canto *et al.* 2020) or (and) the reverse mode of Na^+/Ca^{2+} exchanger (I_{NaCa}). Additionally, Ca-handling is mechanosensitive and involves modulation of Ca^{2+} buffering with TRPN and of the release and uptake fluxes. The effect of stretch induced reduction of diastolic $[Ca^{2+}]_{SR}$ has been reported in rat trabeculae (Gamble *et al.* 1992) and in mouse atria (Tsai *et al.* 2011) and is often associated with the increased rate of diastolic Ca^{2+} sparks as was reported in guinea pig intact ventricular myocytes (Iribe & Kohl 2008).

Mechanical stretch can elicit a biphasic increase in contraction, an immediate increase inline with the Frank-Starling law of heart, followed by a slower increase. The stretch induced rapid response of contraction was associated with enhanced sensitivity of Ca^{2+}-TRPN buffering whereas the slower rise in contraction was because of a consecutive increase in Ca^{2+} transient in rat atria (Tavi *et al.* 1998), and in rat ventricular trabeculae (Kentish & Wrzosek 1998). The mechanism behind the slow force response in humans differs substantially among the atrium and ventricles. In ventricles slow rise in contraction was associated with SAC mediated rise of Na^+ via Na^+/H^+ and I_{NaCa} exchangers however, in atria, the slow response was caused by an angiotensin II and endothelin dependent mechanism (Kockskämper *et al.* 2008). On the other hand, the rapid response of contractility induced by enhanced sensitivity of Ca^{2+}-TRPN binding can be explained by the length-dependent increase of contraction (Lookin & Protsenko 2019) as was already discussed above.

1.4 Anatomy, Cellular Structure of the Atria

During the cardiac-cycle, atrial contraction and relaxation, corresponding to the P-wave in electrocardiogram, occurs during the diastolic stage and are responsible for filling 20-30% of the blood in ventricles prior to systole (Namana *et al.* 2018). This contribution of atrial contraction increases substantially during increased activity and hence, can make a significant difference to the heart performance and is referred as 'atrial-kick'. During cardiac dysrhythmia like AF, the dis-coordinated atrial contraction does not propel the required blood into the ventricles hence, the absence of atrial-kick can reduce the blood pumping capacity of the heart.

Given the importance of atrial contraction, this section proceeds with highlighting a few anatomical features of the atrium and then moving onwards to the cell structural aspects of atria underlying differences with respect to the ventricles.

1.4.1 Anatomy of the atria

The thin-walled atrium can be divided into three components: the venous part, the appendage, and the vestibule (Figure 1.3A). The remaining part is the septum, a thick muscular structure that divides the atria and is crucial for interventional procedures. The appendage, also known as auricle, is a wrinkled flap when not filled with blood but becomes expandable in the presence of blood. The appendage vestibule is a smooth area between the orifice of the appendage and the atrioventricular valve annulus (Holda *et al.* 2020). The venous components are the posterior part of the left atrium receiving the pulmonary veins (PVs). The PVs return blood from the lungs to the LA via four trunks. In the right atrium, the blood returning from upper limbs, head, neck, and chest is carried through superior caval vein (SCV) and is located in the posterior of the superior RA whereas, inferior caval vein (ICV) located in the posterior of the inferior RA carries the blood from lower limbs. The aorta is a cane-shaped curve that is the main artery that carries blood away from the heart to the body. The anterior wall just behind the aorta is exceptionally thin and it gets even thinner in the area near the vestibule (Figure 1.3B). The inferior of posterior wall contains the esophagus and vagal nerves and coronary sinus (CS). CS is a large thin-walled vein, opens into the inferior of SCV in the posterior of septum (shown by asterisk in Figure 1.3C) and it returns blood from the coronary circulatory system to the RA.

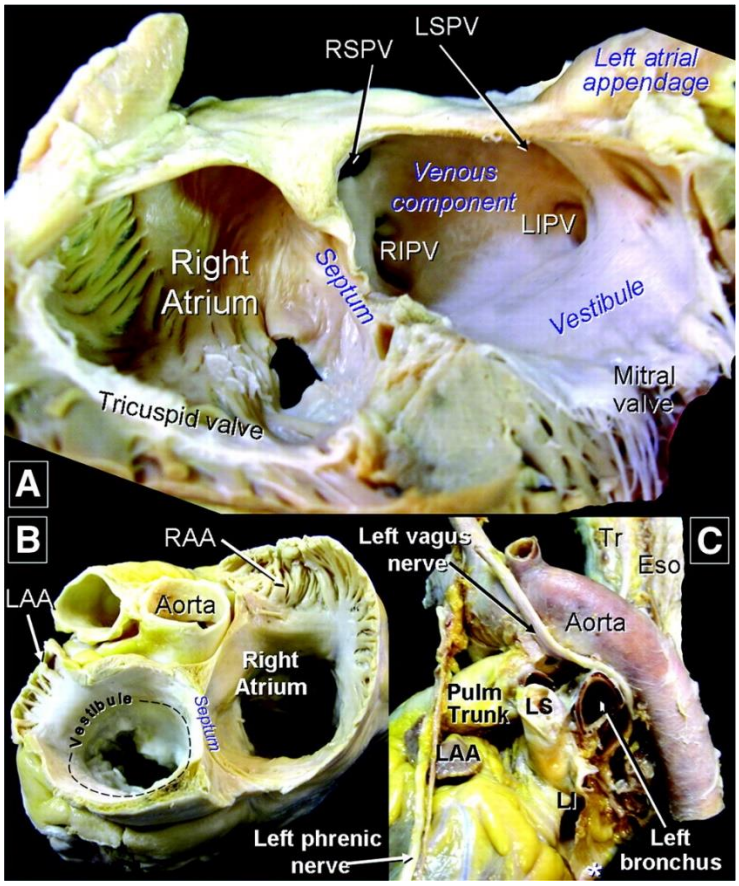

Figure 1.3: A) Smooth endocardial walled surface of left atria viewed from left anterior. B) Dissected view from the back. C) Posterior view of the left atrium. Asterisk marks the location of coronary sinus (CS). Eso: esophagus; LAA: left atrial appendage; LI, left inferior; LS, left superior; PV, pulmonary vein; RI, right inferior; RS, right superior; RAA, right atrial appendage; and Tr, trachea. Adapted from (Ho *et al.* 2012).

Multiple muscular bridges of varying widths, thicknesses, and musculature of the septum are present between the atrial chambers. The interatrial conduction of sinus impulse, originating from the sino-atrial node (SAN) to the anterior left atrial wall is through Bachman bundles (BB) and is located on the superior of crista terminalis (CT) and extended till near the SCV deep into LA. The impaired conduction pathways through CT, BB, and pectinate muscles (PM) play a critical role in the pathophysiology of the atrial tachycardias as was studied by Becker (Becker 2004) where the patients with AF demonstrated more pronounced fibro-fatty replacement of myocardium in CT and BB. On the septum, near the CS and superior to the ICV is the atrio-ventricular (AV) node which is a bridge between atrial and ventricular conduction.

1.4.2 Left atrial physiology and pathophysiology

LA is a dynamic modulator of left ventricle (LV) filling. Being an active chamber, it transports blood from PVs to the LV. In particular its cardiovascular performance is divided in three basic functions, 1) a reservoir of oxygenated blood from PVs during ventricular systole, thus any LV dysfunction can impact the reservoir function; 2) a conduit for PVs for early diastole of ventricles, usually this phase contributes less in ventricular stroke volume but acts dominantly in late diastolic dysfunction, in case of impaired reservoir function during atrial contraction and 3) a

contractile booster pump that reflects atrial contractile function during late ventricular diastole that modulates ventricular filling (Carpenito et al. 2021). These LA finctions are assessed by using volumetric analysis; spectral doppler of PV flow, transmitral flow, and LA appendage flow; tissue doppler, and deformation analysis (Hoit 2014).

In cardiovascular medicine, LA size and function assessment plays a potential role in determinant of symptoms, prognosis and potential treatment in heart failure (HF) patients (reviewd in Carpenito et al. 2021). LA volume indexed to body surface area (LAVi) is a most accurate measure and is strongly associated with cardiovascular disease prediction like development of first AF, congestive HF, stroke (cerebrovascular accident [CVA]), transient ischemic attack, acute myocardial infarction (AMI), and car- diovascular death over 3.5 years of follow-up (Tsang et al. 2006).

1.4.3 Cellular differences between atrial and ventricular cardiomyocytes

On cellular scale, atrial cardiomyocytes share many common structural and functional similarities with ventricular myocytes with some critical differences. One of the key differences lies in the structural arrangement in the atrial myocytes of T-tubules, which are either missing or have a very irregular arrangement (Frisk *et al.* 2014) and therefore express voltage operated Ca^{2+} channels (VOCs) only on the membrane (Brette & Clive 2003). It has been suggested that in place of T-tubules the atrial cells have a prominent structure of SR named Z-tubules (Bootman *et al.* 2011). In atrial myocytes, the distribution of Ca^{2+} release units, ryanodine receptors (RyRs), is like the ventricular cells with some discontinuity that divides it into junctional RyRs, that being in small number and sits just beneath the sarcolemma, and non-junctional RyRs that are deeper inside the cell and constitutes the bulk of the RyR population (Bootman *et al.* 2011). This difference of structure i.e. T-tubules, RyR distribution and VOCs location significantly impact the spatial signaling of the Ca^{2+}-transient within the cytosol. Consequently, Ca^{2+} release in atrial myocytes is spatially heterogeneous throughout the cell, rising from the periphery and propagating to the center hence lacking the 'local control' phenomena of Ca-SR release. In one of the studies, where the VOCs gated Ca^{2+} release induced a regenerative Ca^{2+} release from the adjacent SR compartments that propagates towards the center giving arise to contraction in rat atria (Tanaami *et al.* 2005), rabbit atria (Greiser *et al.* 2014), and in cat atria (Shkryl & Blatter 2013). In human atrial myocytes, a biphasic rise of Ca^{2+} with prolonged and dome-shaped transient was observed reflecting the RyRs activation not fully coupled with VOCs (Hatem *et al.* 1997). Based on these experimental findings, Blatter proposed a novel paradigm of atrial excitation-contraction that was termed as 'fire-diffuse-uptake-fire' (FDUF) mechanism (Blatter 2017). The FDUF mechanism summarizes the series of events in atrial myocytes that initiates by the VOCs gated Ca^{2+} triggering the CICR from junctional RyRs and subsequently activates the CICR from the centrally located RyRs therefore, resulting into CICR propagation. The propagation of CICR is sustained by FDUF mechanism that elevates the Ca^{2+}-transient in the whole cell and hence initiates contraction.

1.5 Human Electromechanical Computational Modeling- a short review

Human biological systems are very complex and it becomes difficult to identify the causal relationship or predict the responses. In an integrated electromechanically coupled system it becomes hard to understand the individual contributor of cardiac electrics and mechanics under both physiological and pathological conditions. Computational modeling provides us with a comprehensive and powerful means of understanding the interrelated processes in a highly integrated system. Most of the computational cardiac models developed so far are based on separate tracks of electrophysiology and contractility however, after looking into the interrelated modulatory effects of electro-mechanics and mechano-electrics (as described in sections 1.2 & 1.3) it seems crucial to study the bidirectional coupling as an integrated system. The individual components of EM models for both atrial and ventricular cardiomyocytes have been reviewed in literature: the electrophysiology for atrial (Heijman *et al.* 2021) and ventricular models (Sutanto & Heijman 2022), Ca-handling (Sutanto *et al.* 2020), MEF coupling in atrial (Varela *et al.* 2021) and ventricular models (Lee *et al.* 2022).

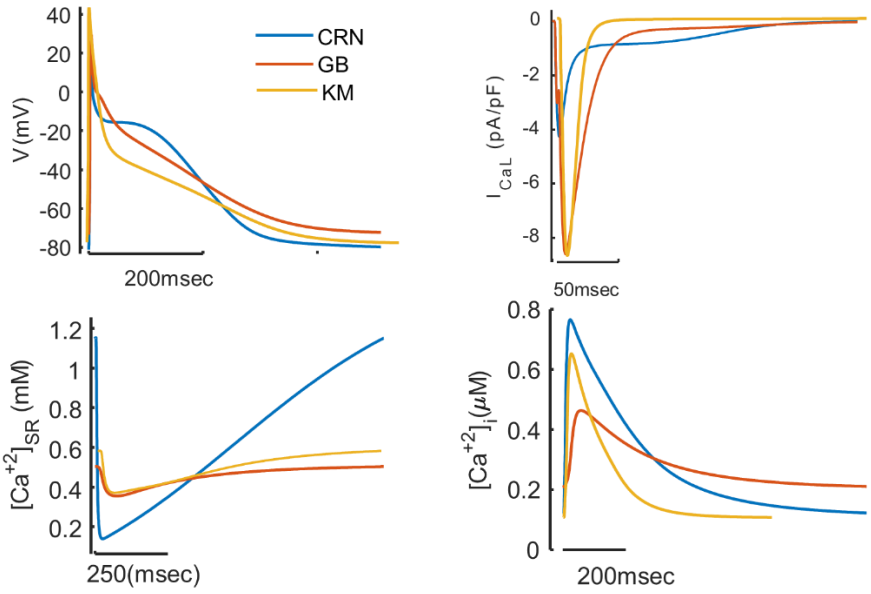

Figure 1.4: Comparison of human atrial action potential models represented by, Courtemanche 1998 (CRN) in blue, Grandi 2011 (GB) in red, and Koivumaki 2011 (KM) in yellow. Top left panel represents the action potential, top right represents the Ca^{2+} entering through VOCs i.e. I_{CaL} current, bottom left panel shows the Ca^{2+} content in the SR (for KM the major storage of $[Ca^{2+}]_{SR}$ i.e., near the subspace is shown), bottom right panel shows the CICR triggered Ca^{2+}-transient produced in the cytosol.

Human atrial electrophysiology models exhibit AP shapes that are markedly heterogeneous. As reported in experiments, three AP shape types were differentiated: type 1 (spike and dome), type 3 (no dome), and type 4 (extremely prolonged) (Dawodu *et al.* 1996). In human atrial computational models, three widely used AP models, the Courtemanche 1998 (CRN) in blue, Grandi 2011 (GB) in red, and the multi-compartmental model of Koivumaki 2011 (KM) in yellow, are compared in Figure 1.4 with respect to their AP morphologies and Ca-handling characteristics. The CRN model demonstrates type-1 AP with a more prominent positive phase 2 and slightly short

phase 3. On the other hand, GB has a type-3 AP with more positive phase 1 potential, more prolonged phase 3, and a depolarized RMP (phase 4). In contrast, KM has a triangular morphology with negative plateau, and a wide phase 3 hence, demonstrating a type-4 like morphology. The trigger of EM coupling is the Ca^{2+} entering the cell by VOCs i.e. the I_{CaL} current density and is compared in top right panel for all the three models. KM and GB demonstrate large I_{CaL} peak current with fast inactivation whereas, CRN has smallest peak current with slow inactivation. The inactivation mechanism in CRN model is divided into fast and slow phases where the fast inactivation is calcium dependent and slow inactivation is voltage based whereas in KM model calcium dependence does not serve as a prominent inactivation mechanism. The Ca^{2+} storage in SR is compared for the three models in bottom left panel where CRN dominates the other two models with a very large Ca^{2+} SR contents and a large release with a slow refilling of the SR. The SR content of Ca^{2+} is the measure of release and uptake fluxes as can be seen GB model with least SR Ca^{2+} content has the smallest release with slow uptake. For KM model, out of the four compartments of Ca^{2+} SR, I have shown the major storage of SR that is near the membrane and is more relevant to CICR initiation. The triggered CICR is compared in the form of intracellular Ca^{2+}-transient where CRN shows a larger amplitude than GB and KM. The ratio of Ca^{2+}-transient amplitude to the I_{CaL} needed to induce it is an index of EM coupling gain. Thus, a Ca^{2+} channel opening at more negative AP will yield a larger I_{CaL} (as in the case of KM and GB) and therefore will more likely trigger the Ca^{2+} SR release hence, producing a higher coupling gain (see Figure 117, Bers 2001). In addition, the coupling gain is also expected to vary as a function of SR Ca^{2+} load, at higher loads (as in CRN) both gain and release increase steeply and that is related to the sensitization of RyRs due to high $[Ca^{2+}]_{SR}$ (Györke & Györke 1998). The decay kinetics of the Ca^{2+}-transient have correspondence with refilling time of the SR and the cytosolic buffering kinetics. Hence, the mean Ca^{2+}-transient decay for KM demonstrates a fast decay since it lacks TRPN buffer and has a faster SERCA pumping rate.

Human based electromechanically coupled cardiomyocytes model for various cell types developed in recent years are shown in Table 1.1. The EM models were developed for a wide range of applications varying from the effect of AP regional heterogeneity on contractility (Sachse *et al.* 2003), MEF effect on conduction velocity (Kuijpers *et al.* 2008), the impact of fibroblast related SACs on electrophysiology (Zhan & Xia 2013; Zhan *et al.* 2017), the role of contraction parameters in APD and Ca^{2+} alternans development (Zile & Trayanova 2016; 2018), and the effect of β-adrenergic stimulation effect on contractility (Pueyo *et al.* 2016, Lyon *et al.* 2020). However, the EM model validation based on experimental data always remains challenging either because of the sparsity or heterogeneity of the data. Also, the contraction model used for the coupling of EM models is based on an analytical description of Ca^{2+}-transient hence, requiring a considerable level of re-tuning the contraction parameters to couple it with atrial or ventricular human AP models. The very first attempt was made by Land (Land & Niederer 2018) to study the influence of human atrial mechanics during AF on the whole heart model. However, not every contraction parameter was re-tuned according to human atrial physiological contraction data. A couple of other studies have recalibrated the contraction parameters either as a result of a hybrid optimization process for ventricular myocytes (Bartolucci *et al.* 2022) or by manual tunning (Zile & Trayanova 2018; Forouzandehmehr *et al.* 2021). Apart from this, it can be noted from Table 1.1 that all the atrial EM models were not calibrated or validated for the cell level mechanism. Also, the EM

models used the gold standard AP model in human atrial modeling i.e., the CRN that lacks the detailed Ca-handling FDUF mechanism. Therefore, the EM models should have a tight integration with the experimental data that can ensure a better insight into the electromechanical coupling.

Table 1.1: Recently developed human electromechanical cell level models ranging from various cell types along with the description of action potential (AP) and contraction models and the major development made by each model. Abbreviations: PB: Priebe-Beuckelmann, LRd: Luo-Rudy, CRN: Courtemanche, ORd: O'Hara Rudy, TTP: ten Tusscher Panfilov, GB: Grandi, CG: Chang 2014, ToR-ORd: Tomek-ORd.

Model	Cell type	AP model	Contraction model	Development
Sachse et al. 2003	Ventricular	PB, LRd	Sachse et al.	1. Effect of regional electrophysiology heterogeneities on contraction. 2. No validation of coupled model.
Kuijpers et al. 2008	Atrial	CRN	Rice 1999	1. Effect of MEF on conduction velocity in a dilated atria. 2. No validation of cell level coupled model.
Zhan & Xia 2013	Atrial	CRN	Rice 2008	1. Impact of fibroblast related SAC on electrophysiology. 2. No description/validation of Ca-handling.
Brocklehurst et al. 2015	Atrial	CRN	Rice 2008	A 2D tissue level coupled model, but cell level model not calibrated/validated.
Pueyo et al. 2016	Ventricular	ORd, TTP	Niederer	1. Phasic β-adrenergic stimulation effect on phasic changes in APD. 2. No validation of the model.
Zile & Trayanova 2016	Ventricular	TTP	Rice 2008	Simulation of heart-failure induced electrical and mechanical alternans.
Timmerman et al. 2017	Ventricular	ORd, GB	Rice 2008, Land 2017	1. Effect of strain and fibrosis on cellular electrophysiology (through SAC). 2. Qualitative validation of the model.
Zhan et al. 2017	Atrial	CRN	Rice 2008	1. Role of MACs in fibroblast in effecting contraction. 2. No cell level description of validated Ca-handling.
Land & Niederer 2018	Atrial	-	Land 2017	1. Calibration of contraction parameters 2. Not every contraction parameter was re-tuned.

Zile & Trayanova 2018	Atrial	CG	Zile 2016	Role of myofilaments in alternans development in cAF condition.
Lyon et al. 2020	Ventricular	ORd	MedChem (Dupuis 2018)	Difference of β-adrenergic effect and stretch on a coupled model.
Vikulova et al. 2020	Ventricular	TTP	Ekaterinburg-Oxford	Simulation of afterload and isometric twitches and their impact on APD, Ca^{2+}-transient and contractility.
Forouzandehmehr et al. 2021	Stem cells	Paci 2020	Rice 2008	Calibrated contraction parameters and simulates aftercontractions.
Margara et al. 2021	Ventricular	ORd, ToR-ORd	Land 2017	Simulation of drug-induced pro-arrhythmic and inotropic risk assessment.
Bartolucci et al. 2022	Ventricular	BPS2020	Land 2017	Calibrated model with simulation of cardiac abnormalities and rate adaptation.

Conclusion

Electromechanical coupling and its feedback regulatory loops can have physiological and pathological impact on the heart performance. The interconnected modulatory effects of electro-mechanics and mechano-electrics emphasize the importance of studying the bidirectional coupling as an integrated system. Computational models can help to enhance physiological information given a complex electromechanical integration system. The key challenges in the development of the *in-silico* models are their calibration against a detailed set of experimental studies followed by a series of validation tests. This well-validated model can serve as a useful tool to confirm the cause-effect relationships as suggested by the experiments.

Chapter 2

Positive Force-Frequency relationship is maintained by the Detailed Ca^{2+} Handling Representation in Human Atrial Cardiomyocytes

The content of this chapter has been published in:

"Human Atrial Cell Models to Analyse the Effect of Extracellular Calcium on Action Potential Duration."

Fazeelat Mazhar*, Chiara Bartolucci, and Stefano Severi.*

Computing in Cardiology, IEEE, 2020.

"Electro-Mechanical Coupling in Human Atrial Cardiomyocytes: Model Development and Analysis of Inotropic Interventions."

Fazeelat Mazhar*, Francesco Regazzoni, Chiara Bartolucci, Cristiana Corsi, Luca Dedè, Alfio Quarteroni, and Stefano Severi*

Computing in Cardiology, IEEE, 2021.

Abstract

Human-based computational models are a powerful tool that complements experimental approaches and can improve our understanding of individual components of the heart by integrating them into one system. This chapter presents a coupled and calibrated human atrial electro-mechanical model that will be used to analyze the coupling effects and inotropic interventions on human atrial electrophysiology, calcium dynamics, and active isometric contraction on a cellular scale. An existing human atrial electrophysiology model was coupled with one of the recently developed biophysically detailed contraction models. A collection of human atrial experimental data has been presented to calibrate the coupled model. The calibrated electro-mechanical human atrial model yielded action potential, calcium transient and active tension that were validated against the experiments and conclusions were drawn to explain the mismatch between *in-silico* and *in-vitro* experiments on inotropic interventions. A brief analysis of extracellular Ca^{2+} concentration variations is also presented based on existing electrophysiology models. The coupled and calibrated human atrial electro-mechanical model and simulation framework developed in this study serves as a pathway for future investigations of the effect of contractile performance and inotropic interventions on the electrophysiology of the atria.

2.1 Introduction

Atrial Fibrillation (AF) is the most common cardiac arrhythmia characterized by adverse changes in electrophysiology and intracellular Ca^{2+} signaling of atrial myocytes (Kirchhof *et al.* 2016). Contractile remodeling is the major consequence of impaired electrical activation and Ca^{2+} handling that includes alterations in active and passive force levels, and cross-bridge (XB) binding rates (El-Armouche *et al.* 2006, Eiras *et al.* 2006). Based on the inter-dependence of excitation and contraction it is crucial to study them as a coupled system. Computational modelling and simulation is a powerful tool to accelerate the mechanistic understanding of a complex inter-connected coupled system. Several atrial cellular models have been proposed that provide substantial insights into the pathophysiology of the atrial cell usually through separate tracks of EP and contractility (Heijman *et al.* 2021). Hence, an integrated electro-mechanical (EM) model of human atrial cardiomyocyte with a calibrated set of contraction parameters is lacking. This study aims to investigate the coupling effects in human atrial action potential (AP), calcium dynamics and active isometric contraction, and the inotropic effects by varying the rate and its dependence on force. For this purpose, human atrial AP and contraction model are coupled and calibrated using experimental data. For the choice of AP model, a detailed ionic model, Courtemanche (CRN) (Courtemanche *et al.* 1998) was considered and for the contraction part a recent model by Regazzoni-Dede-Quarteroni based on mean field approximation, RDQ-MF (Regazzoni *et al.* 2020) was employed. RDQ-MF is computationally efficient and biophysically detailed model for cardiac force generation. The proposed model highlights the limitation of rate adaptation on inotropic properties of the heterogeneous excitation and mechanical coupling and can be adapted as a pathway in making the right choice of the models for ensuring a strong coupling. Overall, this simulation framework serves as a roadmap for human-based integrated simulation of EP, calcium dynamics and contractility in atrial cardiomyocytes.

2.2 Methods

The AP and contraction models are briefly introduced in the following section. I will also shed some light on the Ca-homeostasis formulations of three known human atrial models by varying the extracellular Ca^{2+} concentration $[Ca^{2+}]_o$. Finally, I will present a stepwise approach for coupling and calibrating the excitation-contraction model.

2.2.1 The AP model: Courtemanche 1998

The human atrial AP model with a spike and dome morphology (type 1) also shown in Figure 1.4 is based on Hodgkin-Huxley type gating formulation. The model is based on membrane currents: fast sodium current (I_{Na}), the transient outward K^+ current I_{to}, the ultra-rapid delayed rectified K^+ current (I_{Kur}), the L-type Ca^{2+} current (I_{CaL}), the rapid and slow delayed rectifier currents (I_{Kr} and I_{Ks} respectively), and the inward rectifier K^+ current (I_{K1}). With a prominent plateau and repolarization, the I_{CaL} and I_{Kur} are stronger, and the I_K current (I_{Kr}, I_{Ks}) have large magnitude. SR Ca^{2+} uptake and release is based on two-compartments, the junctional for release, and the network SR for uptake. The calcium-induced-calcium-release (CICR) mechanism depends upon both Ca^{2+} entering through I_{CaL} channel and membrane potential. The Ca^{2+}-transient is more gradual, longer-lasting and the Ca^{2+} buffering in the cytosol is mediated by troponin (TRPN) and calmodulin (CMDN).

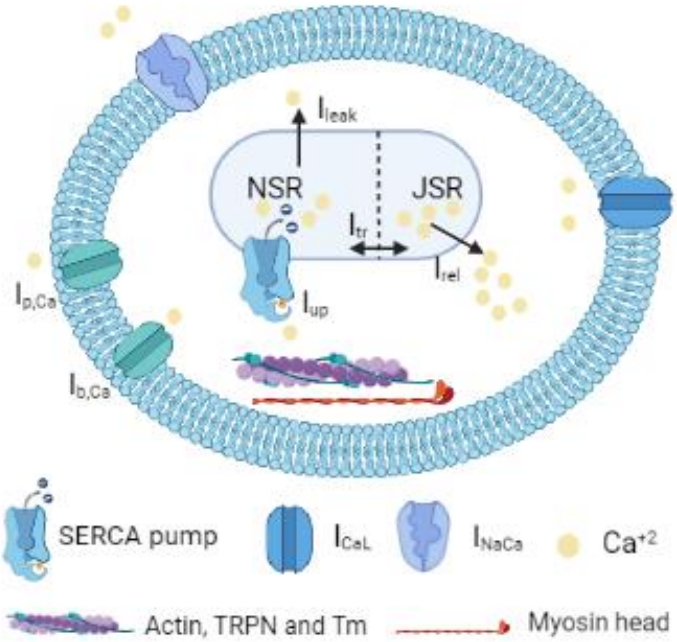

Figure 2.1: Conceptual diagram of electro-mechanical cell level coupling using CRN arrangement of SR compartments.

2.2.1.1. Effect of $[Ca^{2+}]_o$ variations on intracellular Ca^{2+} homeostasis

Intracellular Ca^{2+} homeostasis is a central element for regulating excitation-contraction coupling. The elevation of Ca^{2+} ions entering the cell through I_{CaL} channel is often associated with inotropic response of contraction (Brixius *et al.* 1997). I_{CaL} is the ionic current most affected by the $[Ca^{2+}]_o$ changes and, therefore, affecting the APD. Two mechanisms have been hypothesized:

i) an increased $[Ca^{2+}]_o$ leads to elevated driving force (DF, i.e., the difference between membrane potential V_m and equilibrium potential E_{Ca}) causing an increased I_{CaL} hence a prolonged APD; ii) the calcium-dependent inactivation (CDI) gets strengthened resulting in a reduced APD. For this reason, while analyzing the relationship between APD-$[Ca^{2+}]_o$ both factors (driving force and CDI) should be equally considered.

Based on this, three human atrial AP models: CRN, Koivumäki (KM) (Koivumäki *et al.* 2014), and Ellinwood (EM) (Ellinwood *et al.* 2017) were analyzed for varying $[Ca^{2+}]_o$ for the values 0.9, 1.8 and 2.7mM. The models were analyzed to dissect by using AP-clamp technique and quantify the role of the different mechanisms involved: i) I_{CaL} calcium dependent inactivation (CDI) dependence on $[Ca^{2+}]_o$, ii) the dependence of I_{CaL} driving force on $[Ca^{2+}]_o$.

Using AP-clamp, native AP recorded at steady state and $[Ca^{2+}]_o$ 1.8mM was used as a stimulus for the experiment of CDI dependence on varying $[Ca^{2+}]_o$. The state variables values were recorded for each $[Ca^{2+}]_o$ concentration at steady state. These values were used as initial conditions for the AP-clamp experiments. All the experiments were carried out at a constant rate of basic cycle length (BCL) =1s. For the noCDI simulations, the Ca^{2+} dependent gate was turned off in the I_{CaL} equation and the experiment was repeated for the same set of concentrations.

The third analysis was a modification of the DF in the EM model, by making it independent of Ca concentrations. In particular, the concentrations involved are the sarcolemma (SL) calcium (SL space in most of the models is subdivided into junctional $[Ca^{2+}]_j$ and sub-sarcolemma compartments $[Ca^{2+}]_{sl}$) and $[Ca^{2+}]_o$. By fixing the SL Ca concentrations to their diastolic values ($[Ca^{2+}]_j$ = 0.34μM and $[Ca^{2+}]_{sl}$=0.24μM) and $[Ca^{2+}]_o$ =1.8mM, the trend of I_{CaL} was analyzed in CDI condition using AP-clamp.

2.2.2 The contraction model: RDQ-MF

A biophysically detailed mean-field model that requires the solution of 21 ODEs, thus showing significant computational efficiency. The model is derived from a biophysically detailed continuous-time Markov Chains (CTMC) by neglecting second-order interactions among the proteins, thus resulting in a drastic reduction of size of the model. The regulatory unit (RU) constituting of TRPN and tropomyosin (Tm) are represented by discrete states and cooperativity is included based on the local effect of nearest neighbor interactions among the RUs. The changing sarcomere length effect on force generation is incorporated as a function of single overlap zone. The cross bridge (XB) cycling is characterized by slower time scales hence is confined to attachment and detachment process as was shown by Huxley (Huxley 1957).

2.2.3 Electro-mechanical coupling

The EM coupling of human atrial cardiomyocytes was modelled through the integration of the AP model, CRN and the contractile model, RDQ-MF. The bidirectional coupling was achieved as previously reported by (Timmermann *et al.* 2017). Briefly, a strongly coupled model was developed by incorporating, 1) a dynamic calcium transient generated from AP model serving as an input to the contraction model; 2) the effect of active contractions was feedback into the AP model. The fundamental contractile units of muscle cells are the sarcomeres that generate active tension F_{active} in a myocardial cell. In RDQ-MF model, this process has been split into two parts,

1) the activation of RUs, protein complexes of TRPN and Tm residing on the thin filament, actin as shown in Figure 1. Rise of Ca transient via CICR process, activates these RUs hence resulting in muscle contraction. 2) XB cycling, which is achieved by the interaction of activated RUs, the actin with the thick filament, the myosin that generates F_{active} by consuming the chemical energy stored in ATP (Narolska *et al.* 2005).

In CRN model, the amount of calcium bound to cytosol buffers, CMDN and TRPN is described through a combined scheme and provides a steady-state approximation of the phenomenon. Therefore, to ensure EM coupling, the combined buffering scheme was separated, keeping an algebraic formulation for the CMDN buffer, and including dynamic calcium buffering for TRPN. The amount of calcium bound to TRPN ($[Ca^{2+}]_{TRPN}$) is the fraction of TRPN units with calcium bound to its regulatory binding site ($CaTRPN$) multiplied by a constant maximum concentration of calcium ions that can bind to TRPN ($[Ca^{2+}]_{TRPN,max}$ = 0.07 mM), leading to

$$\frac{d[Ca^{2+}]_{TRPN}}{dt} = [Ca^{2+}]_{TRPN,max}\frac{dCaTRPN}{dt} \quad (1)$$

The definition for $[Ca^{2+}]_i$ from CRN model was modified in such a way,

$$\frac{d[Ca^{2+}]_i}{dt} = \beta^*_{Cai}\left(\frac{(-I_{pCa}-I_{Cab}+2I_{NaCa,i})\ A_{cap}}{2Fv_{myo}} - J_{up}\frac{v_{nsr}}{v_{myo}} + J_{diff,Ca}\frac{v_{ss}}{v_{myo}} - \frac{d[Ca^{2+}]_{TRPN}}{dt}\right) \quad (2)$$

where,

$$\beta^*_{Cai} = \frac{1}{1+\frac{[CMDN]K_{m,CMDN}}{[Ca^{+2}]_i + K_{m,CMDN}}}$$

and all other variables are as it is in the CRN AP model. Here Ca_{TRPN} from equation 1 has been computed from RDQ-MF 2020 model and is given as,

$$Ca_{TRPN} = B_{so}X_{so}(SL) + B_{nso}(1 - X_{SO}(SL))$$

where B_{so} and B_{nso} are the ratio of bounded TRPN units in the single-overlap zone (SO) and in the non-single-overlap zone (NSO), respectively, and $X_{so}(SL)$ is the function of the size of the single overlap zone that models the effect of SL changes. In this way, the bidirectional coupling was achieved by subtracting the effect of $\frac{d[Ca^{2+}]_{TRPN}}{dt}$ from $[Ca^{2+}]_i$ as shown in equation (2). Hence, an EM system of nonlinear equations can be produced that determines the coupling effect on AP, CaT and active contractions of a single cell.

2.2.4 Experimental data

Human experimental recordings used for EM coupled model calibration have been summarized in Table 2.1. A cardiac myocyte removed from its normal environment, where it interacts with several other cells, has a significant impact on its electrical and mechanical functionality (Pfeiffer *et al.* 2014). Therefore, it is very hard to translate the electro-mechanics recorded at an isolated cellular level to organ level. Hence, instead of employing data from a single cardiac myocyte, the model was calibrated using tissue level preparations that allow the myocytes

to be studied in an environment that more closely mimics how they are found in the heart. The optimized set of parameters was obtained on basis of time related biomarkers of F_{active} i.e., relaxation time at 50% and 90% of peak values (rt_{50}, rt_{90}), time to T_{max} (ttp), and twitch time (TT).

Table 2.1: Human Atrial experimental data used for calibration of EM coupling model. T_{max}: peak tension, ttp: time to peak tension, TT: twitch time, rt_{50}, rt_{90}: relaxation time at 50% and 90% of T_{max}, CaT: Calcium-transient.

Reference	Tissue preparation	Biomarkers
Schotten *et. al* 2002	Right atrial appendages from patients of mitral valve surgery (1Hz, 37°C, n=31)	T_{max}, rt_{90}
Schwinger *et al.* 1998	Right atrial trabeculae from patients who underwent aortocoronary bypass operations. (1Hz, 37°C, n=9)	T_{max}
Sossalla *et al.* 2009	Thin right atrial trabeculae were micro-dissected (n=79)	T_{max}, ttp, rt_{50}, rt_{90}
Maier *et al.* 2000	Right atrial trabeculae from patients undergoing aortocoronary bypass operation (37°C, n=15)	ttp, TT, rt_{50}, rt_{95}, CaT_{max}
Flesch *et al.* 1997	Isolated electrically driven (1Hz, 37°C) human right atrial trabecula from non-failing hearts. (n=15)	ttp, rt_{50}
Brixius *et al.* 1997	Right atrial tissue from patients having aortocoronary bypass surgery. (n=19)	ttp, rt_{50}, CaT_{max}
Schotten *et al.* 2006	Human atrial myocardium obtained from right atrial appendages at 1Hz, 37°C. (n=14)	T_{max}
Brixius *et al.* 1999	Auricular trabeculae were selected from right atrial tissue. Using Fura- 2 ratio method for Ca transient and force in muscle strips at 37°C, 1Hz.	T_{max}, T_{min}, $ttp_{Factive}$, $rt_{50Factive}$, CaT_{max}, CaT_{min}, ttp_{CaT}, rt_{50CaT}

2.2.5 Contraction parameter calibration

The coupled EM model was calibrated against human experimental recordings to achieve atrial-specific characteristics. Ca sensitivity plays a crucial role in assessing the mechanical behavior of the muscle other than the force-pCa curve. An increased Ca sensitivity indicates that the muscle requires less free Ca^{2+} to generate force but in this process many factors work in collaboration. The equilibrium dissociation constant, K_d (mM) is the ratio of dissociation K_{off} (ms^{-1}) to association K_{on} of Ca-TRPN. Human atrial myocytes have less Ca sensitivity hence providing increased K_d than ventricular myocytes (Morano *et al.* 1998). In accordance, K_d was manually tuned to value in a range of 0.5-0.86 µM as reported by (Robertson *et al.* 1981, Land & Niederer 2018).

In addition, XB cycling kinetics K_{basic} (ms^{-1}) was also optimized along with the value of K_{off}. Human atrial twitches and CaT are shorter in time than ventricles (Maier et al. 2000) therefore the optimization of model RU and XB kinetics parameters were achieved by using human atrial

experimental data as listed in Table 1 based on biomarkers of ttp, rt_{90}, rt_{50} and the beating frequency. The calibration of EM kinetics parameters has been shown in Figure 2.3 in the Results section. The calibration was performed using *fminsearch* optimization function to find local minima in Matlab. The model biomarkers were tuned in accordance with the experimental data to adopt atrial physiology.

2.3 Results

2.3.1 EM model characteristics

A comparison of AP, CaT, active isometric tension F_{active}, contractility for calibrated EM model (in red) with original CRN model (in blue) is illustrated in Figure 2.2. For CaT and F_{active} we have also included original RDQ-MF (in cyan) and un-calibrated EM model curves. The stimulus of 2 nA was applied at t = 50 ms to the cell for a duration of 2ms. Initial conditions were recorded by running the original CRN model at 1 Hz for 200 beats. The EM model was then run for 20 beats to achieve steady state.

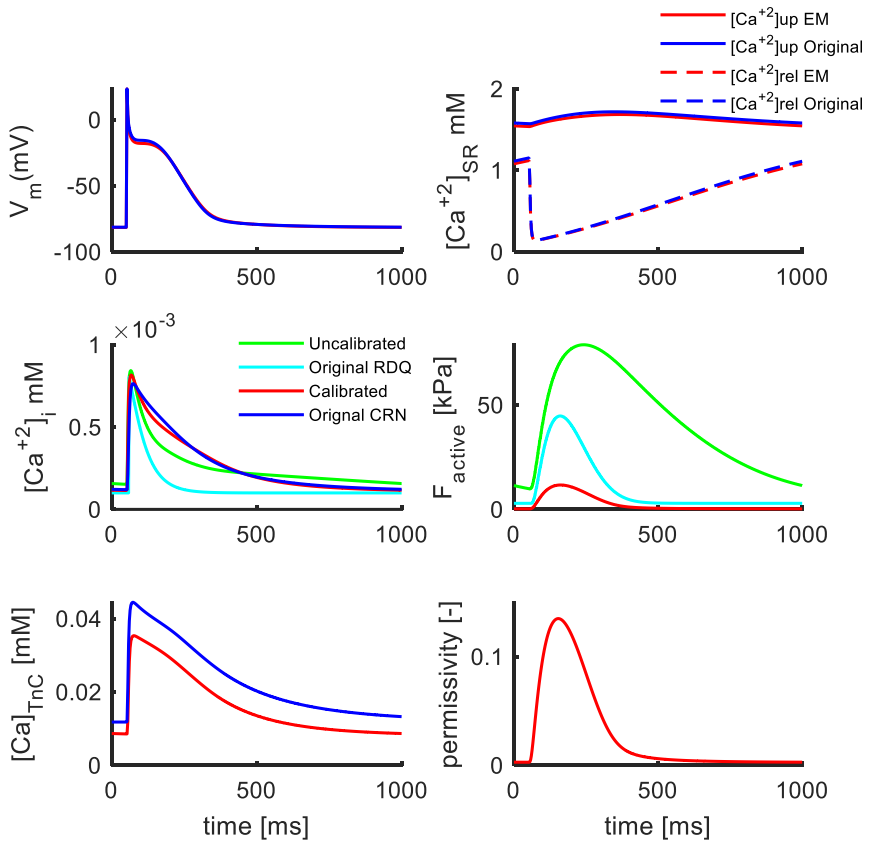

Figure 2.2: Simulation of EM coupled human atrial cell model (in red) vs original CRN model (in blue). Upper panel shows effect of contraction on AP, SR Ca^{2+} content. Middle panel shows CaT and F_{active} also including un-calibrated EM model i.e., RDQ-MF with CRN CaT (in green) and the original RDQ-MF model i.e., RDQ-MF with the analytically simulated CaT(in cyan). Lower panel shows Ca bound to TRPN and permissivity.

Coupling affects the AP by slight shortening of the early phase of repolarization as shown in Figure 2 top left panel. CaT of the calibrated model follows the original CRN trend (middle left

panel) with slightly elevated peak and shortening of early phase of decay. No change is seen by SR Ca^{2+} uptake. The middle right panel of Figure 2.2 also demonstrates F_{active} development with SL fixed at 2.2 µm. The calibrated tension twitch (in red) has fast activation and relaxation phases and a depressed peak than the uncalibrated (in green) and original RDQ-MF (in cyan) twitches. The lower left panel shows a reduction in Ca bound to TRPN peak than the original CRN which is the consequence of a slight increasing CaT peak. Another parameter, permissivity is the number of myosin heads that are in a permissive state, and it is proportional to the amount of force generated. The plot corresponds to a very small amount of permissive myosin heads.

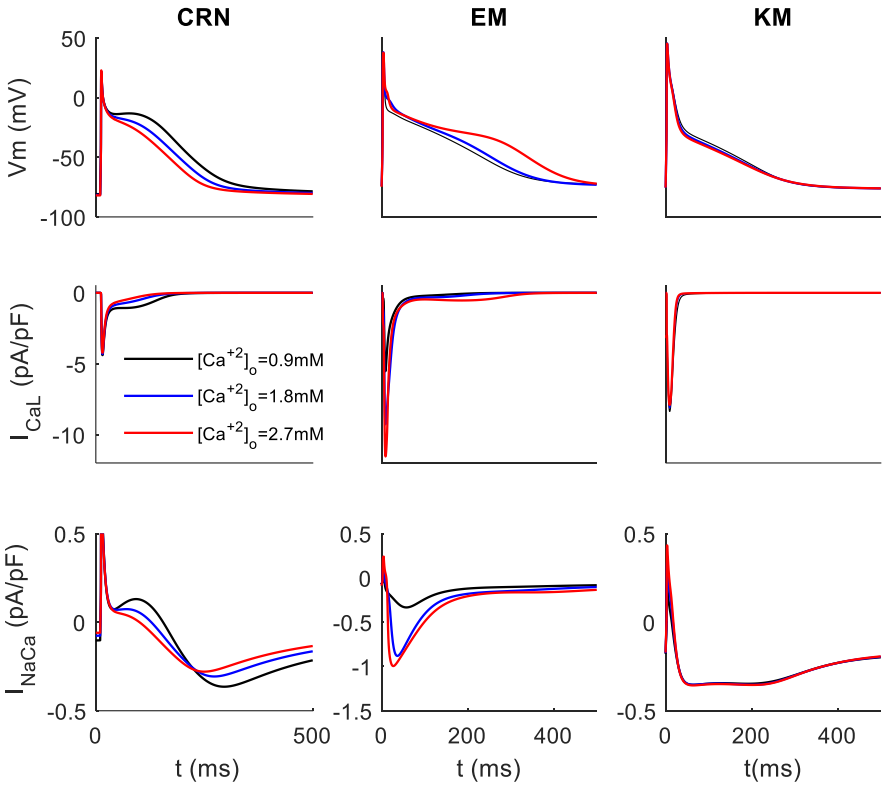

Figure 2.3: Comparison of AP (top), I_{CaL} (middle) and I_{NaCa} (bottom) obtained with three human atrial AP models (CRN, EM and KM) baseline codes for $[Ca^{2+}]_o$=[0.9 (black), 1.8 (blue), 2.7(red)] at steady state (600s and BCL=1000ms).

2.3.1.1 $[Ca^{2+}]_o$-APD relation for AP model

The hypothesized effect is the inverse relation between APD and $[Ca^{2+}]_o$ suggested by experimental AP recordings from human atrial myocyte superfused with 1.2 mM and 2.0 mM $[Ca^{2+}]_o$ (Severi *et al.* 2009). The three human atrial models that were run at three different $[Ca^{2+}]_o$ values is shown in Figure 2.3. The graph depicts AP V_m (top panel), I_{CaL} (middle panel), and I_{NaCa} (bottom panel) trends in steady state. CRN and KM models have similar behavior in terms of APD i.e., inverse relation to changing $[Ca^{2+}]_o$ but CRN is more sensitive to $[Ca^{2+}]_o$ variations then KM model. On the other hand, EM model shows a largely direct dependence of APD with $[Ca^{2+}]_o$. The reduced I_{CaL} plateau is observed in CRN model whereas the KM model current does not show any significant dependence on $[Ca^{2+}]_o$. The inward current of exchanger I_{NaCa} shows a biphasic dependence on $[Ca^{2+}]_o$ variations for CRN i.e. it is increasing in the initial phase of AP and then

decreasing during repolarization phase. In EM model, I_{CaL} is increasing with respect to both peak and plateau whereas, I_{NaCa} shows a decreasing inward current. Hence, a difference of Ca^{2+} homeostasis can be seen in three human atrial models.

The quantification of the CDI mechanism was carried out using the AP-clamp technique where currents were analyzed for two different scenarios: for both CDI+VDI mechanisms and for VDI only where CDI gate was turned off. The integration of I_{CaL} current trend with $[Ca^{2+}]_o$ variations can be appreciated in Figure 2.4. Here both KM and CRN shows slightly increasing slope under CDI+VDI and completely flat curves under VDI only. On the other hand, the CDI mechanism has a strong impact on the EM model, dramatically changing how the amount of charge carried by I_{CaL} depends on $[Ca^{2+}]_o$ (compare continuous and dashed red lines in Figure 2.4). Nevertheless, the EM model still does not correctly reproduces the APD-$[Ca^{2+}]_o$ relation (Figure 2.3 AP traces). To better understand the cause, the DF was made independent of Ca^{2+} concentrations. In this configuration the EM model shows an opposite behavior (Figure 2.4, dotted red line) proving that CDI is effective in decreasing the current upon increase of $[Ca^{2+}]_o$, however, this is overcome by the opposing effect of $[Ca^{2+}]_o$ modulation of DF, leading to the resulting AP prolongation.

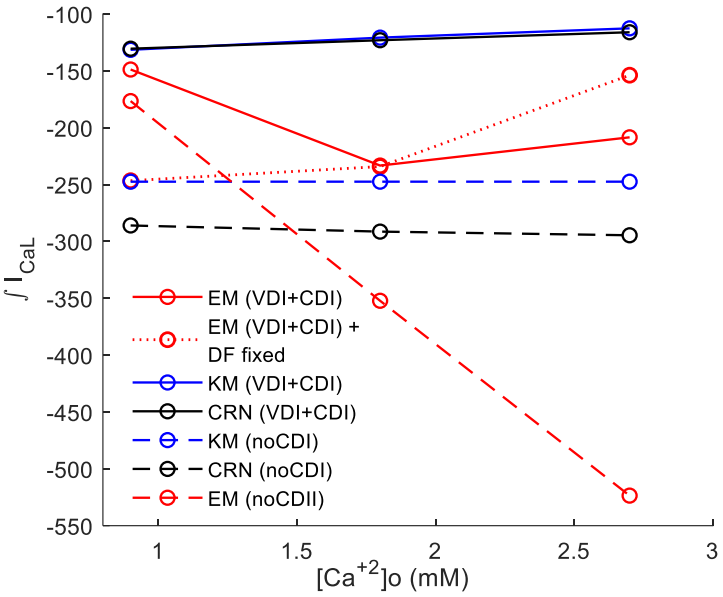

Figure 2.4: Integration of I_{CaL} current under AP-clamp for all three human atrial AP models for CDI+VDI and noCDI conditions. For EM model an extra test of with and without fixed driving force (DF) was simulated.

2.3.3 APD rate adaptation

The rate adaptation of APD at 90% of repolarization was compared for the coupled EM model with original CRN and the experimental data for human atrial cardiomyocytes as shown in Figure 2.5. The data demonstrate a wide range of heterogeneity as at basal cycle length of 1sec APD_{90} can vary from 370 to 240 msec. In the experiments, most of the data express a sharp shortening of APD_{90} since the AP was least affected by the coupling (Figure 2.2) hence, there was no substantial difference between the coupled (in red) and original AP model (in blue). The model

demonstrates a biphasic APD_{90} rate dependence shortening which gets steeper after BCL 1sec. Hence, as already been explained in detail in the original work (Courtemanche *et al.* 1998), the major contributor of rate adaptation of APD_{90} was the rate dependent reduction in I_{CaL} current that reduces the plateau and accelerates the repolarization phase hence reduces the I_K activation (not shown).

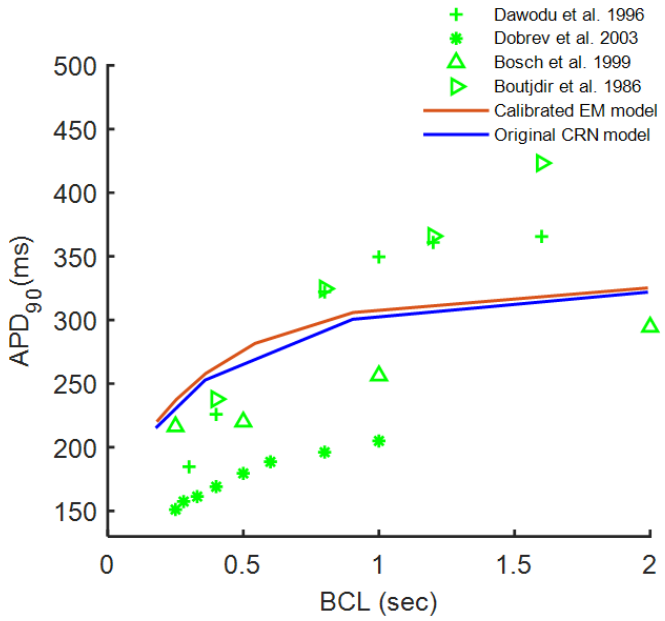

Figure 2.5: Rate adaptation trend of APD_{90} for EM coupled and original CRN model compared with experimental data.

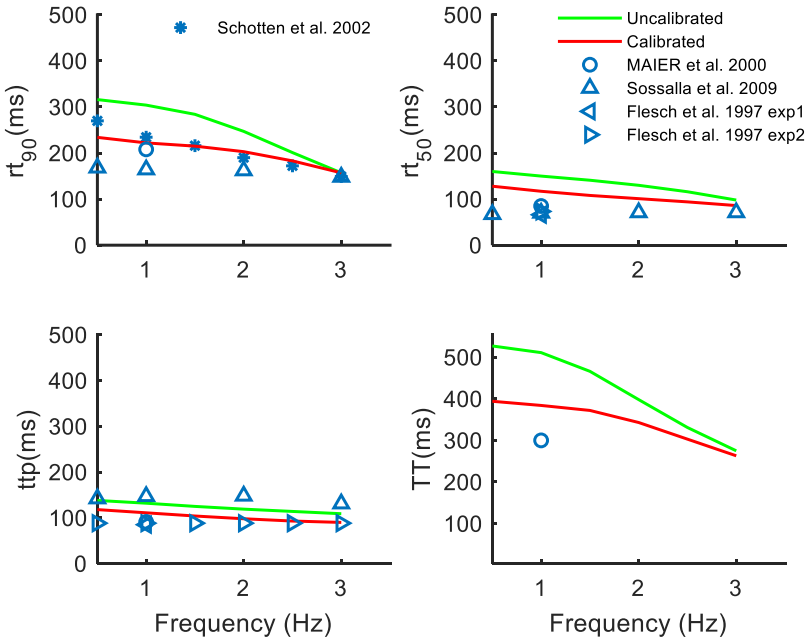

Figure 2.6: EM model kinetics calibration based on biomarkers extracted from human atrial experimental data.

2.3.4 Force frequency relationship

EM model was calibrated based on the biomarkers as described in Methods section 2.2.5 and shown in Figure 2.6. After calibration the kinetics of EM model were tuned as follows: K_d=0.865 s^{-1}, K_{off}=180 s^{-1} and K_{basic}=20 s^{-1}. This calibration effect has already been depicted in Figure 2.2. Moreover, the model cooperativity was also slightly enhanced by making γ=20. In terms of biomarkers, the comparison of the calibrated model with the un-calibrated one can be seen in Figure 2.6. The un-calibrated model shows slower kinetics i.e., a delayed ttp, slow relaxation rt_{50} and rt_{90} and a large TT. Thus, the calibration of contraction parameters accelerates the twitch kinetics and the twitch peak is also achieved earlier. The late relaxation phase has demonstrated a shift of slope for rate dependent acceleration of relaxation (FDAR) phenomena which is also evident in mammalian ventricular muscles (Schouten, 1990, Pieske et al., 1995, Hussain et al., 1997). The inotropic response of the model was assessed by running the model at frequencies varying from 0.5 to 3Hz. Rate adaptation by the coupled model demonstrates a negative inotropic effect as shown in Figure 2.7 (left panel). All the experimental data shows a positive dome-shaped force-frequency relation where the mean maximal force is achieved at the mid frequency of 2Hz whereas the coupled model is not following this trend. On the right, CaT generated from the AP model has been plotted in the systolic phase which also depicts a decreasing trend with increase in frequency and is in accordance with the AP model CaT trend with frequency.

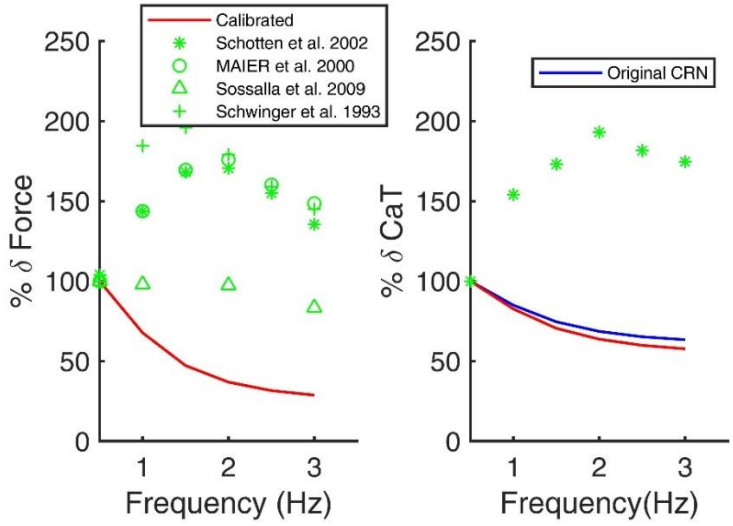

Figure 2.7: Force (left) and CaT (right) plotted with respect to frequency for coupled and calibrated EM model

2.4 Discussion and Conclusions

In this study, a strongly coupled EM model of human atrial myocytes has been presented by the integration of existing human cellular AP and contractility model. In particular, the model incorporates the modulatory effect of contraction on AP and CaT by adding the feedback of Ca-TRPN buffering on AP model. To have more atria-specific behavior of the EM model the calibration of twitch kinetics was performed in accordance with human atrial experimental data as shown in Table 2.1. For this purpose, a collection of available data from human atrial trabeculae at body temperature has been presented. The interacellular-Ca^{2+} homeostasis dependence on

varying $[Ca^{2+}]_o$ was compared for the existing human atrial models by highlighting some insight mechanisms that are quite variable among the models.

The $[Ca^{2+}]_o$ variations based simulation revealed that among the analyzed human atrial models CRN and KM qualitatively reproduce the real behavior of cells whereas EM does not. The major current contributing to the overall APD trend is I_{CaL}, but $[Ca^{2+}]_o$ influences I_{CaL} in two opposing ways by modulating DF and CDI. *In-silico* analysis allowed us to precisely quantify these contributions in terms of changes in the amount of depolarizing charges carried into the cell by the current (Figure 2.4).

The investigation pointed out that one of the two mechanisms ($[Ca^{2+}]_o$ modulation of DF) is not acting in CRN and KM. Indeed in the I_{CaL} formulations of these models, the DF is not dependent at all on $[Ca^{2+}]_o$. Of course, this description is not realistic, and the right behavior of CRN and KM is actually relying on an incorrect assumption. On the other hand, the EM model behaves completely the opposite of real cells. *In-silico* analysis allowed to quantify the reasons: the $[Ca^{2+}]_o$-induced modulation of I_{CaL} DF produces a large direct dependence of the current (here DF is the only $[Ca^{2+}]_o$ modulated mechanism) while the CDI can induce only a modest inverse relationship (see dotted line in Figure 2.4, here CDI is the only $[Ca^{2+}]_o$ modulated mechanism). When both mechanisms are in place the former prevails (Figure 2.4 continuous line) yielding the wrong behavior.

The main findings of the coupled model analysis are the negative inotropic response of the model with respect to changing rate. A further investigation demonstrated a decreasing CaT with respect to increasing rate generated by both CRN and our model. The positive force-frequency relation is associated with a powerful continuous increase in Ca uptake by SR as reported by *in-vivo* experiments (Maier *et al.* 2000). This mismatch of the *in-silico* model with the *in-vivo* experiment highlights the limitation of the AP model choice. CRN model has a simplistic representation of SR compartments that is far from the actual arrangement of complex SR structure. Therefore, there is a need for an AP model with a more detailed spatiotemporal Ca-gradient representation like Koivumäki 2011 (Koivumäki *et al.* 2011) model. This choice will come up with an obvious increased computational complexity by adding more state variables in the EM model and that would create difficulty of scaling up our cellular level model to tissue level. Therefore, a tradeoff between complexity and biophysically detailed AP model can be achieved by employing an update of CRN model like an initial attempt by Colman (Colman *et al.* 2013) model that incorporates a simplified but still detailed form of Ca^{2+} handling developed in KM model.

Overall, the study concludes that a need for a new computationally efficient human atrial AP model as a future choice for EM coupling that should have a correct representation of Ca^{2+} homeostasis so that it would be able to reproduce correctly the $[Ca^{2+}]_o$ dependence and the inotropic response of rate. Moreover, more experimental data are required to draw conclusions about the cardiac phenomena and not only on the models developed to describe them.

Chapter 3

A Detailed Mathematical Model of the Human Atrial Cardiomyocyte: Integration of Electrophysiology and Cardiomechanics

The content of this chapter is re-produced from:

"A Detailed Mathematical Model of the Human Atrial Cardiomyocyte: Integration of Electrophysiology and Cardiomechanics."

***Fazeelat Mazhar**, Chiara Bartolucci, Francesco Regazzoni, Michelangelo Paci, Cristiana Corsi, Luca Dedè, Alfio Quarteroni, and Stefano Severi.*

Under revision in Special Issue 'Cardiac Mechano-Electric Crosstalk' in Journal of Physiology.

"A Novel Human Atrial Electromechanical Cardiomyocyte Model with Mechano-Calcium Feedback Effect."

***Fazeelat Mazhar**, Francesco Regazzoni, Chiara Bartolucci, Cristiana Corsi, Luca Dedè, Alfio Quarteroni, and Stefano Severi.*

Computing in Cardiology. IEEE 2022

Abstract

Mechano-electric regulations play an important role in the maintenance of cardiac performance. Mechano-calcium and mechano-electric feedback pathways adjust the cardiomyocyte contractile force according to mechanical perturbations and contribute to affect electrophysiology. Electro-mechanical coupling integrates all these regulations in one unit resulting in a complex phenomenon where it becomes difficult to quantify the role of its individual components. Computational modeling is a useful tool to accelerate the mechanistic understanding of complex experimental phenomena. A novel EM model developed for human atrial cardiomyocytes with proper consideration of feedforward and feedback pathways has been presented in this chapter. The model integrates a modified version of the electrophysiology model by Koivumäki with the contraction model by Quarteroni group and is named *MBS2022*. The model simulates iso-sarcometric and isometric twitches and the effects of feedback on forward electrophysiology and Ca-handling. In-line with experiments, the model showed a biphasic response of Ca^{2+} transient (CaT) peak to increasing pacing rates. The effect of CaMKII based activations is also identified and its effect on rate dependency has been quantified. Overall, the developed model provides a physiological CaT followed by a physiological twitch having biomarkers in agreement with human atrial data. This model can open pathways for future studies of human atrial electromechanics.

3.1 Introduction

At each heartbeat, dynamic changes induced by the mechanical load are intrinsically regulated by the heart (via Frank Starling and Anrep effects) to maintain the cardiac output. Likewise, at the cellular level these mechanical changes regulate the electrical activity (Kohl *et al.* 2000) and the Ca^{2+} handling (Calaghan & White 1999, Neves *et al.* 2015) under both physiological and pathological conditions (Varela *et al.* 2020, Pfeiffer *et al.* 2014, Ravens 2003, Taggart & Sutton 1999). The changing contractile force affects the action potential via mechano-electric feedback (MEF) (Nazir et al. 1996; reviewed in Peyronnet *et al.* 2016, reviewed in Quinn & Kohl 2020). However, to investigate the influence of MEF effect, the strong coupling of electrophysiology and cardiomechanics within the cardiomyocyte, which is referred to as electro-mechanical coupling (EM), must be considered. Within the EM coupling, the dynamic response of Ca^{2+} sequestration by troponin (TRPN) on the electrophysiology is termed mechano-calcium feedback (MCF) (Rice et al. 1999). These feedforward and feedback pathways can be conceptualized using Figure 1.1.

EM coupling is a series of events triggered by the membrane depolarization and the development of the action potential (AP), followed by the Ca^{2+} release from the sarcoplasmic reticulum (SR) via the Ca^{2+}-induced-Ca^{2+}-release (CICR) mechanism. The Ca^{2+} release is responsible for initiating contraction by the activation of thin filaments i.e., the regulatory units (RUs) followed by the cooperativity of RU proteins, and eventually leading to cross bridge cycling (XB_{cy}). This regulation hence depicts a complex phenomenon making it challenging to understand and to quantify the role of individual components in the integrated system. The development of a sophisticated cardiac mathematical model can help to have a better insight into these complex experimental phenomena (Vagos *et al.* 2018).

Several atrial computational models have been developed to improve the understanding of individual components of EM coupling: the electrophysiology (reviewed in Heijman *et al.* 2016 and Wilhelms *et al.* 2013) and the Ca^{2+} handling (reviewed in Sutanto *et al.* 2020). However, in the literature, the focus of cardiomechanics study (reviewed in Regazzoni *et al.* 2021; Niederer *et al.* 2019) and its modeling (reviewed in Trayanova *et al.* 2011) was more on ventricular cardiomyocytes (CMs). Similarly, integrated EM models were developed and were based either on ventricular electro-mechanics (Timmerman *et al.* 2017; Margara *et al.* 2020; Bartolucci *et al.* 2022) or stem cells derived CMs (Forouzandehmehr *et al.* 2021). With the availability of human atrial cellular data, interest in atrial specific EM modeling has increased. The very first attempt was made by Land (Land *et al.* 2018) to study the influence of human atrial mechanics during atrial fibrillation (AF) on the whole heart model. However, not every contraction parameter was re-tuned according to human atrial physiological contraction data. Few atrial cell level EM models were developed, for instance, EM model by Zhan (Zhan *et al.* 2013; Zhan *et al.* 2017) is more focused on the impact of fibroblast on EM coupling and contraction. Another EM model was developed by Kuijpers (Kuijpers *et al.* 2008) and later by Brocklehurst (Brocklehurst *et al.* 2015) but its cell level mechanism was not validated quantitatively against any human atrial *in-vitro* data. Importantly, all the EM models used the gold standard AP model in human atrial modeling i.e., the Courtemanche (CRN) (Courtemanche *et al.* 1998).

Following the current EM modeling approach, in one of our previous studies (Mazhar *et al.* 2021) (Chapter 2 in the thesis), we developed an EM model of human atrial CM by coupling the Courtemanche AP model and the contraction model by the Quarteroni group, RDQ2020 (Regazzoni *et al.* 2020). However, this coupled and calibrated model was not able to reproduce one of the important phenomena, the force-frequency relationship for human atrial CMs. The reason for this discrepancy was seen in the Ca^{2+}-transient rate adaptation trend, which in turn likely depends on the atrial specific physiological phenomena of CICR propagation from the membrane to the center in a Ca^{2+}-wave like fashion by a "fire-diffuse-uptake-fire mechanism" (Blatter 2017; Bootman et al. 2006). Hence, there is a need to have a model with a calibrated Ca^{2+} handling dynamics that remains valid upon rate changes.

Our aim was to develop an EM human atrial cell level model that is computationally efficient and exhibits a detailed temporal Ca^{2+} handling description that is valid over a physiological range of frequencies. In addition, to the current knowledge, this is the first human atrial EM model that includes mechano-electric regulatory loop and is calibrated against a wide collection of available human *in-vitro* data. The model was designed to present coupling and mechanical load effects on electrophysiology, on Ca^{2+} transient (CaT), and on the active force (F_{active}). In this way, it can be used to determine the possible role of MEF towards the initiation of atrial arrhythmias by varying stretch levels. The model is named *Mazhar-Bartolucci-Severi 2022* (MBS2022) onward.

3.2 Methods

With respect to EM coupling between AP and contraction modules, two types of pathways can be identified i.e., feedforward, the input of CaT to the contraction module; and feedback, the sequestration of Ca^{2+} bound to troponin (MCF) from the free cytosolic CaT. In this way, a strong

bidirectional coupling was ensured in MBS2022 model. The section 3.2.5 Electro-mechanical coupling highlights this stepwise approach for introducing MCF effect in the model. Moreover, the calibration of contraction and Ca^{2+} handling parameters was carried out to achieve a model within a physiological range of human atrial *in-vitro* data (references in Table 3.1, 3.2).

3.2.1 Parent AP model: Koivumäki 2011

KM2011 (Koivumäki *et al.* 2011) is a human atrial model that reproduces the principal characteristics of Ca^{2+} dynamics that is evident by the biphasic rise of the Ca^{2+}-transient resulting from delay between junctional and bulk SR release. This development was a breakthrough in the human atrial AP models since it has a detailed fire-diffuse-uptake-fire (FDUF) (Blatter 2017) propagation of Ca^{2+} diffusion. The model is based on a multi-compartmental setup for cytosolic and SR, where the compartment near to the membrane is the subspace (*ss*) and the rest of the bulk is divided into four bulk (*bc*) compartments (three for SR) as shown in Figure 3.1 (left). Other than diffusion, the centripetal movement of Ca^{2+} ions is carried out by mobile buffers having mobility and dissociation coefficient (K_d) of calmodulin (CMDN). In the SR, the Ca^{2+} buffering to and uptake by the SERCA is fitted based on Ca^{2+} transient kinetics and SR Ca^{2+} contents. Thus, an AP model with the detailed description of Ca^{2+} dynamics might increase the computational load when coupled with a biophysically detailed model or scaled up to multicellular level.

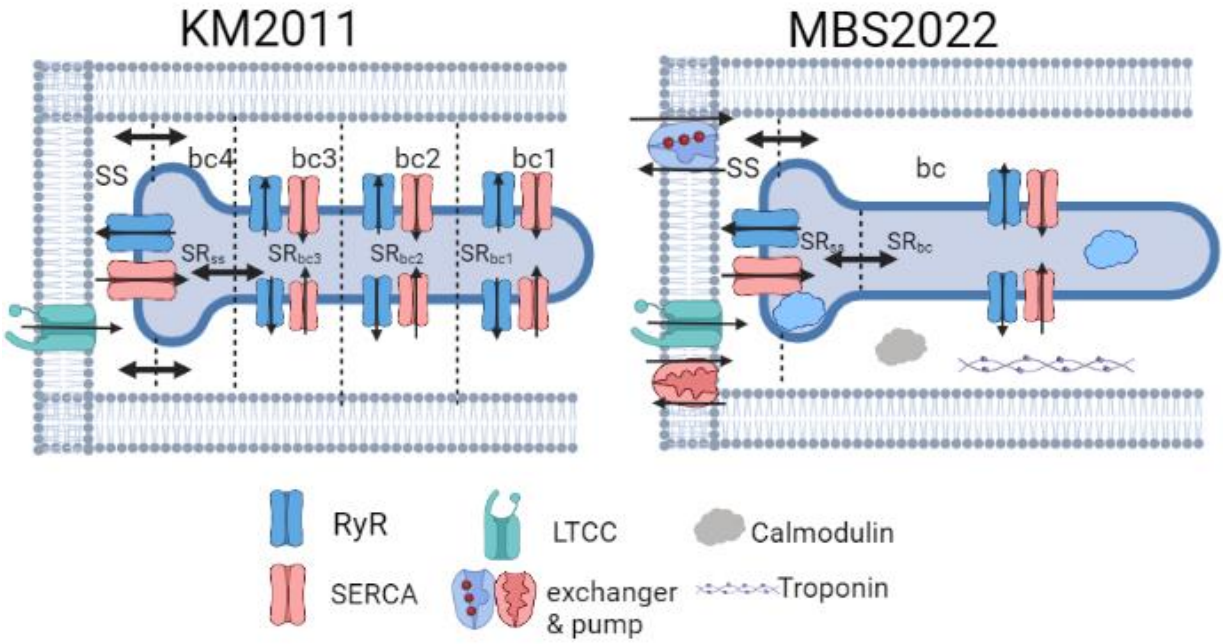

Figure 3.1: Model description and comparison of Koivumaki (KM2011) model schematic with MBS2022 model schematic.

3.2.2 Cell structure of the MBS2022 model

MBS2022 is an electromechanically coupled model where the coupling is based on two modules: the AP module obtained from a considerable level of modifications in the human atrial cell model KM2011; and a mean-field approximation-based contraction module, RDQ2020

(Regazzoni *et al.* 2020). MBS2022 model has inherited the complex Ca^{2+} handling dynamics of atria (Blatter *et al.* 2003; Bootman *et al.* 2011; Hüser *et al.* 1996; Hatem *et al.* 1997) based on the multi-compartmental structure of KM2011 AP module. The multi-compartmental structure of cytosol and SR in KM2011 was reduced and we were left with two compartments only i.e., the sub-space (*ss*) and the bulk cytosol (*bc*) (for comparison with parent model see Figure 3.1). A detailed schematic diagram of our human atrial EM model illustrating this updated compartmental setup is shown in Figure 3.2.

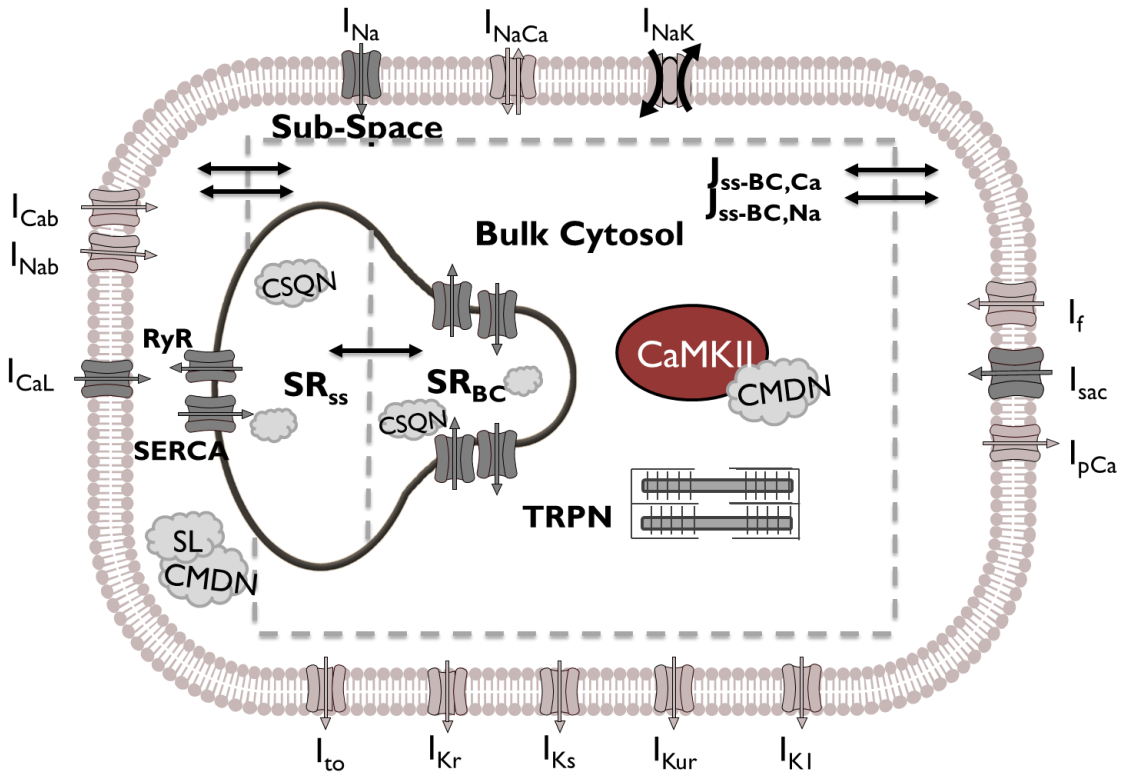

Figure 3.2: Schematic diagram of human atrial myocyte model. The figure shows two cytosolic compartments, the subspace (*ss*) and bulk cytosol (*bc*). The *bc* compartment is enclosed inside a grey dashed line box. The sarcoplasmic reticulum (SR) includes two compartments SR_{ss} and SR_{bc} with their own release (RyR) and uptake (SERCA) units. The cytosolic buffers are troponin (TRPN), calmodulin (CMDN) and sarcolemmal phospholipids (SL). The sarcolemmal currents and fluxes in dark grey were modified/ reformulated/added in our novel model MBS2022.

The cell dimensions for the parent AP model KM2011 were adopted from Nygren (Nygren *et al.* 1998). In comparison to the human atrial cell dimensions (Neef *et al.* 2010; n=115), the model cell length was slightly longer (122.051µm vs 101.15±1.5 µm) and radius was a bit narrow (6.5µm vs 7.4±0.3 µm). Thus, the total cell capacitance (50pF) seems to be lying in the lower whisker of the box plot in Figure 3.3 showing the cell capacitance value being used in human atrial experiments (references are in Table A2). We found a very large variability in such data, ranging from 29.6±1.8 pF, as reported by the Nattel lab (Wang *et al.* 1999) up to 114.8±5.9 pF reported by Voigt et al. (Voigt *et al.* 2012). This variability in cell capacitance value can be associated with the t-tubules density present in the cell that affects the capacitance-to-longitudinal surface area (C/A), reported to range from 1 to 10% in human atrial cell (Fakuade *et al.* 2020; n=50). The

dimensions for MBS2022 cell model were modified in accordance with the experimental values (Neef *et al.* 2010). Since there was a 12% increase in radius, with respect to KM2011, we made an similar rise in the capacitance providing new capacitance, upto 56pF. The low C/A ratio (≅1%) implies an assumption of a low T-tubule density.

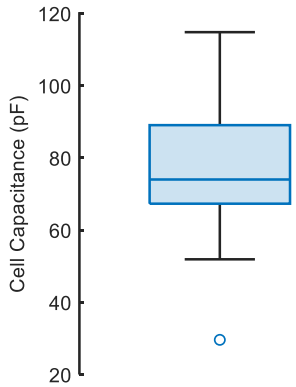

Figure 3.3: Cell capacitance trend used in human atrial myocytes with references in Table A2. The top and bottom whiskers are enclosed within 51.9 to 114.8pF range. The outlier at 29.6pF is shown by an open circle.

The cytosolic space was re-arranged in such a way that the *ss* compartment was at a distance of 0.02 µm from the membrane (as in KM2011); the rest of the area in the bulk/center was summed up to form *bc* compartment so that the *bc* was 6.6 µm deep from the *ss*. In this way, the *bc* compartment volume (V_{bc}) was 163 times larger than the volume of *ss* compartment (V_{ss}). Similarly, SR was divided into two compartments i.e., SR_{ss} that lies near the membrane and SR_{bc} that is more towards the center, each having its own release RyRs and uptake SERCAs units. The total volume of SR was kept same as it was in KM2011 whereas, the volume space dedicated to *ss* (V_{SRss}) and *bc* (V_{SRbc}) was redefined. Since now, V_{SRbc} was the formed by contribution of ¾ part of the cytosolic *bc* compartment therefore, V_{SRss} was now a sum of cytosolic subspace volume V_{ss} and ¼ part of *bc*. Hence, the V_{SRbc} was 1.26 times larger than V_{SRss}. In this way, the contribution of Ca^{2+} storage in SR_{ss} was enhanced towards the formation of global cytosolic CaT.

The diffusion of Ca^{2+} and Na^{+} in the cytosolic compartments has also been shown in Figure 3.2. In addition, all of the intracellular electrolyte concentrations were dynamic except $[K^{+}]_i$ which was fixed to 134 mM since it was necessary to have a steady-state stable value of the electrolyte concentrations (Barral *et al.* 2022).

3.2.3 Ca^{2+} handling and diffusion

3.2.3.1 Ca^{2+} in the cytosol

In KM2011, cytosolic Ca^{2+} diffusion from the *ss* to *bc* region was an analytical diffusion equation. The diffusion distance $x_{ss\text{-}bc}$ was computed from the center of *ss* to the center of 1st *bc* compartment. In MBS2022, the center of *bc* compartment was shifted to deep inside i.e., from 0.8125 µm to 3.3 µm (from 1/8 to 1/2 of the updated *bc* compartment) from the membrane. As a result, using this new distance value resulted in a 75.3% increase in diffusion distance that will eventually lead to a significant slowing of diffusion. On the contrary, Ca^{2+} diffusion is faster in

atria than in ventricles therefore, it cannot be a slow process physiologically (Tanaami *et al.* 2005). Hence, in our model diffusion distance was kept as it is i.e., 0.8125µm to have a fast diffusion of Ca^{2+} in the cytosol. KM2011 has a single arbitrary cytosolic buffer whose dissociation coefficient K_d and concentration value corresponds to the characteristics of CMDN. For bidirectional coupling, TRPN was included in the cytosol with the existing CMDN buffer (Ji et al. 2015). The detail of bidirectional coupling of AP and contraction module has been described in the section 3.2.5 Electro-mechanical coupling. The Ca^{2+} diffusion via mobile buffer in the *bc* compartment was no longer needed in our model since MBS2022 has a single *bc* compartment now. The absence of mobile buffers and the functional T-tubules in the model makes Ca-SR release the main source of spatial spread of Ca^{2+} signal other than the diffusion as can also be seen in experiments (Walden *et al.* 2008). Hence, the differential equations for both free intracellular Ca^{2+} ($[Ca^{2+}]_i$) and Ca^{2+} in SR ($[Ca^{2+}]_{SR}$) were modified.

3.2.3.2 Ca^{2+} in the SR

Inside the SR, the bidirectional SERCA pumping and buffering have the same formulation as the KM2011 model. Other than this, in KM2011, the numeric value of SERCA buffer affinity was adopted from ventricular myocytes as reported in (Shannon *et al.* 2000). However, an increased SERCA activity with fast uptake dynamics was found in atria (Walden *et al.* 2008). The SERCA affinity formulation is based on the regulatory protein phospholamban (PLB) and SERCA expression levels as shown in (Koivumäki *et al.* 2009). A low level of SERCA inhibitory protein (PLB) along with high SERCA expressions eventually leads to raised affinity of SERCA buffer for human atria (Bokník *et al.* 1999). Moreover, less PLB inhibition of SERCA directly impacts the SERCA dynamics too. Hence, the affinity of SERCA buffer was modified to meet human atrial SERCA activity level (Koivumäki *et al.* 2014 Supplementary Section).

On the release side, RyR channel has a Hodgkin-Huxley type formulation in KM2011 that consists of activation, inactivation and an adaptation gate. The adaptation gate adapts the RyR open probability according to the intracellular Ca^{2+} environment. Since the intracellular Ca^{2+} levels have been modified now, RyR adaptation level was adjusted accordingly to maintain physiological level of Ca^{2+} both in the cytosol and in the SR. In the *bc* compartment, MCF introduced by the inclusion of TRPN-like fast buffer resulted in a depression of Ca^{2+} peak levels and a slowing of relaxation kinetics (Smith *et al.* 2019; Michailova *et al.* 2002). This lowering of Ca^{2+} peak was the consequence of less release flux J_{rel} from the RyR in the *bc* compartment. Hence, an adjustment of Ca^{2+} release was required to have a physiological level of CaT. For the systolic value, we acted upon adaptation parameters of *bc* compartment i.e., the saturation level and the sensitivity of adaptation. The saturation value was reduced so that release gate activation may saturate at a lower $[Ca^{2+}]_{bc}$ value and adaptation was made more sensitive. On the other hand, the relaxation kinetics were more dependent on contraction dynamics modeled by RDQ2020. Therefore, an automatic optimization was carried out for the time related biomarkers relevant to contraction. This was elaborated in the section Optimization of Contraction parameters.

3.2.4 Sarcolemmal ionic currents

Few of the sarcolemmal currents were re-formulated, modified or newly included in comparison to KM2011 model as reported in dark grey in the schematic of Figure 3.2. Inward

sodium current I_{Na} was reformulated according to new experimental data as described in (Skibsbye *et al.* 2016). Another membrane current, L-type Ca^{2+} I_{CaL} gating was modified as explained in (Koivumäki *et al.* 2014) (KM2014). In comparison to KM2014, steady state inactivation for fast voltage dependent inactivation (VDI) gate was adopted back from KM2011 to avoid irregular reactivation of I_{CaL} current at the lower frequency of 0.5 Hz. As a result, the I-V curves for both KM2011 and KM2014 versions were compared with data (Li *et al.* 1997) under voltage clamp protocol in Figure 3.4. Our modified formulation is in more agreement with the experimental data as of KM2014.

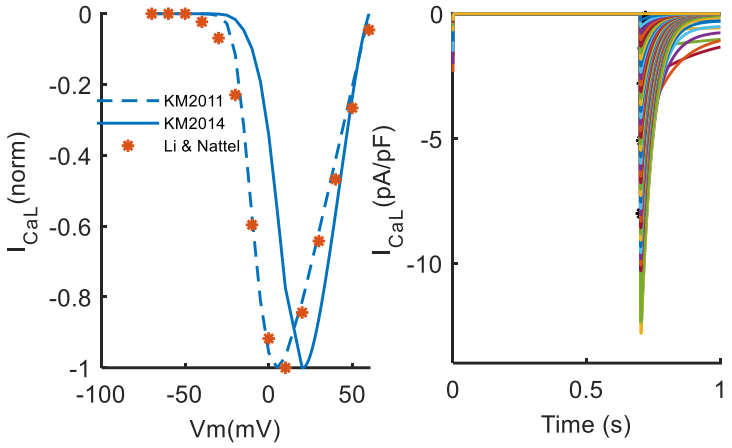

Figure 3.4: Voltage clamp protocol reproduced from (Li et al. 1997). Left panel shows I-V plot for two different formulations i.e., the modified KM2011 used by MBS2022 (in dashed line) and the KM2014 (in solid line) in comparison to the experimental data points.

Apart from the voltage dependent membrane currents, MBS2022 also includes mechanically activated channel (MAC) by the inclusion of stretch activated current as non-selective cations. A detailed description of MEF effect in MBS2022 model will be presented in Chapter 5 here we will consider all the simulations under iso-sarcometric condition where the sarcomeres were in stretched state with a constant length (SL) of 2.2µm.

3.2.5 Electro-mechanical coupling

Using the AP module as a modified version of KM2011 and the contraction module from RDQ2020, we constructed a coupled EM description of human atrial myocytes, MBS2022. The CaT from the AP module served as an input to the contraction module in a feedforward manner and the dynamic effect of Ca^{2+} bound to TRPN ($\frac{d[Ca^{2+}]_{TRPN}}{dt}$) from the contraction module was feedback to the free CaT in the AP module i.e., the MCF. In this way, a bidirectional strong electro-mechanical coupling was ensured (also shown in Chapter 2). Mathematically, the integration of modified KM2011 with RDQ2020 was performed in accordance with Ji and Timmermann(Ji et al. 2015; Timmermann et al. 2017). We defined the amount of calcium bound to TRPN ($[Ca^{2+}]_{TRPN}$) as, the fraction of TRPN units with calcium bound to its regulatory binding site ($CaTRPN$) multiplied by a constant maximum concentration of calcium ions that can bind to TRPN ($[Ca^{2+}]_{TRPN,max}$ = 0.56 mM), leading to:

$$\frac{d[Ca^{2+}]_{TRPN}}{dt} = [Ca^{2+}]_{TRPN,max} * \frac{dCa_{TRPN}}{dt} \quad (1)$$

where the $[Ca^{2+}]_{TRPN,max}$ was set to the minimum concentration allowed for 50% of accessible volume (Fabiato *et al.* 1983; Robertson *et al.* 1981). The differential equation for $[Ca^{2+}]_i$ was modified after adding troponin feedback from contraction module. $CaTRPN$ from Equation (1) is computed from RDQ2020 as follows:

$$Ca_{TRPN} = B_{so}\, X_{SO}(SL) + B_{nso}\big(1 - X_{SO}(SL)\big) \quad (2)$$

where B_{so} and B_{nso} are the ratio of bounded TRPN units in the single-overlap zone (SO) and in the non-single-overlap zone (NSO), respectively, and $X_{so}(SL)$ is the function of the size of the single overlap zone that models the effect of sarcomere length (SL) changes. On the one hand, B_{so} was already modeled in the original RDQ2020 model as:

$$B_{so} = \sum_{\alpha,\beta,\delta} \pi(\alpha,\beta,\delta,B)$$

where $\pi(\alpha,\beta,\delta,B)$ is the ratio of TRPN being permissive, regardless of the state of the tropomyosin (Tm) triplet α,β,δ. On the other hand, we introduced the variable B_{nso}, whose dynamics is modeled as:

$$\frac{dB_{nso}}{dt} = k_{on}\frac{[Ca^{2+}]_i}{k_D(SL)}\,(1 - B_{nso}) - k_{off}B_{nso}$$

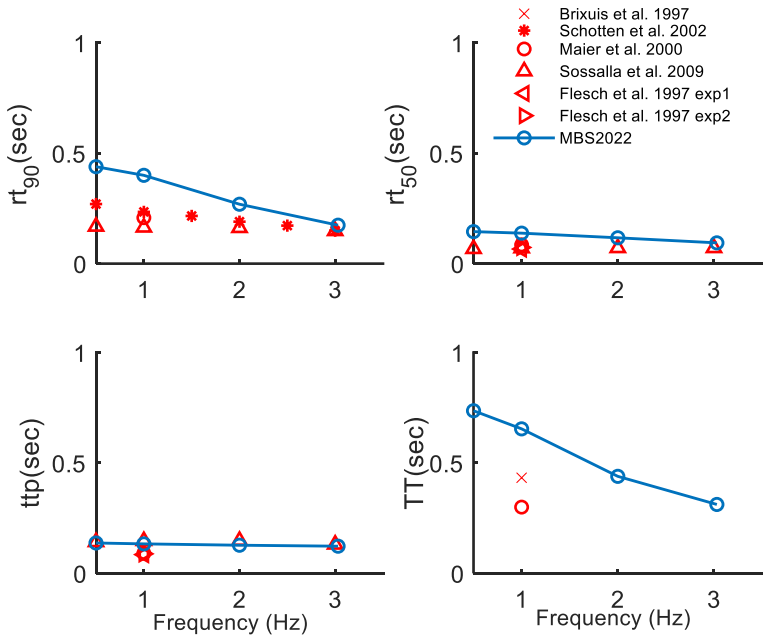

Figure 3.5: Frequency dependent acceleration of relaxation of F_{active} biomarkers. The experimental data reported is from Table 2.1. Relaxation kinetics at 90% and 50% of the peak (rt_{90} & rt_{50}) are shown in top left and right panels. Time to peak (ttp) on bottom left panel and the twitch time TT is shown on the bottom right panel.

3.2.6 Optimization of contraction parameters

The contraction parameters in RDQ2020 model were calibrated according to ventricular human data recorded at body temperature (see Table 3, Regazzoni *et al.* 2020). Hence, to adopt human atria-like physiology, a re-calibration of contraction parameters was required. The calibrated *in-silico* biomarkers were obtained using the set of *in-vitro* biomarkers extracted from the experimental data available for human atrial myocytes quantified in Table 3.1.

Table 3.1: Comparison of AP, Ca^{2+} transient and F_{active} biomarkers obtained with the model and the values (lower and upper bounds along with their mean values) from *in-vitro* human atrial data extracted from references in Table A3 and 3.3.

Action Potential			**Ca^{2+} transient**			**Active Force**		
Biomarker	**Mean value Range [LB, UB]**	**Model output**	**Biomarker**	**Mean value Range [LB, UB]**	**Model output**	**Biomarker**	**Mean value Range [LB, UB]**	**Model output**
APD_{90} (ms)	263.05 [202, 332]	248	Ca_{amp} (µM)	.268 [.180, 0.4]	0.221	F_{active} (kPa)	5.92 [3.14, 9.5]	4.7
APD_{50} (ms)	50.02 [25, 94.14]	60.2	Ca_{dias} (µM)	.223 [0.2, 0.25]	0.187	$ttp_{Factive}$ (ms)	104.98 [79.5, 161]	135.7
APD_{30} (ms)	7.725 [5, 13.9]	13.4	ttp_{Ca} (ms)	52.5 [49.4, 55.6]	93.7	$rt_{50Factive}$ (ms)	80.92 [60.2, 118.6]	140
V_{amp} (mV)	103.266 [83, 130]	111.7	rt_{50Ca} (ms)	177.5 [168.5, 186.5]	176	$rt_{90Factive}$ (ms)	200 [153, 235.9]	406
V_{diast} (mV)	-75.1 [-68, -75.1]	-75.7	TT_{Ca} (ms)	539.1 [508.1, 570.1]	690	$TT_{Factive}$ (ms)	433.3 [413.1, 453.5]	663
dV/dt_{max} (mV/ms)	179.23 [159, 231.9]	177	τ (s^{-1})	335 [220, 450]	288			

Table 3.2: Contraction module calibration based on biomarkers from human atrial experimental data.

Parameters	**Calibrated data**	**RDQ2020 calibration**
Troponin sensitivity (k_{d0}) (mM)	1.4e-3	0.3e-3
Troponin dissociation rate (k_{off}) (s^{-1})	197.6	100
Cooperativity factor (ɣ) (-)	13.43	12
r_0 (s^{-1})	55.5	134.31
α (-)	22.2	25.184
$\boldsymbol{\mu_{fp}^0}$ (s^{-1})	13.5	32.653

$\boldsymbol{\mu_{fp}^{1}}$ (s^{-1})	0.304	0.778
a_{XB} (kPa)	52.89e3	22.894e3

The major difference between atria and ventricles contraction lies in the contractile protein myosin and its iso-enzymatic variety (Reiser *et al.* 2001; Narolska *et al.* 2004; Morano *et al.* 1987). Contractile protein myosin is the major determinant of contractility since it can modulate the ATPase activity and maximum shortening velocity (v_{max}). Accordingly, the contraction and relaxation kinetics are faster in atria than ventricles (Piroddi *et al.* 2006). Moreover, the Ca^{2+} sensitivity of atrial fiber is also less than ventricles (Morano *et al.* 1987).

Table 3.3: Human atrial *In-vitro* data used for evaluation of action potential biomarkers

Reference	**Experimental protocols**	**Biomarkers**	**Frequency dependent Biomarkers**
Bosch *et al.* 1999	Whole cell voltage clamp technique was used to record AP from rod shaped cells of the RA appendages at 36°C.	APD_{90}	APD_{90}
Wagoner *et al.* 1999	Whole cell patch clamp technique was used to record AP from isolated atrial myocytes at 35°C.	APD_{90}, APD_{50}	APD_{90}, APD_{50}
Dobrev *et al.* 2003	Atrial myocytes were recorded using patch electrodes at 37 °C.	APD_{90}, APD_{50}, RMP	APD_{90}
Dawodu *et al.* 1996	RA trabeculae were simulated with intracellular microelectrode technique to record APs at 31°C. (Type 3 morphology data was considered only)	APD_{90}, APD_{50}, APD_{30}, RMP, dV/dt_{max}, APA	RMP, dV/dt_{max}
Lagrutta *et al.* 2006	Microelectrode technique was used to measure action potential duration from human atrial myocytes at 35°C.	APD_{90}, APD_{50}, RMP, dV/dt_{max}, APA	
Wang *et al.* 1990	Microelectrode technique was used to measure AP characteristics from atrial strips obtained from right atrial appendage at 36°C.	RMP, dV/dt_{max}, APA	
Wettwer *et al.* 2004	Microelectrode technique was used in right atrial trabeculae.	RMP	
Dobrev *et al.* 2001	Microelectrode technique used to measure the APs from right atrial trabeculae at 37°C.	APD_{50}, RMP	

Workman *et al.* 2003	Whole cell patch clamp technique was used to record the APs at 35-37ºC.	APA	
Ford *et al.* 2016	Sharp microelectrode was used to measure action potentials from small pieces of RAA at 36°C and basal frequency of 1Hz	APD_{90}, APD_{50}, APD_{20}, PLT_{20}, RMP, dV/dt_{max}, APA, ERP	APD_{90}, APD_{50}, APD_{20}, PLT_{20}, RMP, dV/dt_{max}, APA, ERP

Based on these observations, the contraction dynamics of regulatory unit (RU) i.e., a TRPN and a Tm unit were modified. The dynamics were based on transition rates (k_{off} and k_{basic}), the cooperativity (γ) and the Ca^{2+} sensitivity (k_d). The optimized set of parameters was obtained on basis of time related biomarkers of F_{active} i.e., relaxation time at 50% and 90% of peak values ($rt_{50Factive}$, $rt_{90Factive}$), time to F_{max} ($ttp_{Factive}$), and twitch time ($TT_{Factive}$). This optimization was carried out at the basal frequency of 1Hz and then extended for the physiological range of frequencies as shown in Figure 3.5. The human *in-vitro* data collection used for this calibration was the same as listed in Chapter 2 (Table 2.1) with the addition of biomarkers from references in Table A3. Similarly, biomarkers were also computed for the CaT like relaxation time at 50% of CaT_{max} (rt_{50CaT}), time to CaT_{max} (ttp_{CaT}), total time duration (TT_{CaT}) and compared with a small set of data from Table A3. The calibration was performed using *fminsearch* optimization function to find local minima in Matlab. The model biomarkers were tuned in accordance with the human atrial *in-vitro* data to adopt atria like physiology.

Other parameters based on cross bridge cycling (XB_{cy}) i.e., μ_{fp}^{0}, μ_{fp}^{1}, α, and r_0 were also calibrated, by following the procedure presented by (Regazzoni *et al.* 2021). This calibration was based on the difference in maximal shortening velocity (v_{max}) of XB_{cy} for human atria from ventricles (Kuijpers *et al.* 2007). Using the new v_{max} value, based on the best fit with force-velocity hyperbolic curve, we re-calibrated the XB_{cy} parameters (Table 3.2).

The model presented is based upon an ordinary set of differential equations implemented in Matlab using a stiff ordinary differential equation solver method (ode15s). Under the basal conditions, the model was simulated at 1Hz frequency and 800 beats to reach the steady state. All the modifications introduced in the model equations are shown in the Appendix. All other minor modifications in ionic current conductance values have been listed in Table A1(A).

3.2.7 CaMKII based phosphorylation of ionic currents and Ca^{2+} handling

Ca^{2+}/CMDN-dependent kinase II (CaMKII) is a multifunctional serine/threonine kinase expressed ubiquitously in the cardiomyocytes (reviewed in Bers & Grandi 2009). CaMKII plays an important role in regulating cardiac excitability and contractility. Ca^{2+} mediated modulation of ion channels through direct Ca-CMDN binding or by the activation of CaMKII. CaMKII can phosphorylate numerous targets involved in ion channels, Ca handling, and in regulatory proteins. In the literature, many studies were performed on the biochemically detailed models of CaMKII

signaling but the focus of these studies was on ventricular electrophysiology (Soltis & Saurceman 2010, Morotti *et al.* 2021). As the EC coupling differs among the atrial and ventricular cardiomyocytes (as shown in Chapter 1) because of differences in ultrastructure, Ca^{2+} homeostasis hence, it is crucial to study the atrial model integrated with CaMKII modulated targets based on atrial physiology and pathophysiology. For atrial cardiomyocytes, Zhao has developed an atrial cell model including CaMKII activation to explore the mechanism induced by atrial arrhythmia under oxidative stress (Zhao *et al.* 2020). Another model by Haibo Ni integrates electrophysiology and Ca^{2+}-handling with biochemically detailed systems model of upstream signaling pathways i.e. protein kinase A (PKA) and CaMKII in human atria (Ni *et al.* 2022).

Table 3.5: Effect of CaMKII based phosphorylation of the cellular targets of human atrial cardiomyocytes.

Target	**Effect of CaMKII-dependent phosphorylation**	**Reference**
Fast I_{Na}	Slow inactivation gate slowed by 1.46 times	Zhang *et al.* 2015
I_{CaL}	1. Current increased by 40% 2. Voltage dependent inactivation gate slowed by 1.5	Christ *et al.* 2004
I_t	1. Current reduced by 10% 2. Inactivation time slowed by 1.56 times	Tessier *et al.* 1999
I_{Kur}	Current increased by 57%	
RyR	Opening probability increased and leak current increased by 2.5 times.	Neef *et al.* 2010, Voigt *et al.* 2012
SERCA	Pumping activity increased by 27% by a direct effect and reduction in PLB inhibition, an indirect enhancement, of forward pumping rate by 70%.	Koivumaki *et al.* 2009

In human atrial cardiomyocytes, CaMKII acts on diverse targets in ion channels and Ca^{2+} handling as listed in Table 3.5. The CaMKII model was adopted from O'Hara ventricular model formulation (O'Hara *et al.* 2011), where each target *T* is divided into two parts:

$$T = (1 - \phi_{CAMK})T_{NP} + \phi_{CAMK}T_{CaMK}$$

where T_{NP} is the non-phosphorylated part of the target, T_{CaMK} is the CaMKII modulated part of the target, and the ϕ_{CAMK} is the proportion affected by CaMKII and is given as:

$$\phi_{CaMK} = \frac{1}{1 + \frac{K_{m,CaMK}}{CaMK_{active}}}$$

where $CaMK_{active}$ is the fraction of active CaMKII binding sites, $K_{m,CaMK}$ is the half saturation coefficient which was the same as O'Hara CaMKII model. $CaMKII_{active}$ is given as:

$$CaMK_{active} = CaMK_{bound} + CaMK_{trap}$$

where $CaMK_{bound}$ and $CaMK_{trap}$ are the fraction of CaMKII binding sites bound to Ca^{2+}/CMDN and with trapped CMDN respectively and are given as:

$$CaMK_{bound} = CaMK_0 \frac{1 - CaMK_{trap}}{1 + \frac{K_{mCaM}}{[Ca^{+2}]_{ss}}}$$

here $CaMK_0$ is the fraction of active CaMKII binding sites at equilibrium, K_{mCaM} is the sensitivity factor of CaMKII bound to Ca^{2+}/CMDN. Hence, $CaMK_{bound}$ quantifies the dependence on $[Ca^{2+}]_{ss}$. $CaMK_{trap}$ is a dynamic quantity and is given as:

$$\frac{dCaMK_{trap}}{dt} = \alpha_{CaMK} CaMK_{bound}\left(CaMK_{bound} + CaMK_{trap}\right) - \beta_{CaMK} CaMK_{trap}$$

α_{CaMK} and β_{CaMK} are the transition rates. All the values used for CaMKII model constants are listed in Table A1(B).

3.3 Results

3.3.1 Model characteristics: AP, Force and Ca^{2+} transient

The simulated steady state characteristics of AP waveform, Ca^{2+} transient in *ss* and *bc* compartments, and F_{active} are shown in Fig. 3.6. The modifications with respect to the parent model, KM2011, resulted in a type-3 human atria AP morphology (Fig. 3.6A) (Dawodu *et al.* 1996). Hence, a prominent plateau phase was achieved by slow inactivation of I_{CaL} current. The role of the modified formulation of I_{CaL} in producing the AP shape of MBS2022 is assessed in Fig. 3.7 where the modified I_{CaL} led to a prominent lengthening of the plateau, early and late repolarization phase of the AP (dashed line in red vs dot-dashed line in purple). The CaT produced by the model can be seen in Fig. 3.6B. As expected, the amplitude is greater in the *ss* with respect to the *bc* compartment (0.678 vs 0.22 μM), with similar diastolic levels (0.179 vs 0.187 μM). A temporal heterogeneity is also evident in the dynamics of the transient; moving to the center, CaT is slowed and delayed, as quantified by the differences in biomarkers values from *ss* to *bc*: δttp_{Ca} 61 ms, δrt_{50Ca} 100 ms and δTT_{Ca} 256 ms. The mean CaT (that is the weighted average between cytosolic compartments, to be compared with experimental measurements) was computed, its time course was substantially equal to that of Ca^{2+} transient in bulk cytosol (not shown). The Ca^{2+} handling behavior for MBS2022 can be analysed using $[Ca^{2+}]_{SR}$ traces from *ss* and *bc* compartments in Fig. 3.6D. In the *ss* compartment, a prominently large Ca^{2+} release can be seen from the SR into the *ss* compartment, with fast release flux dynamics (Fig. 3.9D vs H in red solid line). Whereas, in the bulk cytosol, the Ca^{2+} release is smaller (Fig. 3.9G in red solid line), slower, and slightly delayed, resulting in more Ca^{2+} SR load. The force developed (F_{active}) in the bulk cytosol because of EM coupling is shown in Fig. 3.6E.

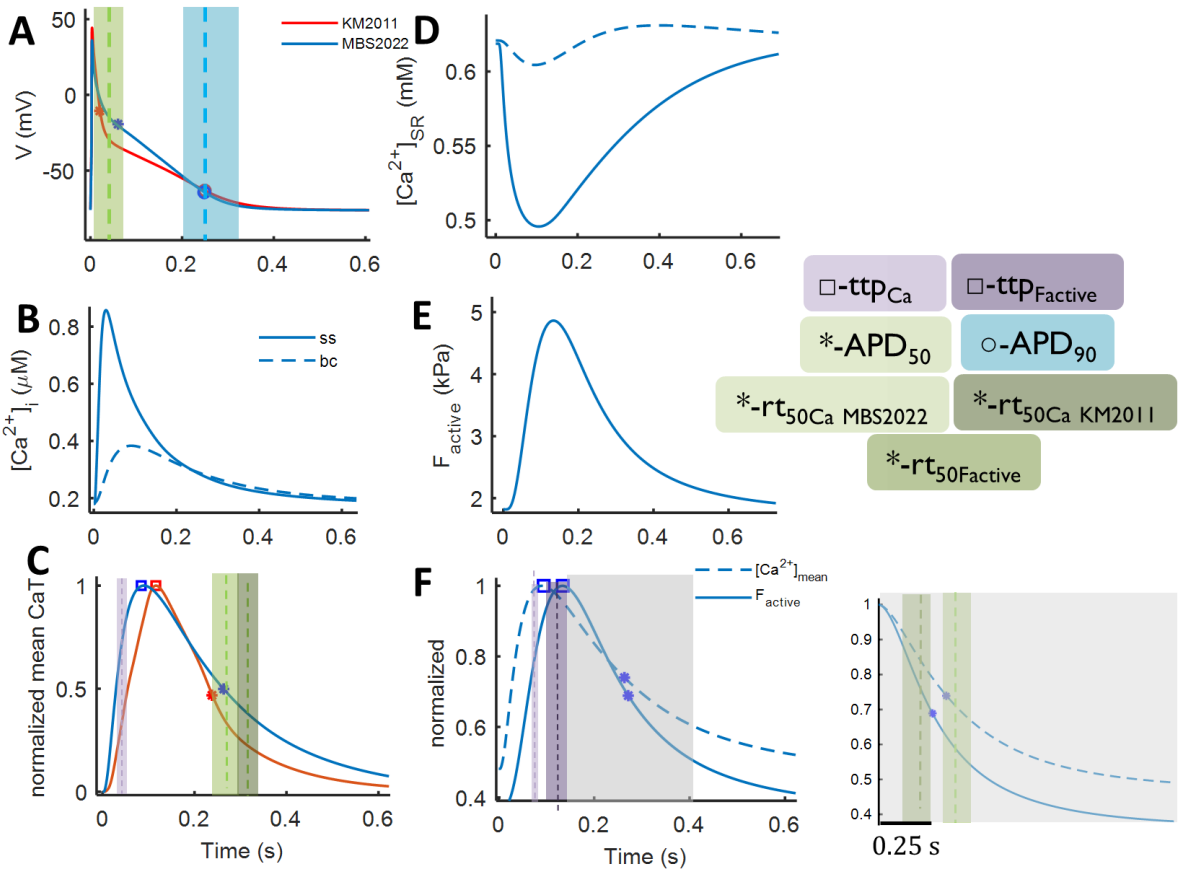

Figure 3.6: AP, Ca-Handling and F_{active} characteristics obtained with the MBS2022 model compared to those obtained with the KM2011 model and experimental human atrial data. Few selected biomarkers are also plotted using various marker labels like ttp_{Ca} or $ttp_{Factive}$ with open squares, APD_{50} or rt_{50Ca} or $rt_{50Factive}$ with asterisk, and APD_{90} with open circles. The color for each shaded area corresponds to data range of a biomarker as was also reported in Table 3.1. A) Comparison of AP traces for MBS2022 (in blue) with KM2011 (in red) and with experimental APD_{50} and APD_{90}, B) Ca^{2+} transients for subspace (solid) and bulk cytosol (dashed line), C) comparison of normalized mean (i.e., weighted average between cytosolic compartments) Ca^{2+} transient from MSB2022 (in blue) and KM2011 (in red) and with experimental ttp_{Ca} and rt_{50Ca}, D) Ca^{2+} concentration inside the SR for both ss and bc subcompartments, E) F_{active} produced by the EM coupling in MBS2022 model, F) comparison of normalized mean Ca^{2+} transient and F_{active} time course in the MBS2022 model (inset: alignment of the same curve with respect to their peaks, to compare relaxation dynamics).

A quantitative comparison of AP, CaT and F_{active} biomarkers with *in-vitro* human atrial data ranges is presented in Figure 3.6 and Table 3.1. The model output biomarkers were plotted using marker labels, whereas within the biomarker legend (Figure 3.6 on the right), each color corresponds to its *in-vitro* value range and the dashed lines are for mean values also reported in Table 3.1. Most of the biomarkers are within the range of the experimental ones. In particular, the MBS2022 model AP curve (in blue) is compared with KM2011 (in red) along with their APD_{50} and APD_{90} biomarkers in Figure 3.6A. Our AP model has a more dominant plateau than KM2011 and is more in agreement with the mean APD_{50} reported by the *in-vitro* data range. For late repolarization, APD_{90} seems comparable for both models and lies on the mean value of the data. CaT upstroke is faster compared to its parent model (Figure 3.6C), while its decrease is slower (within the experimental range, Figure 3.6C). The dynamics of F_{active} (solid line) has been compared with mean CaT (dashed line) of the model along with their ttp and rt_{50} biomarkers

(Figure 3.6F). The CaT arises earlier and decays more slowly than F_{active} as also shown by the data ranges light and dark shades respectively. The rising part of CaT and F_{active} curves are compared using ttp, with ttp_{Ca} less than $ttp_{Factive}$. The ttp_{Ca} is slightly longer than the data range but $ttp_{Factive}$ is within the lower data bound. The comparison of relaxation phase was carried out in the inset where both curve peaks were aligned to highlight that rt_{50Ca} is longer than $rt_{50Factive}$. Moreover, $rt_{50Factive}$ lies quite close to the lower bound of the data range.

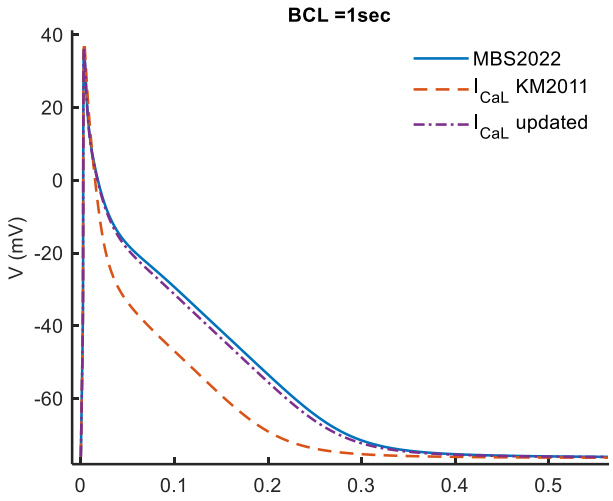

Figure 3.7: Role of membrane currents I_{CaL}, Ito in producing action potential for MBS2022 model at 1 Hz frequency. Steady-state action potentials resulting from updating each current at a time i.e., by I_{CaL} current formulation (in dashed line).

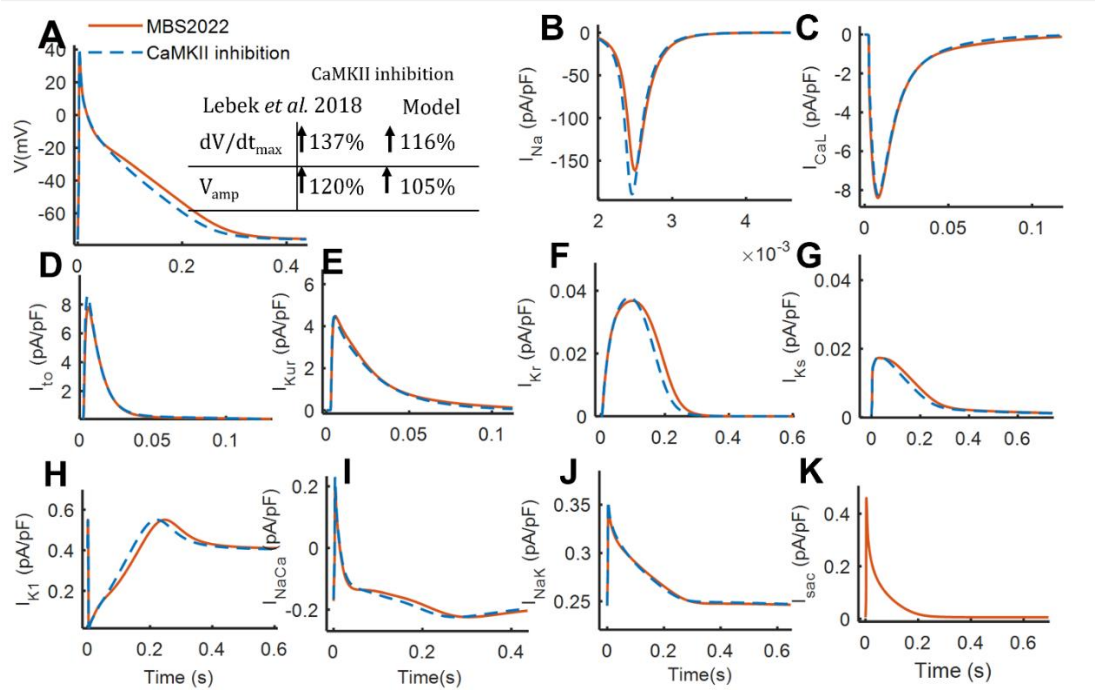

Figure 3.8: Steady-state human atrial AP, major membrane currents at 1 Hz basal frequency in comparison with CaMKII inhibition (dashed line) in MBS2022 (solid line). A) shows the AP morphology for MBS2022, B & C) the fast I_{Na} and the I_{CaL} current, D &

E) shows the phase 1 repolarizing currents I_{to} and I_{Kur}, F, G & H) shows I_K currents for phase 2 repolarization i.e., I_{Kr}, I_{Ks} and I_{K1}, I & J) represents the exchanger I_{NaCa} and the pump currents I_{NaK}, and K) shows the stretch activated current I_{sac}.

All the major currents for MBS2022 model at the basal frequency of 1 Hz are shown in Figure 3.8. The CaMKII inhibition is also compared with the basal condition of the model where where shortening of mid repolarization phase is observed as shown in Figure 3.8. The fraction of $CaMKII_{active}$ is 2.4% at basal rate and it got enhanced with increasing rate as will be described later in this section. Two of the AP biomarkers i.e. dV/dt_{max} and V_{amp} are compared with the experimental data (Leberk et al. 2018) where a qualitative eqvivalence can be observed. Among the ionic currents, I_{Na} shows a increase (Fig. 3.8 panel B), and the I_K current shows slightly fast inactivation (Fig. 3.8 panel F & G). The Ca^{2+}-transient and all the incoming and outgoing flux are shown in Fig. 3.9 (in red solid line) along with the effect of CaMKII inhibition (in blue dashed line). The CaT in *ss* (Fig. 3.9 panel A) rises instantly and decay is also fast in comparison to CaT in *bc* (Fig. 3.9 panel E). This is evident with fast release and uptake flux dynamics of the *ss* compartment (Fig. 3.9 panel D & C). The CaT propagates towards the *bc* compartment via diffusion (J_{diff}) (Fig. 3.9 panel B). In *bc* compartment, the release flux is quite small whereas the uptake is very large in magnitude (Fig. 3.9 panel H & G) in comparison to *ss*. CaMKII inhibition has reduced the J_{up} flux and has reduced F_{active} (Fig. 3.9 panel F) as was observed by Lebek et al. (Lebek *et al.* 2018).

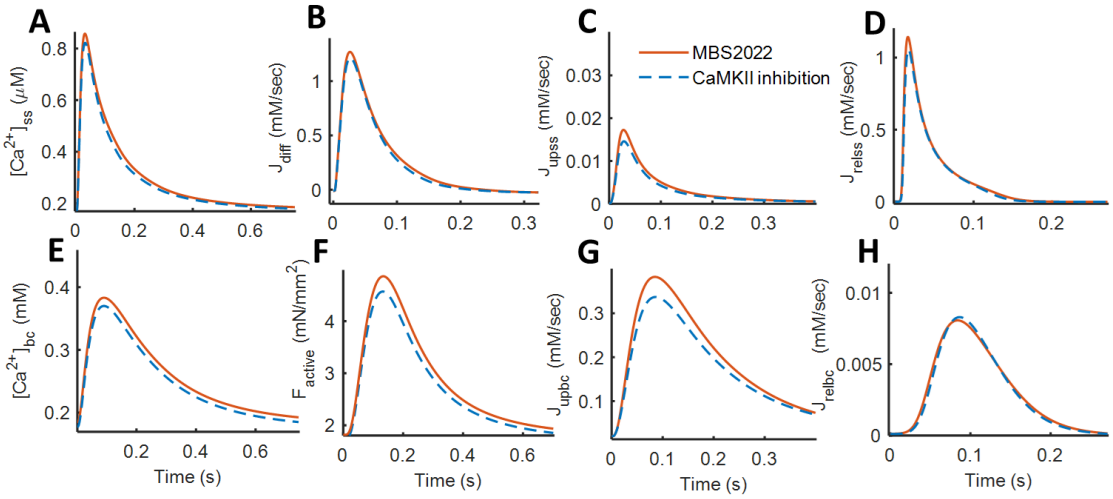

Figure 3.9: Ca^{2+}-handling in MBS2022 model (in red solid line) in comparison with CaMKII inhibition (blue dashed line). A) Ca^{2+}-transient in the ss compartment, B) diffusion from ss to bc (J_{diff}), C) uptake flux via SERCA pump (J_{upss}), D) release flux (J_{relss}), E) slow and smaller Ca^{2+}-transient in the bc, F) Factive produced, G) uptake flux (J_{upbc}), and H) small release flux (J_{relbc}).

3.3.2 Mechano-Calcium Feedback Effect

The EM coupling characteristics of the model were analyzed by keeping SL (i.e. l_{CE}) fixed, in an iso-sarcometric condition as is usually found *in-vitro* experiments (referred to Table 3.1). The consequence of coupling on AP, CaT and F_{active} for the novel MBS2022 model was analysed by comparing the model output under basal conditions, i.e. bidirectional coupling (solid line), with no MCF condition (dashed lines), i.e. by removing the dynamic effect of Ca^{2+} bound to troponin from the model. The MBS2022 AP waveform is compared with AP under no MCF condition in Figure 3.10A. The AP curve and its kinetics are only slightly affected by MCF, the biomarkers are

showing no change and are within the experimental range, while a very slight shortening of early repolarization phase is observed. Accordingly, I_{CaL} current (Figure 3.10B) trace shows more inactivation during the plateau of the curve under no MCF condition. Similarly, CaT produced by the model in bulk cytosol is compared under no MCF effect in Figure 3.10D. An enhanced systolic level of CaT is observed under no MCF condition because the elevated amount of Ca^{2+} bound to TRPN (Figure 3.10F) is not sequestered from the cytoplasm. Moreover, the CaT peak arrives earlier, and the decay is faster than the model output with MCF in place. The ttp_{Ca} for CaT was a bit longer for our model but under no MCF condition, it was near the lower data bound. Moreover, the rt_{50Ca} for the model was within the data range but it went completely out of range under no MCF condition. Although the model produces a TT_{Ca} that is slightly delayed than the data range, under no MCF the TT_{Ca} is far too short, with a large difference from the data range. Because of raised Ca^{2+} level in the bulk cytosol, the exchanger I_{NaCa} first shows more inward current followed by a reduction in the latter phase of time under no MCF condition as shown in Figure 3.10C. On the same lines, F_{active} curve with fast relaxation dynamics was also observed under no MCF condition as shown in Figure 3.10E. The biomarker $rt_{50Factive}$ showed the model output was quite close to the data range but under no MCF condition the biomarker went within the lower bound of the data range.

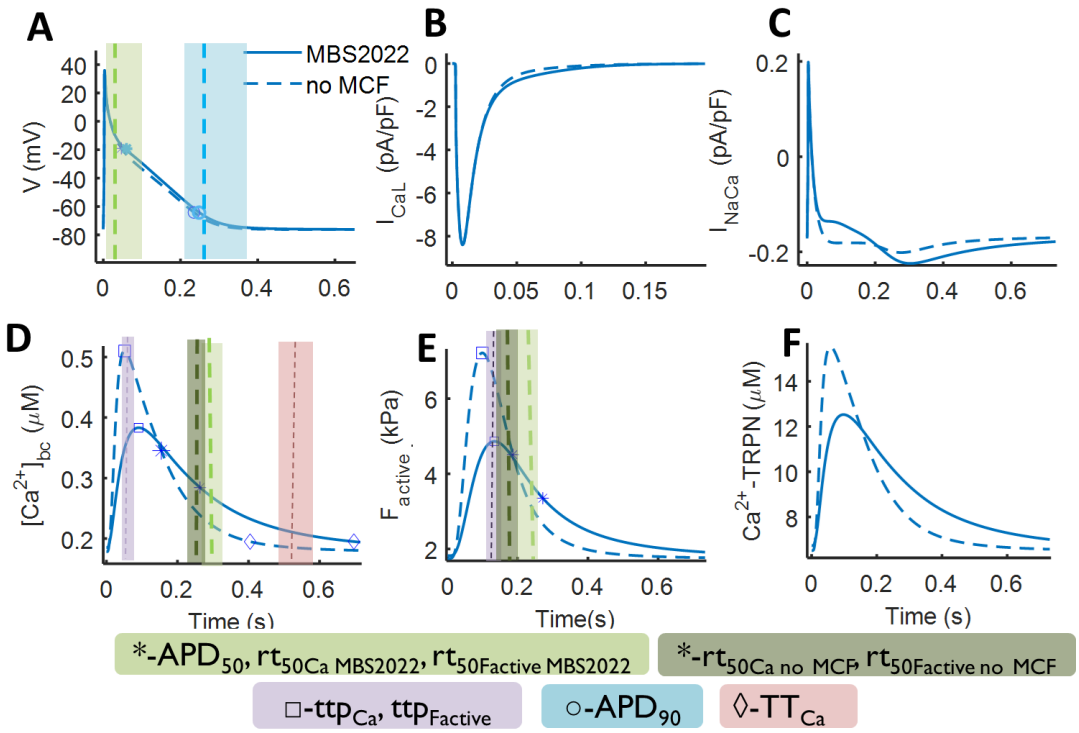

Figure 3.10: Effect of mechano-calcium feedback on MBS2022. Few biomarkers were also plotted by using markers defined in the figure legend in the bottom like ttp_{Ca} or $ttp_{Factive}$ with open squares, APD_{50} or rt_{50Ca} or $rt_{50Factive}$ with asterisks, APD_{90} with open circle and TT_{Ca} with diamond. The colored ranges correspond to the experimental data bounds and their means values (in dashed lines) obtained from Table 1. Consequences of coupling on (A) MBS2022 AP (solid line) in comparison to no MCF (dashed line) condition with experimental APD_{90} and APD_{50}, (B & C) ionic currents I_{CaL} and I_{NaCa} plots with respect to no MCF condition, (D) Ca^{2+} transient in bulk cytosol with respect to no MCF condition, (E) comparison of F_{active} time course with no MCF condition and (F) concentration of Ca^{2+} bound to TRPN with and without MCF.

3.3.4 Quantifying Ca-SR contents

SR Ca^{2+} content is a major modulator of Ca^{2+}-transient hence we made a simulation test equivalent to caffeine induced effect to quantify the SERCA activity by measuring SR-Ca^{2+} contents and its pumping rate. In experiments, the atrial myocytes are preconditioned with an I_{CaL} activation voltage clamp protocol for 1min. Caffeine (10mM) causes a large rise in CaT as a result of SR Ca^{2+} release. The slow decay of CaT is mainly through the I_{NaCa} exchanger, , and the integral of the current is a measure of SR Ca^{2+} contents.

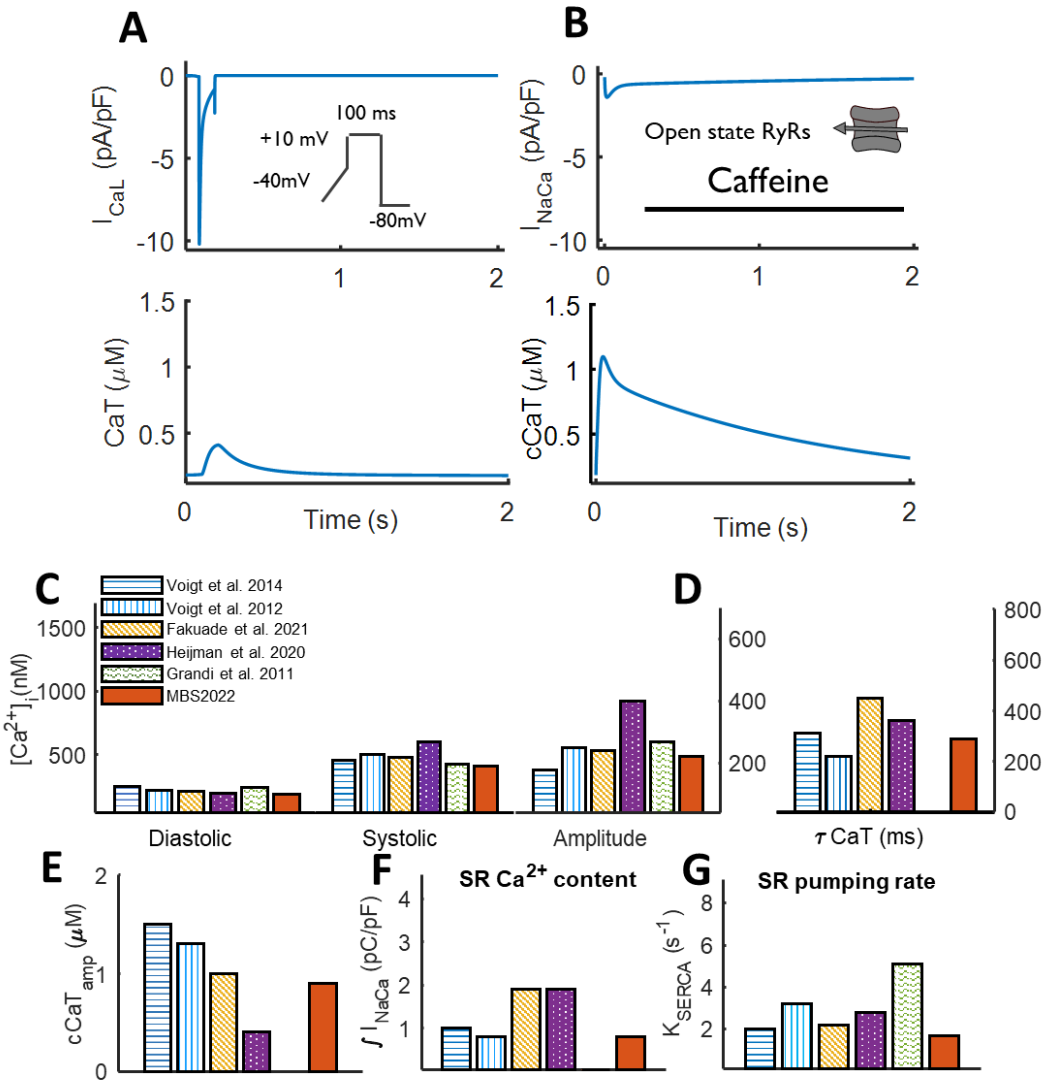

Figure 3.11: Validation of SR Ca^{2+} content and pumping rate in the MBS2022 model. A) The voltage clamp protocol (inset) resulting ICaL current (top) and ICaL triggered Ca2+ transient (CaT) (bottom). B) The caffeine induced inward I_{NaCa} current (top) with CaT (cCaT) (bottom). The experimental data shown in from of bar plots extracted from Voigt et al. 2014 (in blue horizontal lines), Voigt et al. 2012 (in blue vertical lines), Fakuade et al. 2021 (in yellow diagonal lines), Heijman et al. 2020 (in purple dots), Grandi et al. 2011 (in green curvy lines), and MBS2022 output (in red solid bars). C) shows the characteristics of I_{CaL} triggered CaT diastolic (on left), systolic (middle), and amplitude (on right) and D) the decay time constant for the CaT. The caffeine induced CaT amplitude (E), SR- Ca^{2+} content is the integral of I_{NaCa} current under caffeine application and the k_{SERCA} is the measure of SERCA pump rate and is compared for the simulated output with the experimental data in panel (F), and (G) respectively.

Following the experiment, Ca^{2+} current and transient were simulated for a voltage clamp protocol at 0.5Hz as shown in Figure 3.11A (inset). The protocol proceeds with a 100ms duration ramp to -40mV to inactivate fast I_{Na} current from the holding potential of -80mV followed by a step pulse to +10mV for 100ms times (Grandi *et al.* 2011, Voigt *et al.* 2014). Simultaneous I_{CaL} current (top) and Ca^{2+}-transient traces (bottom) are shown in Figure 3.11A. The resultant CaT_{bc} decay phase was fit on a mono-exponential equation given as (Voigt *et al.* 2014 Supplementary Information),

$$CaT(t) = CaT_{amp} * \exp(-k_{sys} * t) + CaT_{dias} \quad (3)$$

The voltage clamp protocol yielded CaT_{sys}=0.41uM and Ca_{diast}=0.179uM and we obtained decay rate, k_{sys}=3.47s^{-1} for the best fit on the I_{CaL} triggered CaT. and decay time constant of 288ms (Fig. 3.11D), corresponding to a decay rate ksys=3.47s-1. In comparison to the experimental data as shown in Fig. 3.11C, the CaT amplitude is quite inline with Fakuade et al. (Fakuade et al. 2021) and Voigt et al. (Voigt et al. 2012, 2014) data whereas, slightly smaller than the value reported by Heijman at al. (Heijman et al. 2020). The decay rate for CaT (Fig. 3.11D) is in between the reported data i.e. less than Fakuade et al. and Heijman et al. but greater than Voigt et al. data range

The caffeine induced Ca^{2+}-transient (cCaT) experiment was replicated by switching the membrane voltage to holding potential (-80mV) and running the simulation in RyRs open state i.e. both activation, inactivation gates along with the Ca^{2+}SR dependent activation gate were set to 1 to have maximum release flux in the cytosol. The cCaT is shown in Figure 3.11B (bottom panel in solid line) where the cCaT has a slow decay phase with high amplitude (2.6 times greater than CaT). The resulting large current flowing through the exchanger I_{NaCa} is shown in Figure 3.11C (solid line). The integral of I_{NaCa} current is the measure of SR-Ca^{2+} content as shown in Fig. 3.11F. The model has SR Ca^{2+} load equivalent to Voigt et al. data but is smaller than Heijman and Fakuade et al. data bar plots. The SERCA pumping rate (k_{SERCA}) is estimated as:

$$k_{SERCA} = k_{sys} - k_{caff}$$

here k_{caff} is given as,

$$k_{caff} = k_{NaCa} + k_{PCa}$$

here k_{PCa} is a small contribution of sarcolemma Ca^{+} current. Hence, using Equation (3) with $cCaT_{amp}$=0.9uM, and $cCaT_{dias}$=0.163uM we obtained k_{caff} =1.8 s^{-1} yielding k_{SERCA} =1.9 s^{-1} (Fig. 3.11G). Thus, the comparison shows that the model has SR Ca^{2+} content in between the experimental data ranges whereas the SERCA pumping time is slower than most of the experimental values (Fig. 7F) but not so far from Voigt et al. and Fakuade et al..

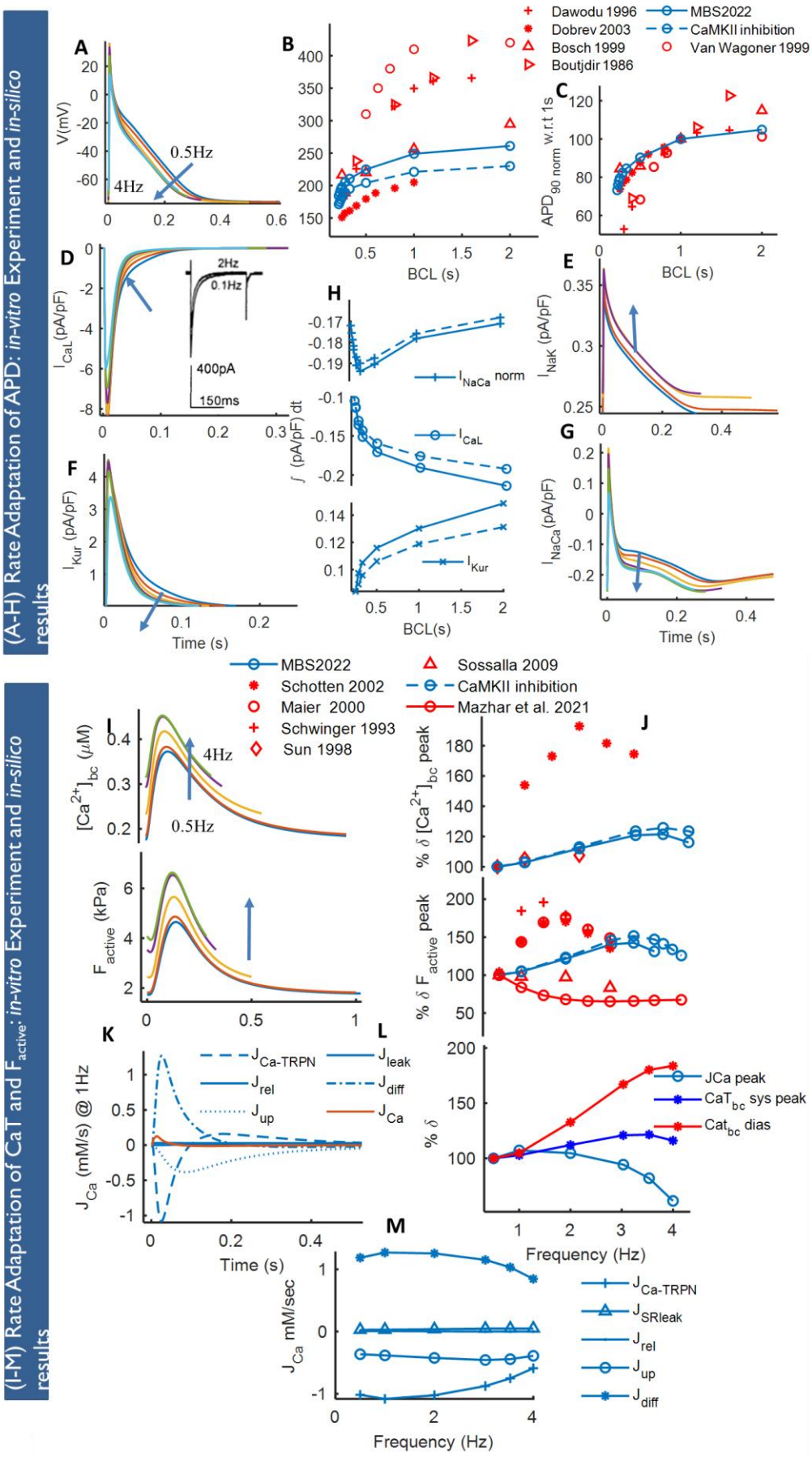
(A-H) Rate Adaptation of APD: *in-vitro* Experiment and *in-silico* results
(I-M) Rate Adaptation of CaT and F_{active}: *in-vitro* Experiment and *in-silico* results
Dawodu 1996
Dobrev 2003
Bosch 1999
Boutjdir 1986
MBS2022
CaMKII inhibition
Van Wagoner 1999
A
V(mV)
0.5Hz
4Hz
B
BCL (s)
C
$APD_{90\ norm}$ w.r.t 1s
D
I_{CaL} (pA/pF)
2Hz
0.1Hz
400pA
150ms
E
I_{NaK} (pA/pF)
F
I_{Kur} (pA/pF)
Time (s)
H
I_{NaCa} norm
I_{CaL}
$\int$ (pA/pF) dt
I_{Kur}
BCL(s)
G
I_{NaCa} (pA/pF)
Time (s)
MBS2022
Schotten 2002
Maier 2000
Schwinger 1993
Sun 1998
Sossalla 2009
CaMKII inhibition
Mazhar et al. 2021
I
$[Ca^{2+}]_{bc}$ (μM)
4Hz
0.5Hz
F_{active} (kPa)
J
% δ $[Ca^{2+}]_{bc}$ peak
% δ F_{active} peak
K
J_{Ca} (mM/s) @ 1Hz
$J_{Ca-TRPN}$
J_{leak}
J_{rel}
J_{diff}
J_{up}
J_{Ca}
Time (s)
L
% δ
JCa peak
CaT_{bc} sys peak
Cat_{bc} dias
Frequency (Hz)
M
J_{Ca} mM/sec
$J_{Ca-TRPN}$
J_{SRleak}
J_{rel}
J_{up}
J_{diff}
Frequency (Hz)

Figure 3.12: Rate adaptation response of MBS2022 and its dependence on CaMKII activity. A-H) shows rate dependence of AP and the cellular mechanism behind it. (A) *in-silico* results of AP time course for each rate, B) shows APD_{90} shortening trend for the model with BCL in comparison to experimental data listed in Table 3.3 and CaMKII inhibition (in dashed line), C) APD90 rate dependence normalized with respect to BCL=1sec, D) I_{CaL} rate dependence compared in experiments (Li *et al.* 1997) (inset) with *in-silico* results. The mechanism of APD_{90} shortening (D-H). E) shows I_{NaK} traces F) shows rate dependency of I_{Kur} current G) shows increasing inward I_{NaCa} current traces, H) rate dependent trend of integral of I_{NaCa} (top) normalized with respect to the BCL, I_{CaL} (middle) and I_{Kur} (bottom) is shown. I-M) shows rate dependence of F_{active} and CaT and its cellular mechanism. *In-silico* results of CaT and F_{active} rate dependence in I), J) percentage change of CaT peak (top) and F_{active} peak values produced by the model in comparison to experimental data (references in Table 3.1) and CaMKII inhibition effect (in dashed lines). The mechanism of CaT rate dependence is shown in (K-M). K) shows the comparison of magnitude and dynamics of inward fluxes to *bc*, diffusion from *ss* to *bc* compartment (J_{diff}) (dot-dashed line), the SR release (J_{rel}) and leak (J_{SRleak}); and outward fluxes, SR uptake (J_{up}) (dotted line), $J_{Ca\text{-}TRPN}$ (dashed line) at 1Hz frequency. The sum of all fluxes is J_{Ca} in red. L) Rate dependence trend of CaT systolic (asterisks), diastolic (cross) and J_{Ca} (open circles). M) Rate dependency of peak values of each flux using various markers, J_{diff} (asterisk), J_{up} (open circles), $J_{Ca\text{-}TRPN}$ (plus), J_{SRleak} (triangles), J_{rel} (dotted).

3.3.5 Rate adaptation for APD, force and Ca^{2+}-transient

An increase in pacing rate causes a physiological shortening of APD of atrial myocytes as quantified in various experimental studies (referred in Table 3.3). The model was capable of reproducing APD rate dependence qualitatively, whereas a quantitative comparison is difficult given the sparse set of experimental data. We simulated the rate dependent behavior of our model by running the model for a physiological range of BCLs (2, 1, 0.5 and 0.33 sec). AP curves rate dependence is shown in Figure 3.12A. In addition, APD_{90} shortening trend with BCL for a sparse set of *in-vitro* data is shown in Figure 3.12B. The relative change of APD_{90} for BCLs [2,0.3] is -20% for MBS2022 model which gets increased to -28.8% under CaMKII inhibition (dashed line). Hence, the monotonically increasing activity of $CaMKII_{active}$ for the physiological range of frequency (0.5 to 3Hz) plays its part in steep APD_{90} rate dependent shortening. The mechanism behind the APD_{90} shortening with rate is explained with the help of the ionic currents that shows substantial frequency dependence as shown in Figure 3.12(D-H): the inactivation of I_{CaL} reduces the plateau of the current (Figure 3.12D) and has a time-dependent recovery property that results in significant rate dependence and hence contributes to APD_{90} shortening which is pronounced only for higher BCLs (2 to 0.5 sec) (Li *et al.* 1997). A parallel phenomenon of rate dependent Na^+ accumulation in the cytosol occurs in ventricular CMs (Verdonck *et al.* 2004; Harrison *et al.* 1995) and in atrial guinea pig (Wang *et al.* 1993). The model shows a similar Na^+ accumulation that is shown by the enhanced pumping activity of Na^+/K^+ pump with rate. This increased pumping results in an increased outward current I_{NaK} (Figure 3.12E) that links to APD_{90} shortening. Since I_{Kur} can contribute to the positive inotropic effect therefore, the rate dependent trend of I_{Kur} integral is also analyzed in Figure 3.12H (lower panel) that showed a rate dependent reduction mainly because of the later decay phase of the current (Figure 3.12F). Thus, reducing outward I_{Kur} is contributing to the accumulation of Ca^{2+} in the cytosol (Figure 3.12J). During the fast pacing, a combination of both Na^+ and Ca^{2+} accumulation together in the cytosol contributes to I_{NaCa} exchanger to work more in reverse mode. In the model output, this is shown by the trend of integral of I_{NaCa} normalized with respect to the BCL with rate (Figure 3.12H top) where the integral is decreasing or becoming more positive after 330ms BCL (Figure 3.12G). CaMKII inhibition effect on the integral of currents (Figure 3.12H in dashed lines) indicates that CaMKII has increased the I_{CaL} and I_{Kur} currents for higher BCLs. For I_{NaCa} integral, CaMKII inhibition has reduced the current overall whereas, the outward mode working of the exchanger gets more prominent at

higher rates. Hence, a combined increase in outward I_{NaK}, I_{NaCa} and reduction in inward I_{CaL} currents is the major contributor of APD_{90} shortening for the physiological range of BCLs.

The rate dependent behavior of CaT in bulk cytosol and F_{active} for the model is shown in Figure 3.12(I-M). The positive inotropic effect with parallel rise in CaT with rate is observed in the *in-silico* model as shown in Figure 3.12I. Likewise, CaT time course shows a rise in both systolic and diastolic levels. The biphasic percentage change of CaT peak in *bc* compartment is compared with a limited available data (Figure 3.12J). On the same lines, percentage change of F_{active} is compared with human experimental data (references in Table 3.1) in Figure 3.12J (bottom panel). The cellular mechanism behind the rate dependence of CaT is explained in Figure 3.12(K-M). Following this, all the inward and outward fluxes in the *bc* compartment are compared (Figure 3.12K) under steady-state conditions and 1Hz frequency. Hence, a difference in dynamics and amplitude of the inward fluxes i.e., diffusion from *ss* to *bc* (J_{diff}), SR release in the *bc* (J_{rel}) and the SR leak (J_{SRleak}); and outward fluxes i.e., SR uptake (J_{up}) from the bulk, Ca^{2+} bound to TRPN ($J_{Ca-TRPN}$) can be observed. J_{diff} shows a large peak comparable with $J_{Ca-TRPN}$ and followed by J_{up} whereas, minimum contribution is observed by J_{rel} and J_{SRleak}. In addition, flux $J_{Ca-TRPN}$ is the fastest followed by J_{diff} and J_{up}. The sum of all the fluxes is shown by J_{Ca} (in red) in Figure 3.12K. J_{Ca} has fast dynamics and a depressed systolic level. The rate dependence of CaT systolic and diastolic values can be appreciated in Figure 3.12I and is quantified, in percentage terms, in Figure 3.12L. The progressive increase in diastolic $[Ca^{2+}]_{bc}$ is the main determinant for a consequent increase in the systolic $[Ca^{2+}]_{bc}$; however, a concurrent progressive decrease with rate of the net Ca^{2+} influx into the bulk cytoplasm, J_{Ca} (peak values) takes place, resulting in the overall biphasic rate dependence of the CaT systolic peaks. A further investigation behind this decreasing rate dependence of J_{Ca} is carried out by plotting the peak values of each flux with frequency as shown in Figure 3.12M. The J_{diff} peak (asterisk) increases slightly at lower rates (up to 1 Hz) and then reduces progressively. On the other hand, the outward flux, J_{up} (open circle) shows a slight increase with rate till 4Hz then a minute decrease whereas, a prominent decrease in $J_{Ca-TPRN}$ (plus) is observed with rate. Hence, the declining trend of diffusion with a parallel reduced amount of Ca bound to TRPN at higher rate (after 3.5Hz) gives arise to the biphasic decline of CaT in the bulk cytosol.

3.4 Discussion and Conclusions

We have developed a novel mathematical model that is electro-mechanically coupled and integrates the mechano-electric regulation with feedback pathways via MCF and MEF. The model couples AP module, the modified KM2011 (Koivumäki *et al.* 2011), with a contractility module, RDQ2020 (Regazzoni *et al.* 2020). The AP module is a simplified version of its parent model; however it was still able to preserve the characteristics of centripetal Ca^{2+} diffusion. Furthermore, this simplification made the AP module computationally efficient being defined considering 30 state variables in comparison to 43 variables of the parent model.

AP and CaT characteristics of the model and the *in-vitro* data

The modifications introduced into the KM2011 model resulted in a type-3 AP morphology of human atria that has a more prominent plateau phase than the parent model. In other words, we

achieved an APD_{50} that is more in agreement with the mean human *in-vitro* data; nevertheless, a high level of AP shape heterogeneity has been reported in human atria (Colman *et al.* 2013, Feng *et al.* 1998) and so was in our data collection in Table 3.1. Of note, the APD_{50} obtained from the model is in close agreement with the value for type-3 AP morphology reported by Dawodu (Dawodu *et al.* 1996). Likewise, the model was able to reproduce faster systolic Ca^{2+} rise and longer Ca^{2+} decay (in the *bc* compartment) than those of the contraction force, hence having a longer time course than the twitch time, in agreement to the observation made by Brixius (Brixius *et al.* 1997). Moreover, a quantitative analysis of this phenomenon based on the biomarkers ttp and rt_{50} for F_{active} and CaT_{bc} resulted in agreement with the experimental data range (Table 3.1). In particular, the CaT produced by the model has slower dynamics than the parent model (Figure 3.9C). On dissecting the decay phases, the model produced a CaT characterized by an early decay phase (rt_{50Ca}) within physiological data range (Table 3.1 & Figure 3.9) but by a slower later phase (TT_{Ca} in Table 3.1). The slow dynamics of decay in the later phase usually depends more on the kinetics of Ca^{2+} removal from the cytosol than the buffering effect (Smith *et al.* 2019). In our model, efflux of Ca^{2+} from the *bc* compartment is carried out by SR Ca^{2+} uptake since the exchanger and sarcolemmal pump are localized in the *ss* compartment. The uptake flux (J_{up}) dynamics in *bc* compartment was quite slow and small in magnitude (Figure 3.8G). This was also evident by comparing SR pumping rate (K_{SERCA}) with experimental data as was shown in Figure 3.11G. This demonstrates a room for further investigation of Ca^{2+} efflux mechanism in the bulk compartment of the developed model.

Rate dependent modulation of MBS2022 and comparison with *in-silico* studies

Computational modelling and simulation are powerful tools to accelerate the mechanistic understanding of ionic mechanisms and eventually for the whole heart. For human atrial myocytes, the CRN (Courtemanche *et al.* 1998) and the Nygren (Nygren *et al.* 1998) were the pioneer *in-silico* models with a detailed description of ionic membrane currents and with different descriptions of CaT dynamics, as reviewed by Cherry (Cherry *et al.* 2008). However, both models were not able to reproduce slow Ca^{2+}-wave like diffusion towards the center of the cell and experimental phenomena like a correct rate dependence of CaT, as shown by using the CRN model in our previous work (Mazhar *et al.* 2021). Later, KM2011 was proposed as the model with detailed Ca^{2+}-wave "fire-diffuse-uptake-fire" mechanism. However, the model showed quite different results for Ca^{2+} rate dependence when compared with the dome shaped experimental trend. An explanation can be that the Ca^{2+} homeostasis validity of the model was confined to the basal frequency of 1 Hz only. Among the existing human atrial computational model, Grandi 2011 (Grandi *et al.* 2011) was the one that demonstrated a positive CaT rate dependency (Fig. A8 in blue dot-dashed line) however, the rate dependence trend for APD_{90} was compromised at lower BCL (also reviewed in Dössel *et al.* 2012). In contrast, MBS2022 adapted the Ca^{2+} handling formulations from KM2011 and calibrated it for a set of physiological range of frequencies i.e., 0.5 to 3Hz. Moreover, the MCF effect inclusion resulted in a more physiological shape of CaT and therefore of the F_{active} dynamics as quantified by ttp and rt_{50} biomarkers. The role of MCF on rate adaptation of CaT will be analyzed in Chapter 5.

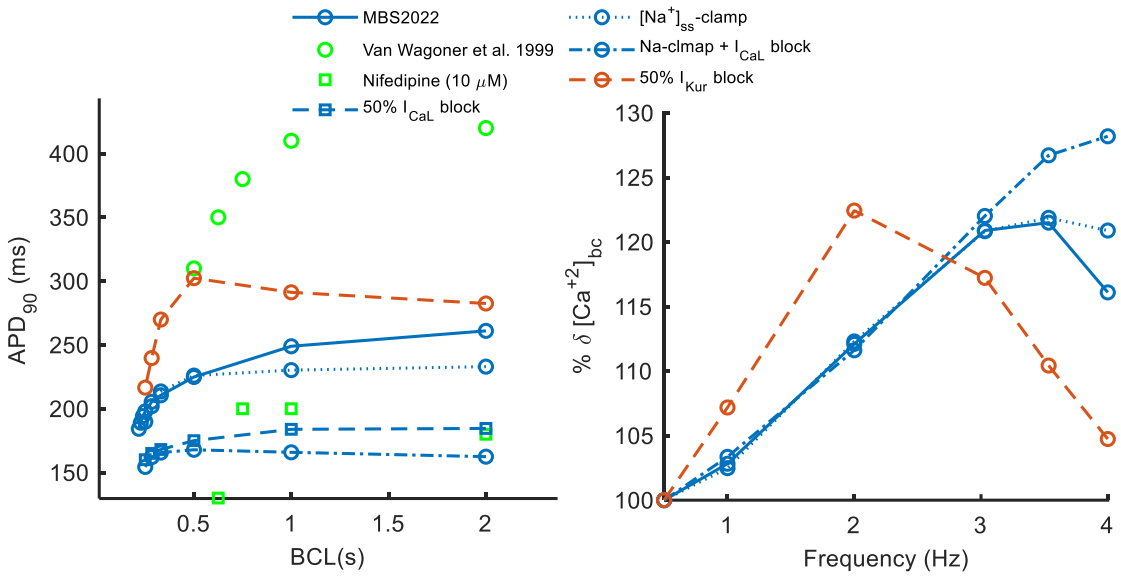

Figure 3.13: Effect of blocking each mechanism involved in APD (left) and percentage change of CaT_{bc} (right) rate dependency. MBS2022 original rate dependence (solid line) is compared with I_{CaL} block by 50% (in squares dashed line), $[Na^+]_{ss}$-clamp (dotted line), combination of I_{CaL} block and $[Na^+]_{ss}$ clamp (dashed sot line), and I_{Kur} 50% block (in red dashed line). The experimental data (Van Wagoner *et al.* 1999) (in green markers) depicts the APD_{90} rate dependency (open circles) and its response on applying calcium channel blocker Nifedipine (10μM) (open squares).

Our model reproduces the APD_{90} rate dependence as observed in type-3 AP morphology (Figure 3.9A). In line with experimental findings (Dawodu *et al.* 1996), our model shows a steep APD_{90} rate dependence, and the slope is getting steeper with increasing rates. We analyzed the ionic rate dependent mechanisms underlying APD rate dependency. We observed that the rate dependence of I_{CaL} inactivation results in a decreasing current with BCL as shown in Figure 3.12D. The effect of rate dependent reduction in I_{CaL} current on APD_{90} was quantified by blocking the current by 50% as shown in Figure 3.13 (dashed line on left). Block of I_{CaL} results in a flat APD_{90} rate dependency for BCL [2,1] similar to what was observed by Wagoner et al. by the application of 10μM nifedipine (Van Wagoner *et al.* 1999) as shown in Figure 3.13 (left in green markers). This was further confirmed by the observation made by Li et al. on human atrial myocytes where the reduction of I_{CaL} was dominant for higher BCLs (0.5 to 2sec) (Li *et al.* 1997). Another test was to clamp $[Na^+]_{ss}$ to its steady state value and quantify the impact on rate adaptation of APD_{90} and CaT_{bc} as shown in Figure 3.13 (dotted line). $[Na^+]_{ss}$ clamp resulted in a similar way as I_{CaL} block but its effect was dominant from BCL 2 to 0.5sec. Hence, a combination of 50% I_{CaL} block and $[Na^+]_{ss}$-clamp (dot-dashed line) was simulated; such combination reversed the shortening of APD_{90} for BCL 2 to 0.33sec into lengthening. Since I_{Kur} was showing rate dependency for the physiological range (Figure 3.12F) therefore, we made a test by blocking 50% of the current (dashed line in red). The block of I_{Kur} can enhance the plateau of the AP hence, resulting in more activation of I_{CaL} current. Hence, the I_{Kur} block also reversed the rate dependent shortening of APD_{90} into lengthening. This was also observed in I_{Kur} block experiments via Acatein (10 μM) (Li *et al.* 2008) and will be discussed in detail in Chapter 6. The I_{Kur} block has a similar response as 50% block I_{CaL}+$[Na^+]_{ss}$-clamp experiment but the later has reduced the overall rate dependence property of APD_{90} whereas the former enhanced it considerably. The combined 50% block

I_{CaL}+$[Na^+]_{ss}$-clamp simulation test, makes the integral of I_{CaL}, I_{Kur} currents completely flat for BCL 2 to 0.33sec as shown in Figure 3.14 (in dot-dashed line). The integral of I_{NaCa} current normalized with respect to the BCL, shows a slight change in operating mode i.e. from inward to outward at higher rates (BCL 0.33sec) as shown in Figure 3.14 (dot-dashed line in the top left panel) very similar to basal state of the model but with small magnitude. On the other hand, 50% I_{Kur} block (in red dotted line) has enhanced the rate dependence of I_{CaL} and I_{Kur} for higher rates after BCL 0.5sec. Both I_{CaL} and I_{Kur} current shows near-to-flat rate dependence for BCL upto 0.5sec. However, the integral of I_{NaCa} current is large in magnitude with its operating mode switched at BCL 0.5sec resulting in a large current in the outward mode that can play a potential role in the rate adaptation of APD under I_{Kur} block. Hence, rate dependent reduction in I_{CaL}, accumulation of Na^+ and resulting I_{NaK}, I_{NaCa} inward current are the major players of APD_{90} rate dependent shortening.

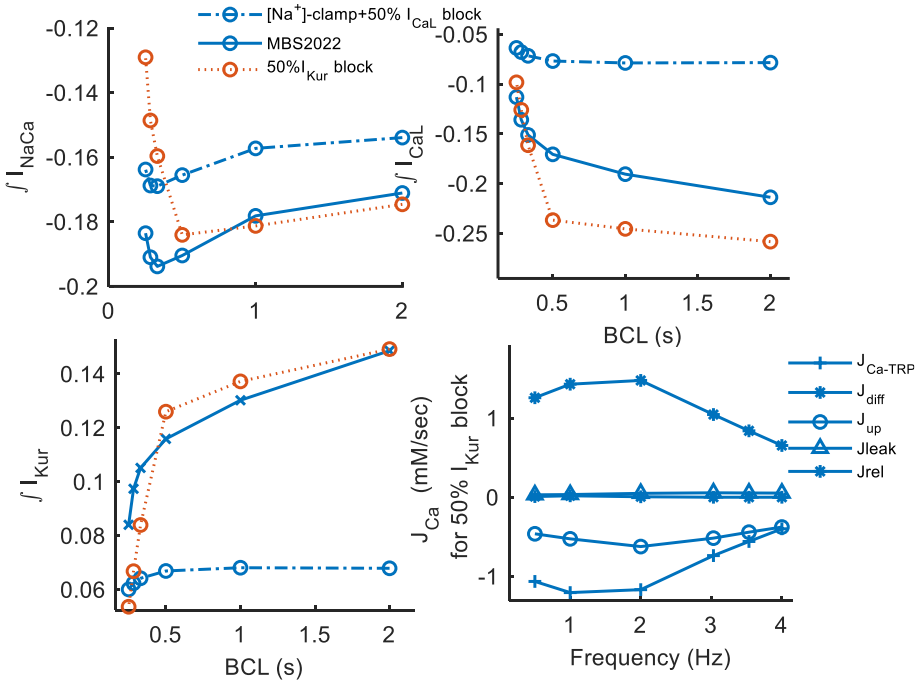

Figure 3.14: Effect of each simulation test defined in Figure 3.11 on current integrals, I_{NaCa} normalized with respect to each BCL (top left), I_{CaL} (top right), I_{Kur} (bottom left). The peak inward and outward Ca^{2+} fluxes in the bulk cytosol are reproduced (bottom right) for 50% I_{Kur} block simulation.

Our model shows an increase in CaT and F_{active} peaks with rate (Figure 3.12I) up to 3.5Hz and then a decline afterwards. Experimental data about this rate dependence are quite sparse, making a close fitting of them not meaningful. Rather our focus was to investigate the mechanisms that give rise to biphasic rate dependence of the CaT. Therefore, we performed a detailed analysis of the inward and outward Ca^{2+} fluxes to/from the *bc* compartment and their rate dependence and quantified the contribution of each flux at each increasing rate. The major source of Ca^{2+} accumulation with rate is the prominent rise of diastolic Ca^{2+} (see Figure 3.12I) because of less time available for its complete removal from the bulk. The Ca^{2+} efflux is mainly dependent on J_{up}, whereas transient sequestration of Ca^{2+} by $J_{Ca\text{-}TRPN}$ during the systolic phase strongly modulates

the CaT peak, as also shown by simulation in which the MCF is absent (Figure 3.10D). An increasing Ca^{2+} content in SR with rate (from 0.615 to 0.821 mM for frequency 1Hz to 4Hz) is shown by the model and it is in accordance with experimental evidence (Maier *et al.* 2000) from human atrial myocytes. An increasing $[Ca^{2+}]_{SR}$ might produce an increasing J_{rel}, however the model produced a J_{relbc} with very small amplitude which is always decreasing with rate. The main reason lies in the refractoriness of RyR gate that resulted in unavailability of fully activated RyR channels with increasing frequency. On the other hand, J_{relss} has faster dynamics than J_{relbc} and it demonstrates a biphasic behavior with increasing rate (not shown) that impacts on J_{diff} rate dependency. Consequently, J_{diff} peak increases slightly at lower rates (up to 1 Hz) and then reduces progressively with rate. On the other hand, after 3Hz, a combined reduction of outward fluxes J_{up} and $J_{Ca\text{-}TPRN}$ was observed. Hence, this balancing of Ca^{2+} fluxes was observed at each frequency; therefore, inward flux was dominant till 3Hz after which the outward flux took the charge.

The testing of rate dependent trend of percentage change in CaT_{peak} was carried out in Figure 3.13 (right) where the biphasic decline (at 4Hz) became less pronounced under $[Na^+]_{ss}$-clamp and was completely lost under the combination of 50% block I_{CaL}+$[Na^+]_{ss}$-clamp simulation test. On the other hand, 50% I_{Kur} block shifted the declining phase back to 3Hz frequency hence, reproducing the experimental trend (Figure 3.12J). Apart from increasing the Ca^{2+} concentration in the cytosol by the increased activation of I_{CaL} (Figure 3.14 top right red dashed line), I_{Kur} block provided us with the Ca^{2+} homeostasis inside the bulk cytosol that can provide an insight into the underlying biphasic CaT rate adaptation property. All the inward and outward flux peak values were plotted with rate in Figure 3.14 bottom right panel. Hence, a rate dependent increase in J_{diff} resulted in Ca^{2+} accumulation upto 2Hz and the combined decreasing outward flux $J_{Ca\text{-}TRPN}$ and J_{up} after 2Hz produced a decline of Ca^{2+}.

In ventricular myocardium the percentage increase in twitch followed by the CaT with respect to rate is less pronounced than atrium as was analyzed by Maier et al. (Maier *et al.* 2000). At lower rates, the ventricular myocardium shows a lower SR-Ca^{2+} uptake that substantially increases with frequency even more than atrial uptake i.e. at 3Hz ~20% greater than atrial myocardium. Moreover, Maier et al. observed postrest potentiation of force in ventricles (not in atrial tissue) that is related to a strong SR-Ca^{2+} uptake activity (Maier *et al.* 2000). Thus, the atrial myocardium is characterized by a strong exchanger activity (Benardeau *et al.* 1996) with increased density than in rat ventricular myocytes (Callewaert *et al.* 1989). Overall, both atrial and ventricular myocardium demonstrates a positive force-frequency relationship that is marked with different subcellular mechanisms owing to the differences in EC coupling and Ca^{2+}-handling.

In this chapter, a new electro-mechanical model for human atrial cardiomyocytes along with mechano-electric regulations was presented. The model was developed, calibrated, and evaluated with a wide range of *in-vitro* data. The model depicts a physiologically accurate description of Ca^{2+}-handling that can reproduce many experimental phenomena and help to gain insights into the pathophysiological mechanisms. This computationally efficient and coupled model opens new pathways for future multi-scale modelling and investigation of human atrial electromechanics.

Chapter 4

Model Validation based on Ca^{2+}-handling Mechanisms: Electrolyte Concentration variations & Post-operative Atrial Fibrillation

The content of this chapter is re-produced from:

"A Detailed Mathematical Model of the Human Atrial Cardiomyocyte: Integration of Electrophysiology and Cardiomechanics."

***Fazeelat Mazhar**, Chiara Bartolucci, Francesco Regazzoni, Michelangelo Paci, Cristiana Corsi, Luca Dedè, Alfio Quarteroni, and Stefano Severi.*

Under revision in Special Issue 'Cardiac Mechano-Electric Crosstalk' in Journal of Physiology.

Abstract

Post-operative AF (PoAF) is a commonly occurring arrhythmia and adds into the complication of cardiac surgery. The presence of pre-operative arrhythmogenic substrate initiates the PoAF when passed through post-(or pre-) operative triggers. Several mechanisms have been associated with PoAF and many preventive treatments have been suggested but still the prevalence is substantial. In this chapter, we aim to simulate two possible mechanisms that can produce an arrhythmogenic substrate and can lead to PoAF condition using our recently developed electromechanically coupled model, MBS2022. The first simulation was the depression of SERCA activity that resulted in the incidence of alternans at 4.2Hz frequency and was associated with the slow inactivation time of ryanodine receptor (RyR) gate. The second simulation test was 50% increase in I_{CaL} current resulting in early afterdepolarization (EADs) in the model. On running the alternans protocol it was found that other than RyRs, CaMKII inhibition can enhance the alternans vulnerability by nearly 2 times indicating a strong modulatory effect of AP morphology on induction and degree of Ca^{2+} alternans. The electromechanical coupling protects the model from beat-to-beat oscillations due to dampening effect of Ca troponin binding. Among contraction parameters, the enhanced thin filament binding affinity can lessen the alternans propensity in the model. This chapter also presents the role of extracellular Ca^{2+} concentration variations on intracellular Ca-homeostasis and the inotropic effect of atrial specific I_{Kur} current block as a validation of our coupled model.

4.1 Introduction

Atrial Fibrillation (AF) is a common form of atrial arrhythmia that has a high mortality and morbidity rate (Benjamin *et al.* 1998) and is becoming more prevalent among aged population (Miyasaka *et al.* 2006). AF is associated with a commonly occurring arrhythmia in an immediate period after cardiac surgery known as Post-operative AF (PoAF), sometimes also named as secondary AF (Dobrev *et al.* 2019). PoAF can occur in 20-50% of patients after cardiac surgery with a peak incidence between post-operative day 2 and 4 (Hindricks *et al.* 2021). Several mechanisms have been associated with PoAF and many preventive treatments have been suggested but still the prevalence is substantial.

PoAF is induced by transient pre-operative triggers when interacting with a pre-existing arrhythmogenic substrate. The arrhythmogenic substrate does not include any sign of electrical remodeling in PoAF patients (Swartz *et al.* 2009). Nevertheless, Van Wagoner et al. observed that the chronic AF (cAF) patients were characterized by a reduced L-type Ca^{2+} current (I_{CaL}) and the patients from control group who experienced PoAF, independent of age difference and myocyte size, have the greatest I_{CaL} current (Van Wagoner *et al.* 1999). Hence, the study observed a significant correlation between the pre-operative Ca^{2+} current density with the propensity of the patients to develop PoAF. Few other studies found Ca^{2+}-handling abnormalities as a potential trigger for not only in cAF but also for PoAF patients. Heijman et al. analyzed the pre-existing Ca^{2+}-handling abnormalities characterized by depressed Ca^{2+}-transient (CaT), leaky and over-sensitization of RyRs, and enhanced Ca^{2+} release events (Heijman *et al.* 2020). The increased Ca^{2+}/Calmodulin-dependent protein kinase-II (CaMKII) protein expression and phosphorylation were associated with increased RyRs open probability and increased sarcoplasmic reticulum

ATPase (SERCA) activity was an indication for leaky RyRs with no change in SR-Ca^{2+} content. In contrast, Fakuade et al. reported a slowing of SERCA activity in the patients from control group who developed PoAF (Fakuade *et al.* 2021) however, the CaMKII phosphorylation effect was not considered in this study.

In this chapter, we will present the incidence of PoAF using a novel electro-mechanically coupled computational model, MBS2022, presented in Chapter 3. These simulation tests can be considered as a validation of the newly developed model in accordance with the cellular mechanisms described above.

4.2 Methods

In this chapter, we will present the applications Ca-handling related mechanism for our newly developed model, MBS2022. The model is an electro-mechanically (EM) coupled model with proper consideration of feedforward and feedback pathways. The model also includes CaMKII-induced phosphorylation effect with well-defined atrial-specific targets. The model is a multi-compartmental cell level structure that is computationally efficient with detailed slow Ca^{2+}-diffusion towards the bulk as described in detail in Chapter 3.

4.2.1 Extracellular [Ca^{2+}] variations on MBS2022 model

Using MBS2022, we validated the model by varying the extracellular Ca^{2+} concentration and analyzing the intracellular Ca^{2+}-homeostasis for MBS2022 model using the experimental data from human atrial tissue (Brixius *et al.* 1999). The quantitative analysis of $[Ca^{2+}]_o$-variations on intracellular environment was carried out using biomarkers both from CaT and contraction force (F_{active}) like systolic peak (CaT_{peak}, $F_{active\ peak}$), time to reach peak systolic value ($ttp_{Factive}$), relaxation time at 50% and 90% of the peak ($rt_{50Factive}$ and $rt_{90Factive}$).

4.2.2 Atrial specific I_{Kur} current block

Another validation test was analyzing the inotropic response of atrial specific, ultra-rapid delayed rectified outward K^+ current (I_{Kur}) block. The drug dose dependent (4-AP and AVE0118) I_{Kur} current block is simulated and its impact on action potential (AP), contractility and CaT has been analyzed using human atrial data (Wettwer *et al.* 2004, Schotten *et al.* 2007).

4.2.3 Post-Operative Atrial Fibrillation simulation and experimental studies

The third validation test is the simulation of PoAF associated pro-arrhythmogenic abnormalities that can be analyzed in the form of beat-to-beat oscillations in CaT and AP i.e., alternans or by the occurrence of delayed and early after depolarizations (DADs and EADs). The PoAF arrhythmogenic substrate was simulated in two ways i.e. by increasing I_{CaL} current up to 50% (Van Wagoner *et al.* 1999), by the depression of SERCA activity, expression and pumping rate (Fakuade *et al.* 2021).

In general, the vulnerability of Ca^{2+} induced alternans is often associated with steep non-linear $[Ca^{2+}]_{SR}$ dependence on J_{rel} (Díaz *et al.* 2004; Xie *et al.* 2008). However, cytosolic Ca^{2+} alternans are also observed without any significant concurrent oscillations in diastolic $[Ca^{2+}]_{SR}$ in single myocytes (Hüser *et al.* 2000; Picht *et al.* 2006). For instance, (Shkryl *et al.* 2012) observed

experimentally in rabbit atrial myocytes that the inactivation kinetics and the refractoriness of RyR release was the key mechanism behind Ca^{2+} alternans generation. Similar results were observed from experiments in human atrial cells (Llach *et al.* 2011) where the mechanism proposed for alternans was the slow recovery of release. For this reason, in the MBS2022, we have a slow recovery time for RyR gates, both in *ss* and *bc* compartments, by increasing the recovery from inactivation time from its standard value of 200msec (Stern et al. 1999). This was achieved in the model by increasing the inactivation time constants for the recovery period from 15msec to 450msec and from 87.5msec to 656msec for *ss* and *bc* compartments respectively. Moreover, the inactivation time constant for *ss* compartment was also updated from 15msec to 60msec. In this way, the J_{rel} fluxes for *ss* and *bc* were having a slow decay time and hence a comparable total time duration.

4.2.3.1 Alternans protocol

In MBS2022, AP and CaT alternans requires faster rates under control condition. To quantify the role of potential parameters both from AP and contractility in the incidence of alternans at higher rates we used a pacing protocol similar to that used in a clinical study by Narayan et al. (Narayan *et al.* 2011) and in computational modeling (Zile & Trayanova 2018). Under isometric condition, at basic cycle length (BCL) of 750ms the model is paced for 1000 beats to reach the steady state condition. Using this steady state value as initial condition, the model was paced for 74 beats for successive BCLs within a window of 500ms to 200ms in a 50msec descending increments. From our literature study, the parameters that were analyzed using this pacing protocol were: Ca-handling related: the RyR inactivation time (tau_{inact}), SERCA pumping rate ($k_{4\text{-}SERCA}$), SERCA expression ([SERCA]); Contraction related: thin filament Ca^{2+} binding sensitivity ($k_{d\text{-}TRPN}$), thin filament rate constant (K_{off}), cross bridge cycling (XB_{cy}), rate constant (K_{basic}); Model related: by switching off the mechano-calcium feedback (no MCF) effect (as described in detail in Chapter 3); and CaMKII related: by inhibition of CaMKII effect, and by the increased expression of CaMKII.

Based on a comprehensive alternans analysis (Zile & Trayanova 2018), we defined a similar measure to quantify the magnitude of AP and CaT alternans. Alternans normalized magnitude (ANM) was calculated as the mean of change over the consecutive last 10 pair of beats during a BCL divided by mean value over the last 10 beats and is given as:

$$ANM = \frac{\sum_{b=63}^{73} |X_b - X_{b+1}|/10}{avg(X)_{b=64\ to\ 74}}$$

where X is AP or CaT biomarker like APD_{90}, APD_{50}, and CaT_{peak} hence, we have three alternans measures namely, APD_{90}-ANM, APD_{50}-ANM and CaT-ANM. The threshold used for alternans to be considered significant was ANM >5%.

4.3 Results

4.3.1 Inotropic effect of extracellular [Ca^{2+}] variation on MBS2022

The evaluation of Ca^{2+} handling mechanism underlying the intracellular Ca^{2+} homeostasis of the model was carried out by simulating the elevation of extracellular Ca^{2+} concentration $[Ca^{2+}]_o$

from 0.9 to 3.2mM. In line with experiments (Brixius et al. 1997) Figure 4.1A (left), the model reproduced the elevation of CaT and F_{active} systolic and diastolic levels, as shown in Figure 4.1B (on right, top and bottom panels respectively). The percentage change trend of systolic (triangles) and diastolic (open circles) for CaT (in red) and F_{active} (in blue) is shown in Figure 4.1B (bottom). The diastolic rise is equivalent for both CaT and F_{active} whereas, the systolic level elevation is more pronounced than CaT for all $[Ca^{2+}]_o$ values. The comparison of percentage rise in systolic peaks of CaT and F_{active} with experimental data is quantified in panel C (left panel). Consistently with experimental evidence, the model shows a significant percentage rise in F_{active} and CaT throughout the varying $[Ca^{2+}]_o$ and this appreciated more at 3.2mM where a 172% rise in F_{active} and 140% in CaT was achieved. Similarly, we compared percentage change of F_{active} biomarkers for $[Ca^{2+}]_o$ variation from 0.9 to 3.2mM in Figure 4.1C (right panel): there is no substantial difference in percentage changes of biomarkers for F_{active} as can be seen in the experimental values.

The diastolic rise of CaT with elevated $[Ca^{2+}]_o$ can be speculated as a result of more Ca^{2+} influx via Ca^{2+} channels in the subspace and less efflux either via SERCA activity or the I_{NaCa} exchanger current. Since the model lacks T-tubules hence, inside the bulk cytoplasm, the rise in Ca^{2+} influx is mainly due to 175% increase in diffusion flux (J_{diff}) and slightly because of release flux (J_{relbc}) whereas, the extrusion of Ca^{2+} is dependent on SERCA uptake. Under $[Ca^{2+}]_o$ elevation model showed a 123% rise in SR-Ca^{2+} content (not shown) thus also resulting in more Ca^{2+} bound to TRPN. Hence, these changes of intracellular CaT with varying $[Ca^{2+}]_o$ were accompanied by a rise in diastolic and systolic values of F_{active}.

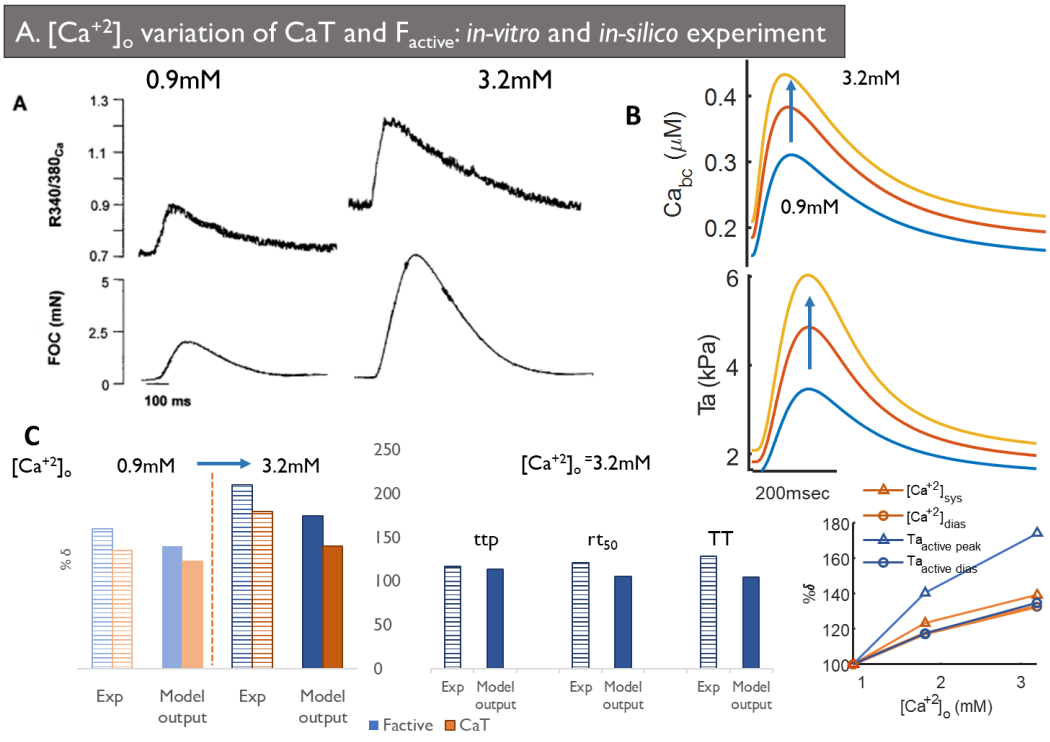

Figure 4.1: Extracellular Ca^{2+} ($[Ca^{2+}]_o$) variation effect on MBS2022. A& B) Experimental data (Brixius *et al.* 1997) for CaT (fura-2 ratio) (top) and F_{active} elevation (bottom) with $[Ca^{2+}]_o$ compared with *in-silico* results of CaT (top) and F_{active} (bottom) time course, B) bottom panel compares percentage rise of systolic (triangles) and diastolic (open circles) for CaT (in red) and F_{active} (in blue). C) F_{active} and CaT biomarkers response to $[Ca^{2+}]_o$ variations. (On left) Percentage change of systolic peaks of F_{active} (red bars) and

CaT_{bc} (blue bars) compared with the experimental data with respect to 0.9mM $[Ca^{2+}]_o$, (On right) percentage change in kinetics of F_{active} using biomarkers ttp, rt_{50} and TT with same experimental data.

4.3.2 Inotropic response of I_{Kur} current block

The block of I_{Kur} current is expected to prolong the AP plateau that will eventually lead to an increase in contractility. Accordingly, we analyzed the blocking effect of I_{Kur} by setting the current conductance g_{Kur} to 100%, 80% and 20% of its regular value. In accordance with the experiments (Wettwer *et al.* 2004), the *in-silico* model reproduced the prolongation of the plateau phase as shown in Figure 4.2A. Moreover, a change of AP-morphology from type 3 to type 4 (Dawodu *et al.* 1996) for human atria is also observed at a higher percentage (80%) of I_{Kur} block. The AP biomarkers' response to I_{Kur} blocking is shown in Figure 4.2A (on the right). AP biomarkers included APD at 20% and 30% of repolarization (APD_{20}, APD_{30}) and the plateau potential (PP) calculated as a mean voltage amplitude within a time window of 20 to 80 ms after the upstroke. In line with experiments (Wettwer *et al.* 2004), APD_{30} prolongs from 8 to 105 msec and the plateau potential raises from -16 to +10 mV with the increasing block percentage of I_{Kur}. In contrast, we observed a lengthening of APD_{90} in the model instead of a shortening as reported in the experiments (Wettwer *et al.* 2004).

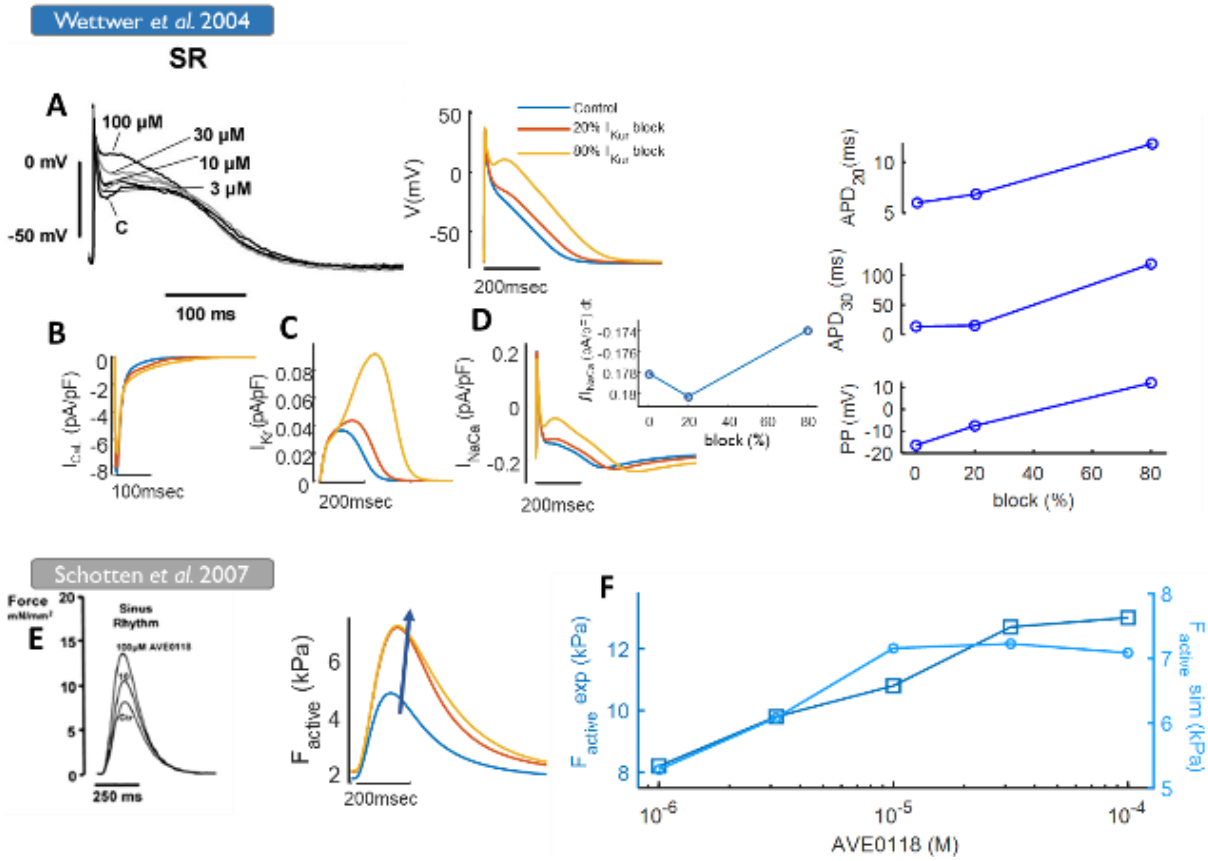

Figure 4.2: Effect of I_{Kur} blocker on MBS2022. A) *In-silico* results of I_{Kur} blocking on AP time course compared with *in-vitro* experiments (Wettwer *et al.* 2004). The AP biomarkers were shown, plateau potential (PP), APD_{30} and APD_{20} trend. Secondary effect of I_{Kur} blocking on B) I_{CaL} current C) I_{Kr} current and D) I_{NaCa} with the integral (in the inset), E& F) compares the drug concentration dependent inotropic response of the model with experimental data (Schotten *et al.* 2007).

The model also demonstrated the secondary effect of I_{Kur} blockage on AP. As a result, an increased amplitude of I_{CaL} current was observed at more positive AP potential (Figure 4.2B). Consequently, large I_{CaL} activated more outward repolarizing currents like I_{Kr} (Figure 4.2C) and I_{Ks} (not shown). The reduced activation of Na^+ channels results in decreasing steady state Na^+ concentration in the cytosol. Hence, a secondary reduction of I_{NaCa} inward current can be observed initially followed by a slight increase in Figure 4.2D. The integral of I_{NaCa} current (inset) shows a shift of exchanger activity to outward mode with decreasing current magnitude at high percentage of block i.e. 80%. The positive inotropic response of our model is in line with the human experimental results (Schotten *et al.* 2007) (Figure 4.2E). The concentration dependent effect of I_{Kur} block (Kv1.5) by AVE0118 is modelled using the formulation by Decher (Decher *et al.* 2006). Based on this relation our model showed good agreement (in open circles) with the elevation of contractility by the various degree of I_{Kur} block (Figure 4.2F) as reported in experiments (open squares).

4.3.3 Simulation of impaired SERCA activity as a mechanism for Post-operative AF

Simulations were conducted to reproduce experimental findings on impaired Ca^{2+} handling contribution to the development of PoAF (Fakuade *et al.* 2021). Following the experimental protocols, we simulated the model from 0.5 to 5Hz of frequency and analyzed the mechanism behind the incidence of CaT and AP alternans under control conditions and the alternans threshold shifting in the PoAF condition. Following the experimental results, the PoAF condition was reproduced in the model by reducing the SERCA activity, i.e. the pumping rate by 70% and the expression levels, to 80%. The onset of AP and CaT alternans at high frequency is reproduced by our model as shown by the biomarker bifurcation diagram in Fig. 4.3A&B. The biomarkers for AP are APD_{50} and APD_{90} (Figure 4.3A), and for CaT the amplitude of CaT peaks at consecutive beats in *bc* (Figure 4.3B left) and *ss* (Figure 4.3B right) compartments. In the bifurcation diagram, the divergence point is the key indicator of alternans initiation. Hence, under control condition (100% SERCA activity) (in blue), alternans both in AP and CaT appeared at a frequency of 4.6 Hz. In the experiment (Fakuade *et al.* 2021), the threshold for AP and CaT alternans was shifted down to lower frequency in the PoAF group. This alternans threshold shifting is reproduced by the model under PoAF condition (in red). Hence, a higher susceptibility to AP and CaT alternans was found under PoAF, as the alternans threshold was shifted to 4.2 Hz. Furthermore, under PoAF, a reduced Ca^{2+} level is seen in the *ss* compartment (Figure 4.3B right) with respect to control (red vs blue) with no change in *bc* CaT levels (Figure 4.3B left). The consecutive three beats, in terms of AP (first panel), CaT in *ss* (solid line) and *bc* (dashed line) (second panel) and $[Ca^{2+}]_{SR}$ time course (third panel) evoked at 4.2 Hz under control condition are shown in Figure 4.3C & D. A similar plot of AP, CaT and $[Ca^{2+}]_{SR}$ under PoAF (Figure 4.3C & E in red) illustrates the beat-to-beat alternations in CaT systolic and diastolic levels both in *ss* and *bc* compartments (left panel) and in $[Ca^{2+}]_{SR}$ release and end diastolic value (right panel).

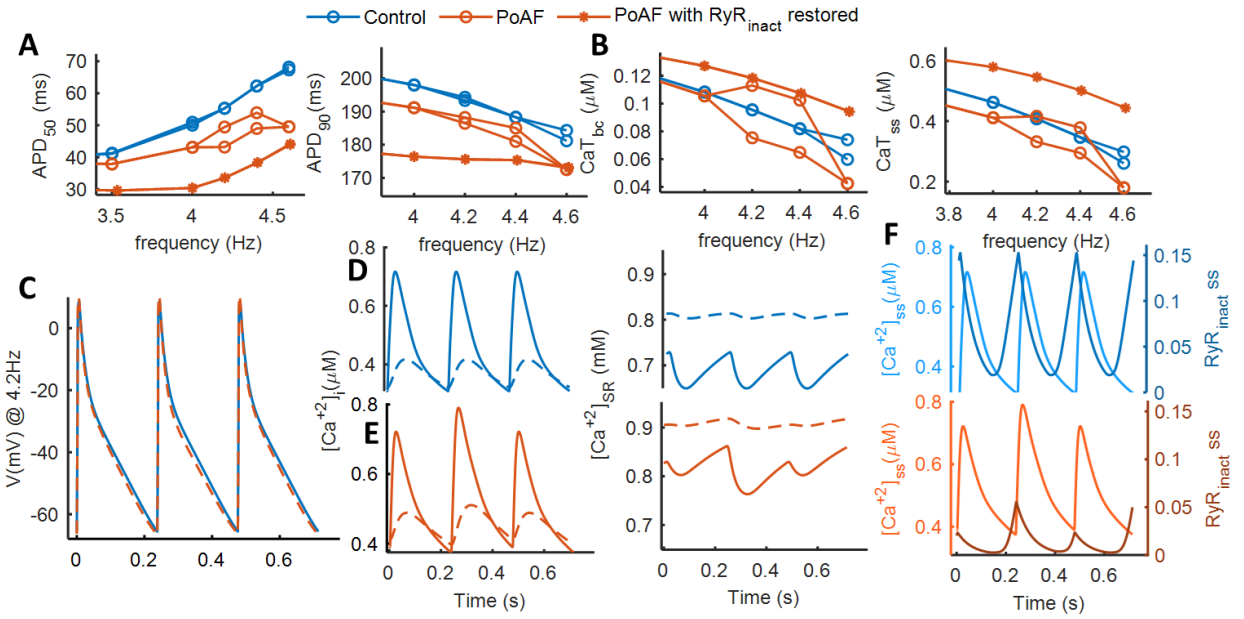

Figure 4.3: Effect of SERCA activity variation as a measure of PoAF condition on MBS2022 model. The SERCA activity was reduced from 100% (control in blue) to 80% of SERCA expression and 70% of pumping rate (PoAF in red). A) Bifurcation diagram of AP biomarker (APD_{50}) (left panel), and APD_{90} (right panel), B) difference of CaT amplitude on the consecutive beats of CaT in *bc* (left panel) and *ss* (right panel) compartments at different frequencies. C) Last three beats at 4.2Hz for AP superimposed on each other under control (in blue solid line) and PoAF (in red dashed line), D& E) consecutive three beats for CaT in both compartments (left panels) and Ca^{2+} concentration in SR, $[Ca^{2+}]_{SR}$ (right panels) at 4.2Hz in control (D) and PoAF (E) conditions. F) Shows consecutive beats of RyR steady-state inactivation gate in comparison with CaT from *ss* compartment at 4.2Hz under control and PoAF condition.

The mechanism for the onset of CaT alternans is investigated in Fig. 4.3F by plotting the consecutive beats of RyR steady-state inactivation gate for the *ss* compartment at 4.2 Hz for control (top) and PoAF condition (bottom). Under control conditions (Figure 4.3F top panel), the peak availability of RyR gate is about 16%, it is uniform all along the consecutive beats, and this gives a stable CaT in the subsequent beats (in light shade). In contrast, in PoAF (bottom panel), the model demonstrates beat-to-beat alternations in RyR inactivation and recovery from inactivation time. The recovery from inactivation is not uniform from beat to beat, as a consequence the availability of RyR gate is alternating between 3% to 6% resulting in short and long CaT respectively. Hence, the refractoriness of RyRs in the *ss* compartment was the main cause of alternans incidence in the model under PoAF condition.

4.3.3.1 Dissecting parameters involved in alternans development

With the help of alternans pacing protocol, we have investigated the role of contraction, Ca-handling, CaMKII, and MCF effect on the model that can be appreciated by APD_{90}-ANM and CaT-ANM scores as shown in Figure 4.4, where the ANM threshold is shown in red dashed line. The control model MBS has a propensity of alternans incidence at a BCL of 200ms where Ca alternans are stronger than APD as shown by the ANM score (7.34 vs 5.9% in red bars). Among the contraction related parameters, the slowing of transition rates K_{off} and K_{basic} did not play a significant role in strengthening the alternans magnitude. On the other hand, the reduced sensitivity of thin filament i.e increasing $k_{d\text{-}TRPN}$ by two times results in enhancement of alternans more for

CaT than APD (ANM scores: 12 vs 9%) and the alternans completely vanished on decreasing $k_{d\text{-}TRPN}$. The parameter that has the greatest impact on alternans magnitude is the coupling effect i.e. MCF feedback as shown in Figure 4.4 with greater sensitivity to CaT oscillations than APD (ANM score: 18.5 vs 13.75%). This major rise in ANM score is a consequence of the enhanced level of free CaT in the cytosol that is achieved because of the absence of Ca-TRPN bound in the model. Ca-TRPN has a dampening effect on the beat-to-beat oscillations that is even enhanced by increasing the Ca-TRPN binding affinity as was seen already by reducing $k_{d\text{-}TRPN}$ parameter.

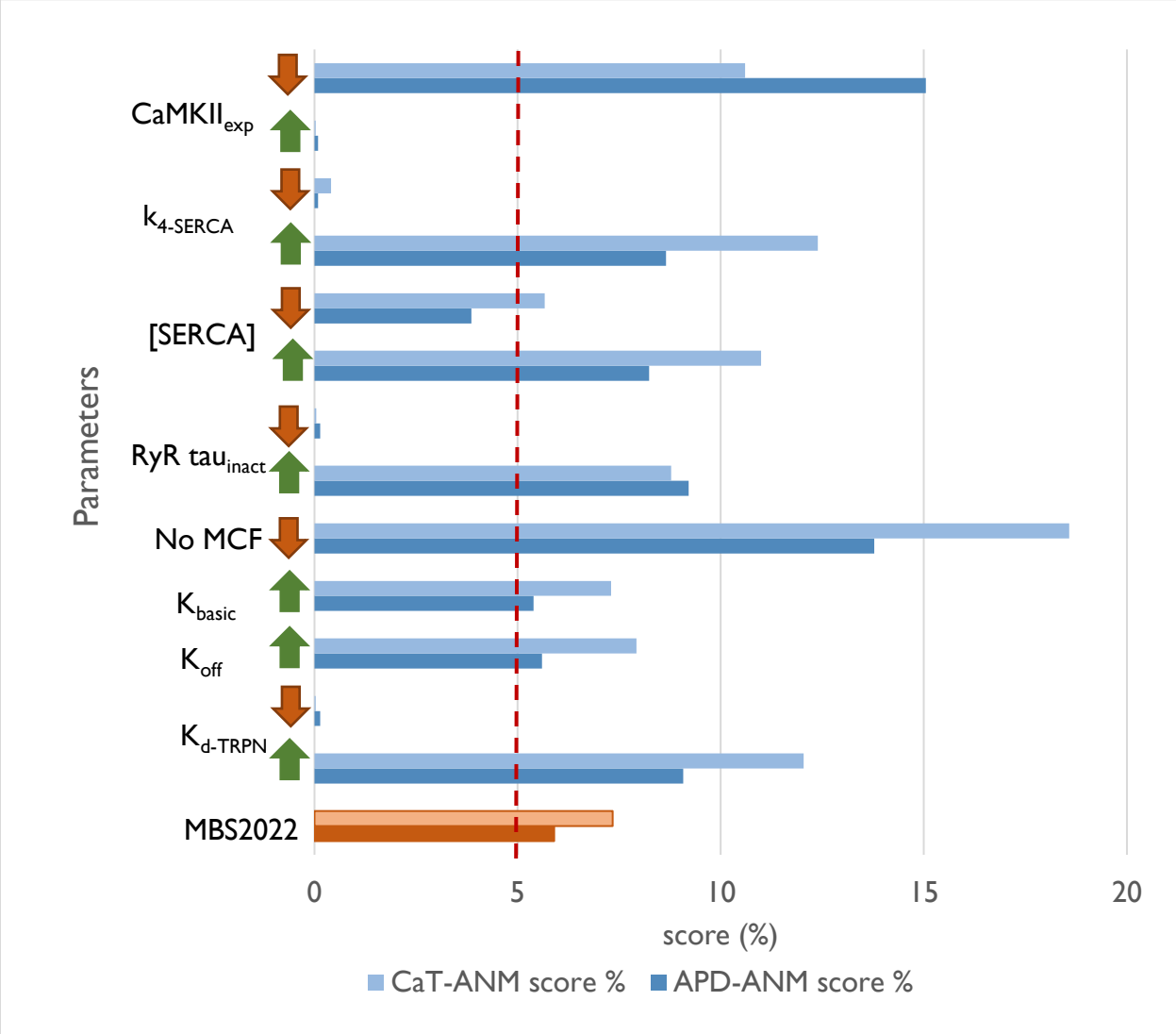

Figure 4.4: Effect of parameter variations on alternans normalized magnitude (ANM) for CaT_{peak} (CaT-ANM) (in light shade) and APD_{90} (APD-ANM) (in dark shade). Parameters related to Ca-handling: RyR inactivation time ($RyR_{tauinact}$), SERCA activity i.e. expression level ([SERCA]), pumping rate ($k_{4\text{-}SERCA}$); Electromechanical coupling: mechano-calcium feedback (MCF) induced by Ca^{2+}-TRPN binding; Contraction: thin filament transition rate (K_{off}), sensitivity ($kd_{\text{-}TRPN}$), and cross bridge cycling (XBcy) rate (K_{basic}); CaMKII: expression ($CaMKII_{exp}$).

Among the Ca-handling parameters, the slow inactivation of RyR release gates has slightly reversed the trend i.e. this parameter is more vulnerable to APD alternans than CaT with ANM score of 9.2 vs 8.78%. The enhanced SERCA activity is favorable for alternans vulnerability, as

demonstrated by enhanced SERCA expression and pumping rate. The CaMKII effect is protecting MBS2022 model against the incidence of alternans. The CAMKII inhibition induces very strong alternans in APD with ANM 15.05% that is even greater than the CaT ANM magnitude (10.6%). Overall, the presence of electromechanical coupling reduces the alternans induced vulnerability in the model where the sensitivity of the thin filament is the key modulator of alternans development. In Ca-handling, enhanced SERCA activity and RyR slow inactivation time can play their role in increasing the alternans incidence probability in our model. The role of each parameter discloses some insight mechanisms behind the alternans vulnerability as will be explained more in discussion section.

4.3.4 Increased I_{CaL} current as a mechanism of Post-operative AF

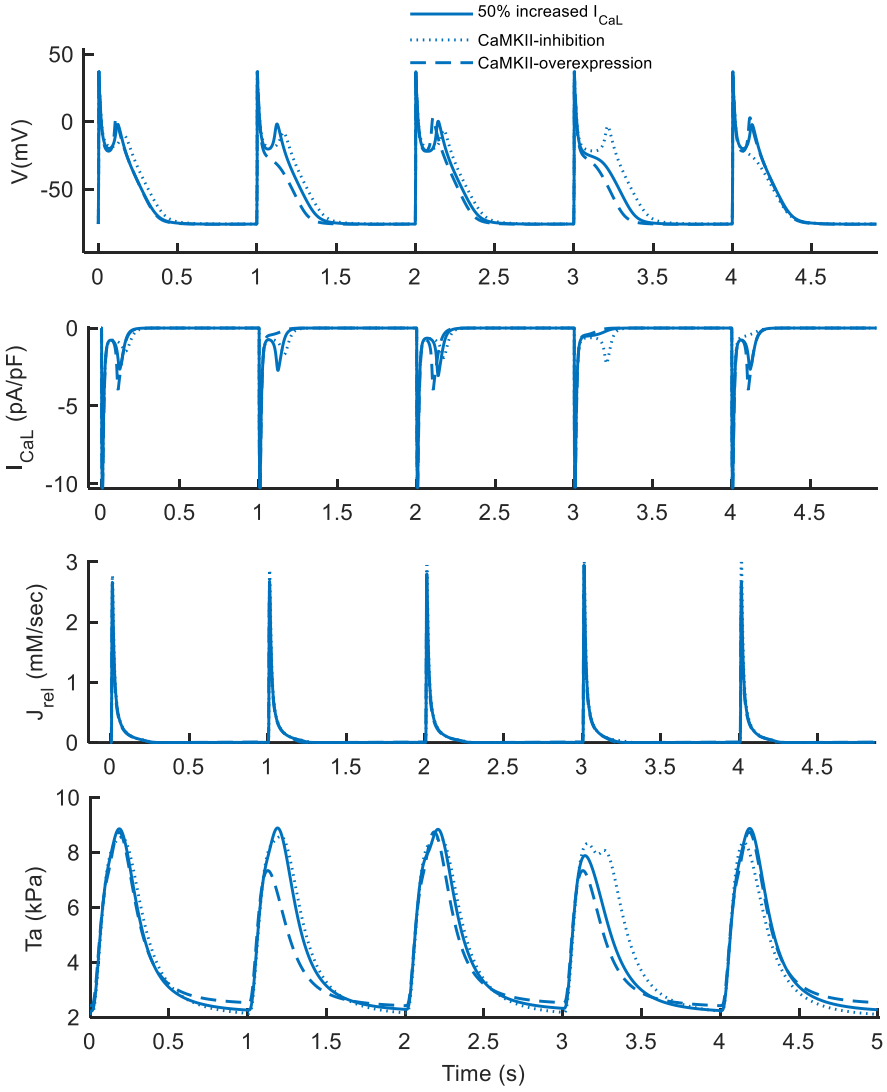

Figure 4.5: Early afterdepolarizations (EADs) triggered by 50% increase in I_{CaL} current (solid lines) and role of CaMKII inhibition (dotted lines) and over-expression (60% increase) (dashed lines). The reactivation of I_{CaL} current (second panel) triggers an EAD in the AP (top panel). The CaMKII expression level is strengthening the EADs magnitude and oscillation in contraction (bottom panel) and release flux (J_{rel}) (third panel).

We reproduced the experimentally observed positive correlation between pre-operative I_{CaL} and the occurrence of PoAF by Van Wagoner (Van Wagoner *et al.* 1999). The simulation for 50% increase in I_{CaL} current triggered EADs as shown in Figure 4.5. The AP waveform is shown in the top panel from where it can be anticipated reactivation of I_{CaL} current (second panel) is the reason for this abnormal AP behavior given that there is no spontaneous Ca^{2+} release behavior from release flux (J_{rel}) (third panel).

The CaMKII role for strengthening the EADs was evaluated since in our model CaMKII targets the I_{CaL} by slowing the voltage dependent inactivation (VDI) time (as shown in Chapter 3). Hence, we tested our hypothesis that CaMKII inhibition would remove or at least weaken the EADs magnitude. We tested the same simulation under CaMKII inhibition (dotted line) and over expression (dashed line) (160% increase) conditions to quantify the EADs magnitude by computing mean voltage (V_{mean}) from 7 to 16ms time window. The model demonstrated that CaMKII inhibition reduced the EADs magnitude i.e. V_{mean} became more negative from -11.8 to -25.22mV whereas, for CaMKII overexpression it tends to be more positive -10.4mV. The over expression of CaMKII also induced oscillations in contraction as can be seen in third panel Figure 4.5. Hence, CaMKII over expression can accelerate the EADs trigger for PoAF condition with a pre-operative increased I_{CaL} acting as an arrhythmogenic substrate.

4.4 Discussion and Conclusions

We have presented a detailed validation study based on Ca^{2+}-handling homeostasis and remodeling effects. Both excitation and contraction parameters are analyzed from MBS2022 model that can be involved in the initiation of arrhythmogenic phenomenon. Ca^{2+} homeostasis is analyzed by the variation of $[Ca^{2+}]_o$ variations, the positive inotropic effect of I_{Kur} block has been observed and two different simulations for PoAF condition have been tested i.e. increased I_{CaL} current and depressed SERCA activity.

Inotropic effect of I_{Kur} blocking

I_{Kur} blocking enhances atrial AP plateau which can be therapeutically beneficial for treating atrial contractile dysfunction (Schotten *et al.* 2007) thus reducing AF burden in persistent AF (Ford *et al.* 2016) and chronic AF (Wettwer *et al.* 2004) groups. In accordance with the experiments, the model can reproduce and explain the positive inotropic response on I_{Kur} blocking (Figure 4.2). The elevated plateau potential and duration predict secondary effect of I_{Kur} block on membrane currents like an increase in I_{CaL} and I_K (I_{Ks} and I_{Kr}) currents. The secondary effect of reduced I_{NaCa} current integral is an outcome of a combined rise in Ca^{2+} and a decrease in Na^+ concentration. The integral shows a reduced magnitude of current at 80% block that also depicts that the exchanger is working more in outward mode thus contributing to APD_{90} lengthening response.

On the other hand, the model shows a contradictory result too, i.e. a lengthening of APD_{90} instead of a shortening as is reported in human atrial myocytes (Wettwer *et al.* 2004). The reason for this discrepancy lies in the low maximal conductance value of I_{Kr} current present in our AP module, which was adopted from the parent model. Indeed, KM2011 inherited that conductance value from the Nygren model which was shown to have a very small I_{Kr} with respect to CRN (Cherry *et al.* 2008). A detailed calibration of I_{Kr} formulation for human atrial myocytes will be

the objective for future developments of our model. Therefore, the overall effect of I_{Kur} block was a prolongation of APD_{90}. In addition, the type-3 AP morphology has either shown no substantial effect on APD_{90} with I_{Kur} blocking with still an increase in the contractility as observed by Schotten in canine myocytes (Schotten *et al.* 2007) or a lengthening effect (Li *et al.* 2008, Wang *et al.* 1993) and in human atrial cell *in-silico* models (Grandi *et al.* 2011, Nygren *et al.* 1998). Hence, AP morphology can decide the response of I_{Kur} block on APD_{90}. The I_{Kur} current block response is highlighted in much detail in Chapter 6 too. Based on these observations, the model predicted that a strong positive inotropic effect is not dependent on the late repolarization phase of the AP, whereas the AP plateau phase is crucial for this phenomenon.

Depressed SERCA activity can affect the alternans threshold

Reduced atrial contractile function is a predictor of PoAF (Fakuade *et al.* 2021). Based on this fact, it was observed experimentally that SERCA activity reduction was the only mechanism of impaired Ca^{2+} handling in a PoAF patient group. Based on this observation, we simulated the depression of SERCA activity by reducing SERCA expression by 80% and pumping rate by 70% and analyzed the mechanism underlying the onset of alternans in the model (Figure 4.3). The model produced alternans at 4.2 Hz under PoAF but not under control conditions. In our model, under PoAF condition, due to SERCA depression the removal of calcium from the cytoplasm and refilling of SR between two successive releases is slowed down (Figure 4.3E). Consequently, the diastolic value of Ca^{2+} in *ss* is relatively high, keeping it into a range for which recovery from inactivation of RyRs is very small. In this condition, the amount of available RyRs at the beginning of two successive releases can change a lot (more than doubled, from 0.024 to 0.058, in Figure 4.3F). In other words, the 'gain' of the feedback loop into the intracellular calcium handling system is very high, and this gives rise to oscillations/alternans. The beat-to-beat alternans in CaT are translated into AP shape due to Ca^{2+} dependent channels and transporters. Therefore, CaT was the driving mechanism of AP alternans demonstrated by comparing the APD_{50} and APD_{90} as a measure of AP alternans. Hence, under PoAF, reduced SERCA activity results in the slowing of J_{up}, that can promote alternans even at modest SR loads and small release consistent with the results found in rabbit atrial myocytes (Shkryl *et al.* 2012). Consequently, the slow uptake results in less Ca^{2+} J_{rel} flux and the small release with slow recovery kinetics contributed to moving the alternans threshold down to 4.2Hz under PoAF condition inline with the findings of human atrial myocytes (Llach *et al.* 2011).

Parameters involved in alternans incidence

The alternans pacing protocol was used to dissect the role of parameters from contraction, CaMKII activation, Ca^{2+}-handling and MCF effect in alternans incidence. We found that CaMKII based phosphorylation protects the model from alternans development (Figure 4.4). In our model, the CaMKII modulates the Ca^{2+}-handling by increasing the SERCA pumping rate and reducing the Ca^{2+}-SERCA binding affinity. Hence, under CaMKII inhibition, the raised SR-Ca^{2+} content induced because of increased SERCA binding affinity, enhances the RyR release steeply as the activation probability is now in a steeper region of fractional SR Ca release curve as also seen experimentally (Shannon *et al.* 2000). The role of fractional SR Ca release curve in causing dynamical instability in Ca^{2+} leading to Ca^{2+} induced alternans that has been recently reviewed by Weiss group (Qu & Weiss 2023; Weiss *et al.* 2006) and has also been observed in experiments

(Díaz *et al.* 2004). Apart from this, CaMKII inhibition has strengthened the APD alternans ANM score more than the CaT. A study by Kanaporis & Blatter (Kanaporis & Blatter 2017) in rabbit atrial myocytes demonstrated a strong modulatory effect of AP morphology on induction and degree of Ca^{2+} alternans. The key mechanisms behind the Ca alternans were the SR Ca load (that also confirms our first observation) and the regulatory kinetics of I_{CaL} current. Under CaMKII inhibition, the small CaT magnitude will inactivate less I_{CaL} showing a weak CDI effect and resulting in a small and slower I_{CaL} current that will eventually trigger less SR Ca^{2+} release. Hence, a large I_{CaL} current with fast dynamics (under CaMKII overexpression in our case) can lower the degree of CaT alternans occurrence that is inline with Kanaporis & Blatter experimental results (Kanaporis & Blatter 2017).

Among Ca-handling parameters, the SR activity has a prominent role in the onset of Ca^{2+} alternans. The SR Ca^{+2} uptake for a given fractional SR Ca release curve slope together predicts the Ca^{2+} cycling stability as was analyzed experimentally by Xie et al. where they found a smaller SR Ca^{2+} uptake as a promoter of alternans and was more sensitive to change in fractional SR Ca release curve slope (Xie *et al.* 2008). In MBS2022 model, it was found that SR uptake pumping rate was slower when compared with caffeine induced CaT experimental data (Figure 3.11F). Hence, the increased SR uptake activity obtained by doubling the pumping rate (Figure 4.4) has not made the SR fast enough to recover back to the same SR Ca load before the next beat arrives at higher BCLs. Thus this incomplete filling of SR can be a cause of beat-to-beat fluctuation in SR Ca^{2+} load leading to Ca^{2+} alternans as was also observed in experiments (Díaz *et al.* 2004).

For contraction related parameters, the increase in Ca-TRPN binding affinity was protecting the model from alternans incidence. However, increased myofilament Ca^{2+} sensitivity is often considered a common attribute of many inherited and acquired cardiomyopathies that are associated with cardiac arrhythmias (as reviewed by Huke & Knollmann 2010). In contrast, Shettigar et al. observed that Ca^{2+} sensitization induced by gene therapy *in-vivo* does not lead to disease but can be utilized to protect and therapeutically aid the heart in a murine model of myocardial infarction (Shettigar *et al.* 2016). Similarly, in our model, the enhanced Ca^{2+} sensitivity of TRPN results in more Ca^{2+} binding to the TRPN hence reducing the J_{up} flux that has enough time to reach its diastolic value during a single beat. Therefore, it is less likely that SR Ca load will generate a beat-to-beat oscillation in the CaT.

In conclusion, in this chapter, we have presented three validation tests related to Ca^{2+}-handling mechanisms for our newly developed model. The model highlights the therapeutic potential of I_{Kur} block for treating atrial contractile dysfunction. We have presented a detailed analysis of the propensity of the model towards alternans incidence by simulating two different mechanisms and running the dynamic alternans protocol. Overall this model will open pathways to study the cause/effect mechanisms under various pathological conditions.

Chapter 5

Modeling Mechano-Electric Feedback and its role in arrhythmogenesis

The content of this chapter is re-produced from:

"A Detailed Mathematical Model of the Human Atrial Cardiomyocyte: Integration of Electrophysiology and Cardiomechanics."

Fazeelat Mazhar*, Chiara Bartolucci, Francesco Regazzoni, Michelangelo Paci, Cristiana Corsi, Luca Dedè, Alfio Quarteroni, and Stefano Severi.*

Under revision in Special Issue 'Cardiac Mechano-Electric Crosstalk' in Journal of Physiology

Abstract

Atrial Fibrillation is associated with many risk factors related to the changing mechanical environment. Mechanical stretch favors the development of arrhythmogenic substrate for AF. In this chapter, based on our recently developed electromechanically coupled model MBS2022, we aim to quantify the effect of stretch variations on the action potential, Ca^{2+}-transient (CaT) and the active force of contraction at basal rates and to analyze the role of stretch in rate dependency. Using the model, we also investigated the role of varying preload in alternans vulnerability and highlighted some insights into the underlying mechanism. The rise in stretch lengthens the APD and depolarizes the resting potential by 31.6% which drops to 8.3% with a reduced sensitivity to stretch. The analysis reveals that increased preload enhances the CaT systolic peak because of increased binding affinity to troponin buffer. Finally, increased stretch level is vulnerable to alternans incidence at higher rates that is mainly related to increased activation of the troponin and cooperative activation of the neighboring regulatory units. Hence, the rise in stretch can play a potential role in the initiation of arrhythmogenic events.

5.1 Introduction

Atrial Fibrillation (AF) is a common cardiac arrhythmia (Kornej *et al.* 2020). Out of many other risk factors of AF, the changing mechanical circumstances are related to the occurrence and maintenance of AF. Mechanical overload (Neves *et al.* 2016) and chronic atrial dilation (Schotten *et al.* 2003, Ravelli & Allessie 1997, Ravelli 2003) can play a role in the initiation of arrhythmia. Atrial stretch favors the development of arrhythmogenic substrate for AF by inducing afterdepolarizations and by promoting reentrants either by increasing atrial surface area or by shortening of the refractory period, and by conduction slowing via spatial dispersion.

Several experimental evidence shows that atrial stretch and dilation can modulate the electrophysiological characteristics of the atria and can promote arrhythmogenic events. Ravelli et al. found that atrial dilation was the major determinant of AF vulnerability in Langendorff-perfused rabbit hearts that was closely related to the shortening of the effective refractory period (ERP) (Ravelli & Allessie 1997). Another study by Bode et al. found a similar observation of AF propensity in isolated rabbit heart during atrial stretch (Bode *et al.* 2000). In human atrium, stretch induced spatial distribution of local conduction velocities was related to a significant rise in AF vulnerability (Ravelli *et al.* 2016). Xie et al. observed an association between the AF incidence and higher right atrial volume indices in a large multiethnic population (n=3147 participants) (Xie *et al.* 2020).

The channels that can produce potentially arrhythmogenic electrophysiological changes are the mechano-activated channels (MAC) named stretch activated currents (I_{sac}). On the cellular scale, MAC are the stretch activated gates whose open probability is modulated as a response to stretch. Very often, the I_{sac} are subdivided into K^+ selective (I_{K0}) and non-selective (I_{ns}) cations channels. I_{ns} allows Na^+, Ca^{2+} and K^+ to enter the cells and the reversal potential, based on the relative permeability of ion channels, is halfway between the RMP and the plateau potential i.e. 0 and -50mV and has a near-linear voltage dependence (Kim 1993). Hence, the activation of I_{ns} can depolarize the cells, while during the plateau phase can cause repolarization of the AP. In contrast, the reversal potential of I_{K0} is close to RMP hence, can modulate the repolarization phase more

than the RMP of the AP. In this chapter, we have only considered the MAC effect that is simulated by I_{ns} current and all the simulations are done under isometric condition where the sarcomere is contracting. Hence, using our recently developed model MBS2022, presented in Chapter 3, we will demonstrate the effect of stretch mediated by I_{ns} current. The mechanical activity of the cell is modeled using a three-element rheological scheme. Hence, in this chapter we will show the changing effect of preload on contractility at basal rates and its relevance with the Frank-Starling law of the heart. The simulation is extended to see the role of stretch at higher rates and its behavior towards the development of alternans.

5.2 Methods

Using our newly developed electromechanically coupled model, MBS2022, we demonstrated the effect of stretch variations on the action potential (AP), Ca^{2+}-transient (CaT), and active force of contraction (F_{active}). For this, we included the mechano-electric feedback (MEF) based manifestations in the model. We included the I_{sac} in the model as subdivided into K^+ selective (I_{K0}) and non-selective (I_{ns}) cations channels. The I_{ns} current parameters were calibrated based on the average current values on negative pressure ranging from 0 to 80mmHg extracted from Jakob *et al.* (Jakob *et al.* 2021). Using the calibrated I_{ns} current the stretch was varied by varying preload. For this, we included the mechanical activity model of the cardiomyocyte based on passive element using three-element rheological scheme (Solovyova *et al.* 2002). Using the calibrated I_{ns} current and the preload effect, we extended the analysis to the rate adaptation of AP and CaT and its possible role in the development of alternans.

The AP, CaT, and F_{active} related biomarkers were used to quantify the relevance of the simulation results with the experiments. Thus, the AP biomarkers are AP duration at 50% and 90% of repolarization (APD_{50}, APD_{90}), the amplitude (V_{amp}), the resting membrane potential (RMP), and the maximal velocity of the upstroke (dV/dt_{max}). Similarly, CaT and F_{active} biomarkers were the systolic peak (CaT_{sys}, F_{peak}), the diastolic level (CaT_{dias}, F_{diast}), the relaxation time at 50% of the peak (rt_{50}), and the total time duration (T_{Ca}, TT) respectively.

5.2.1 Stretch activated channel formulation

The I_{ns} is a near-linear voltage dependent current with a reversal potential between -50mV to 0mV (Kim 1993). In the model, the current is permeable to Na^+, K^+ and Ca^{2+} and it is defined as:

$$I_{ns} = I_{ns,Na} + I_{ns,K} + I_{ns,Ca}$$

here I_{nsX} is the contribution of current permeable due to X ions where X can be Na^+, K^+ or Ca^{2+}. The driving force of each I_{nsX} is modeled by Goldman-Hodgin-Katz (GHK) based formulation:

$$I_{nsX} = P_x g_{ns} \frac{z_x^2 F^2 V_m}{RT} \frac{[X]_i - [X]_o \exp\left(-\frac{z_X F V_m}{RT}\right)}{1 - \exp(-\frac{z_X F V_m}{RT})}$$

here P_X decides the permeability ratio of Na^+, K^+ and Ca^{2+}, and z_X is the ion valence for each ion, and the rest of the constants are defined as in KM2011. For our model the permeability ratio, P_{Na}

: P_{Ca} : P_K was fixed as 1:1:1 that gives a linear V-I relationship for I_{ns} current with a reversal potential near 0mV (Fig. A6 in red triangles) as was shown for rat atrial myocytes (Kim 1993). A sensitivity analysis of increasing permeability of each ion channel by 3 times at a time depicted that change in P_{Na} and P_K can increase (25mV) and reduce (-25mV) the reversal potential of I_{ns} respectively as shown in Fig. 5.1 (in yellow plus marks and in blue squares respectively). Moreover, Kim suggested P_{Ca}/P_K ratio to be equal to 0.9 (Kim 1993) and we have adopted this ratio from Kuijper et al. as 1 (Kuijper *et al.* 2008). Thus, we opted for an equal permeability ratio for all the three ion channels in our model. The effect of stretch change was introduced in the I_{ns} current by conductance g_{ns} equation given as,

$$g_{ns} = \frac{g_{nsmax}}{1 + K_{ns}\exp\left(-\alpha_{ns}(\lambda - 1)\right)}$$

where g_{nsmax} is the maximal conductance, K_{ns} is the parameter that defines the amount of current in the absent of stretch (λ=1), and α_{ns} is the sensitivity to stretch. Furthermore, the I_{ns} current formulation was included in electrolyte equations as:

$$\frac{d[Na^+]_i}{dt} = \frac{-(I_{Na} + I_{Nab} + 3 * I_{NaK} + 3 * I_{NaCa} + I_{fNa} + I_{ns,Na})}{V_{ss}F}$$

$$\frac{d[K^+]}{dt} = 0$$

$$\frac{d[Ca^{+2}]_{ss}}{dt} = \frac{-I_{CaL} - I_{Cab} - I_{CaP} + 2 * I_{NaCa} - I_{ns,Ca}}{2 * V_{ss}F}$$

where V_{ss} is the volume occupied by the *ss* compartment, and the rest of the constants are same as the original model. All other minor modifications in conductance values have been listed in Table A1 C. For I_{K0} current, we have considered the formulation for rat ventricular myocytes by Niederer and Smith (Niederer and Smith 2007). Briefly, the conductance is a function of strain and is modeled as,

$$\gamma_{K0} = \beta_{K0}(\lambda - 1) + 0.7$$

and I_{K0} becomes,

$$I_{K0} = g_{K0}\,\frac{\gamma_{K0}}{1 + \exp -\frac{10 + V}{45}}\,(V - E_K)$$

All the constants were the same as was used in the original work (Niederer and Smith 2007).

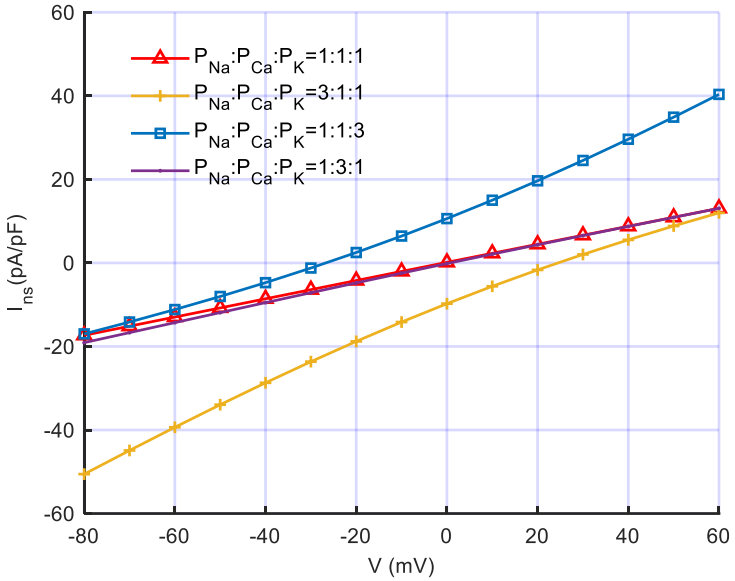

Figure 5.1: I-V plot for non-selective stretch activated current density I_{ns} showing plots for equal permeability ratio (in red triangles), for P_{Na} increased 3 times (in yellow plus marks), for P_K increased 3 times (in blue squares), and for P_{Ca} increased by 3 times (in purple dot markers).

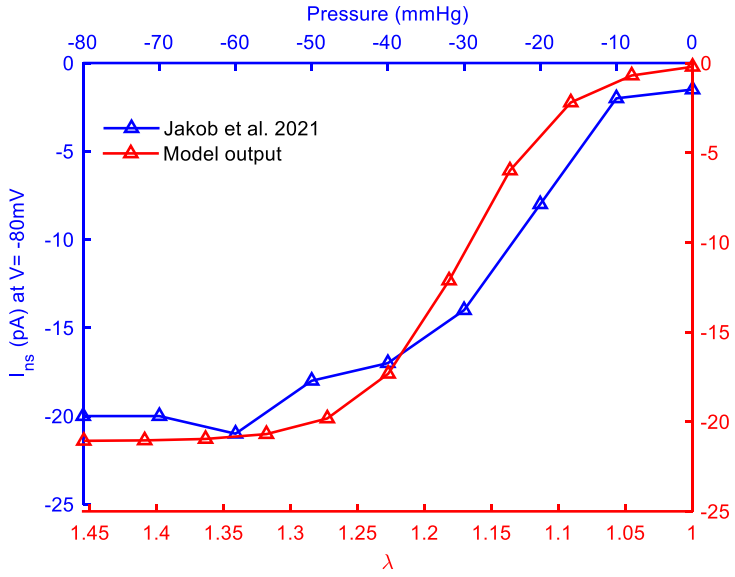

Figure 5.2: Non-selective cation ion stretch activated current (I_{ns}) (model output in red) validated against the average-currents for all negative pipette pressures tested (from 0 to −80 mmHg) for 110 cells obtained from Jakob et al. 2021 (in blue).

5.2.1.1 Parameter Validation for I_{ns}

We have validated the I_{ns} current parameters based on the average current values on negative pressure ranging from 0 to 80mmHg extracted from Jakob *et al.* (Jakob *et al.* 2021). The measurements are obtained from 11 tissue donors and 110 cells. The model output for I_{ns} current (in red line) fit on the experimental data is shown in Fig. 5.2 (in blue line). The model output I_{ns} current increases upto λ=1.25 followed by a plateau that fits qualitatively with the experimental average current values i.e. -20pA. The calibrated set of parameters, thus obtained, are listed in

Table A1 section C which shows a high sensitivity towards stretch i.e. α_{ns}=27 and a maximum conductance of g_{nsmax}=0.513e-6 nS. The permeability ratio is fixed same for all three ion channels. Using these calibrated parameters of I_{ns}, we evaluated the effect of increasing stretch level on the MBS2022 model in the Results section.

5.2.2 Three-element rheological scheme

The mechanical activity is modeled using three-element rheological scheme introduced by Hill in 1938 (Hill 1938) and modeled by Solovyova (Solovyova *et al.* 2002) and later by Kuijpers *et al.* (Kuijpers *et al.* 2008) as shown in Fig. 5.3. The contractile element (CE) is responsible for generating the active force (F_{active}) and is the one produced by RDQ2020 module. The element has a length of l_{CE} and a resting length, l_{CEr} i.e., the length when the segment is relaxed, and no force is applied. The force developed by CE unit is given as,

$$F_{CE} = f_{CE} * F_{norm}(SL, Ca^{2+}, v) \qquad (3)$$

where f_{CE} is a scaling factor and F_{norm} is the normalized active force generated by RDQ2020 module that is dependent on sarcomere length (SL), Ca^{2+} dynamics and the shortening velocity, v of the XBs. The MEF based mechanical modulation of Ca^{2+} is already modelled in RDQ2020 module, since Ca^{2+} bound to troponin (Ca-TRPN) sensitivity, k_d is a function of SL. The passive elastic effect is introduced in two forms i.e., by the series (SE) and parallel (PE) elements. Mathematically, passive force developed by SE and PE were modeled as non-linearly related to length i.e., l_{PE} and l_{SE} and is given as,

$$F_{SE} = f_{SE}\{\exp[k_{SE}(l_{SE} - l_{SEr})] - 1\} \qquad (4)$$

Similarly, for F_{PE},

$$F_{PE} = f_{PE}\{\exp[k_{PE}(l_{PE} - l_{PEr})] - 1\} \qquad (5)$$

where f_{SE} and f_{PE} are the scaling factors, k_{SE} and k_{PE} are the spring constants, and l_{SEr} and l_{PEr} are the resting lengths for each element. Under mechanical equilibrium, the total force of the mechanical segment ($F_{segment}$) is related as, $F_{segment} = F_{PE} + F_{SE}$; and length of the segment as, $l_{PE} = l_{SE} + l_{CE}$; and the series forces as, $F_{SE} = F_{CE}$. The three-element mechanical model equations were solved by using the numerical scheme described by Solovyova (Solovyova *et al.* 2002). Two new state variables were integrated in the model i.e., $l_1 = l_{CE} - l_{CEr}$ and $l_2 = l_{PE} - l_{PEr}$ and Equations (4 & 5) were modified accordingly. Moreover, an assumption on resting lengths was made, $l_{PEr} = l_{CEr}$, and, as a consequence, $l_{SEr} = 0$. Based on this, the mechanical state of each element is defined by l_1, l_2, dl_1/dt, dl_2/dt. For isometric simulations $dl_2/dt = 0$, $dl_1/dt = -v$, and the sarcomere shortening velocity v was modeled as,

$$\frac{dv}{dt} = \frac{F_{CE} - F_{SE}}{Ir} \qquad (6)$$

where Ir is the inertial parameter and all other constant parameter values are listed in Table A1 C part.

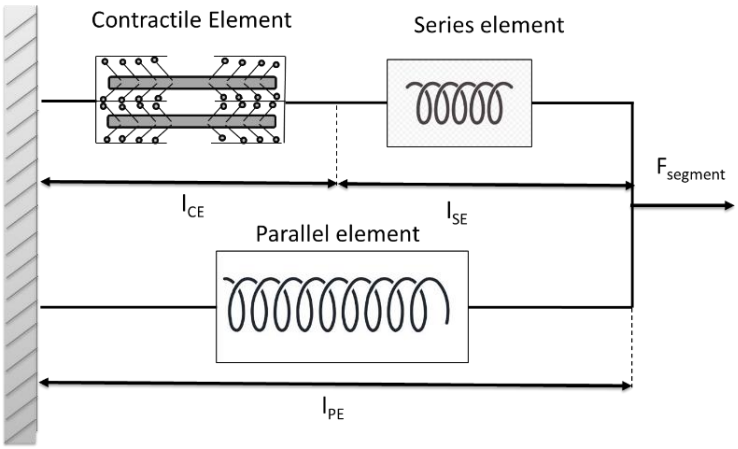

Figure 5.3: Three element rheological scheme for modeling the mechanical activity of the cell in MBS2022 model. The scheme consists of a contractile element of length l_{CE} from RDQ2020 module, responsible for active force development and two passive elements, the series (SE) and the parallel element (PE) of length l_{SE} and l_{PE} respectively.

5.3 Results

5.3.1 Effect of stretch variation on MBS2022

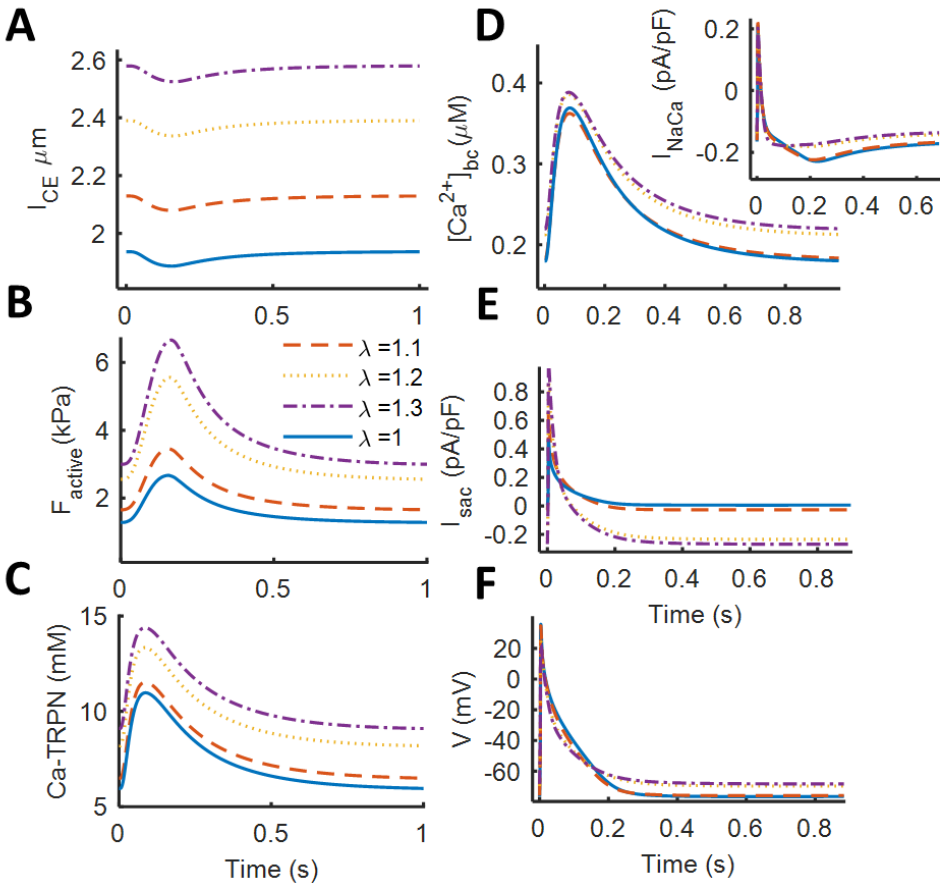

Figure 5.4: MBS2022 model characteristics for stretch variations λ from 1 (in solid blue line), 1.1 (in red dashed line), 1.2 (in yellow dotted line), and 1.3 (in purple dot dashed line). A) The increasing length of contractile element (lCE), B) active contractile

force (Factive), (C) the concentration of Ca2+ bound to troponin (TRPN), D) Ca2+ transient in bulk cytoplasm (bc), INaCa in the inset, E) stretch activated current Isac that is the sum of Ins and IK0, and F) the action potential (AP).

Using the MBS2022 model, we simulated the effect of stretch variations on AP, CaT and F_{active} characteristics under isometric condition, where for a given l_{CE} the preload effect was varied using λ. We simulated the I_{sac} current which is the combination of I_{ns} and I_{K0} currents and varied the λ from 1 (in blue solid line), 1.1 (in red dashed line), 1.2 (in yellow dotted line) to 1.3 (in purple dot dashed line) as shown in Fig. 5.4. The raised preload effect elevates the l_{CE} (Fig. 5.4A) and demonstrates positive inotropic effect (Fig. 5.4B) which is the key depiction of Frank-Starling law of the heart. The increasing F_{active} is a consequence of enhanced sensitivity of Ca^{2+} bound to TRPN as shown in Fig. 5.4C. In line with the observation of Tavi et al. (Tavi *et al.* 1998) for λ =1.1, the rise in F_{active} was not because of increased CaT in the bulk but is caused by the increased sensitivity of the contractile element to Ca^{2+}. For λ=1.2 and onwards, the combined rise in CaT and sensitivity of TRPN results into a more prominent rise in F_{active}. Elevated diastolic CaT level is also observed for λ=1.2 and onwards that can be related to raised SR Ca^{2+} content with varying preload (not shown). For CaT and F_{active} biomarkers, a rise in systolic and diastolic levels is observed with a slight lengthening of time duration (T_{Ca} and TT). The rise in Na^{+} concentration because of stretch modulates the inward I_{NaCa} current (Fig. 5.4D inset) in the early phase of the AP followed by a reduced current in the later phase. The I_{sac} current shown in Fig. 5.4E demonstrates a combined effect of inward I_{ns} and outward I_{K0} currents. For λ=1, 1.1 (in blue solid line and in red dashed line respectively) the I_{sac} is following the I_{K0} current whereas, for λ=1.2 (in yellow dotted line) the effect of I_{ns} predominates as can be seen by the inward current and slow kinetics.

The reversal potential of I_{ns} lies near zero (as shown in Fig. 5.1 in red triangles) whereas the I_{K0} current has a potential quite close to the RMP. This can also be depicted from the separate current time courses shown in Fig. 5.5 panel E. Consequently, the I_{ns} depolarize the RMP of the AP with lengthening of late repolarization i.e. APD_{90} and no effect on the mid repolarization phase i.e. APD_{50} (Fig. 5.5 panel F on left). In contrast, I_{K0} has a slight shortening effect on the late repolarization phase of the AP (Fig. 5.5 panel F on right). The combined effect of I_{sac} on AP can be demonstrated using Fig. 5.4F where the shortening effect is predominant for smaller preload (λ=1, 1.1), and the depolarized RMP is obtained at λ=1.2 and onwards. Consequently, the depolarized RMP demonstrates a 60% slowing of dV/dt_{max} at λ=1.2 and will be discussed in detail in the discussion section. The depolarization of RMP gets strengthened by increased conductance of g_{nsmax} as shown in Fig. 5.6 panel F where the basal state of the model (in yellow) at λ=1.2 demonstrates another 58% slowing of dV/dt_{max} for a 50% rise in g_{nsmax} (in red). This conduction slowing is usually found a consequence of acute atrial dilation that can be considered vulnerable to AF (Ravelli *et al.* 2011).

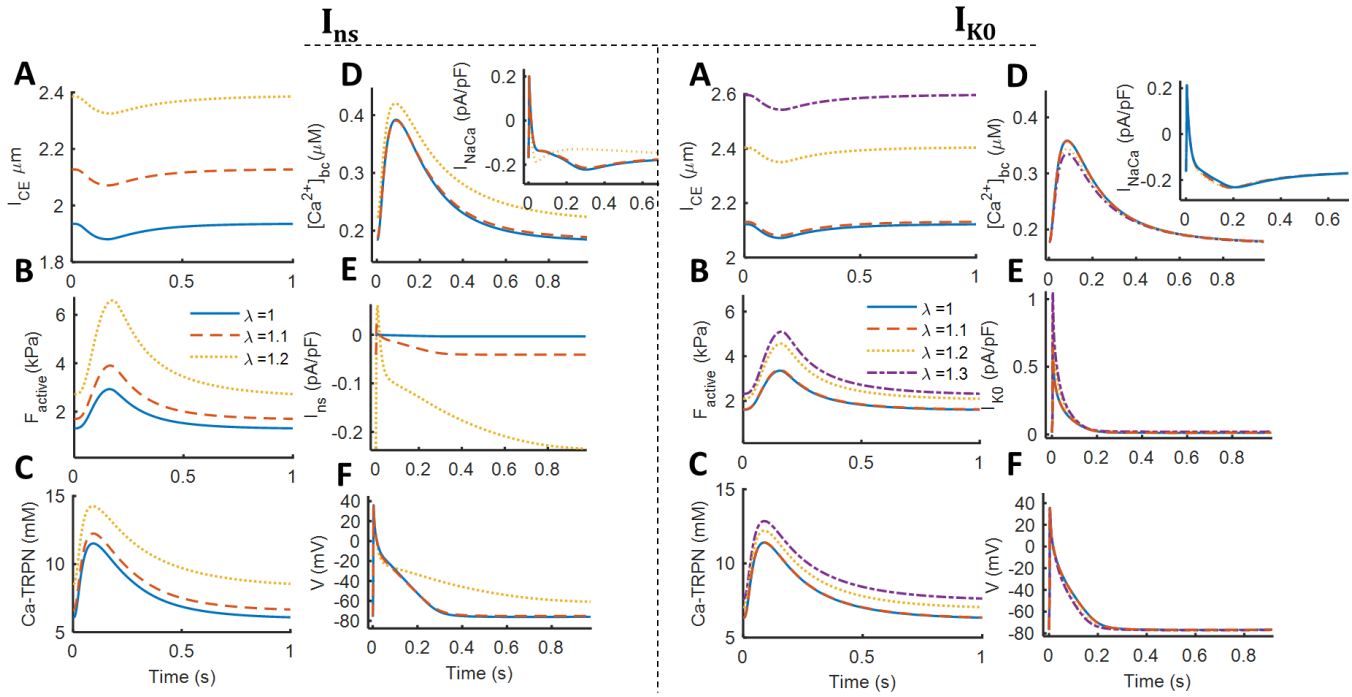

Figure 5.5: MBS2022 model characteristics for stretch variations using non-selective and selective cations current, I_{ns} (on left panels) and I_{K0} respectively (on right panels). Stretch is varied by increasing preload effect, i.e. λ from 1 (in blue solid line), 1.1 (in red dashed lines), 1.2 (in yellow dashed line), and 1.3 (in purple dot dashed line). A) the increasing length of contractile element (l_{CE}), B) active contractile force (F_{active}), (C) the concentration of Ca^{2+} bound to troponin (TRPN), D) Ca^{2+} transient in bulk cytoplasm (*bc*), E) I_{ns} (on left) and I_{K0} (on right) variation with stretch, and F) the action potential (AP).

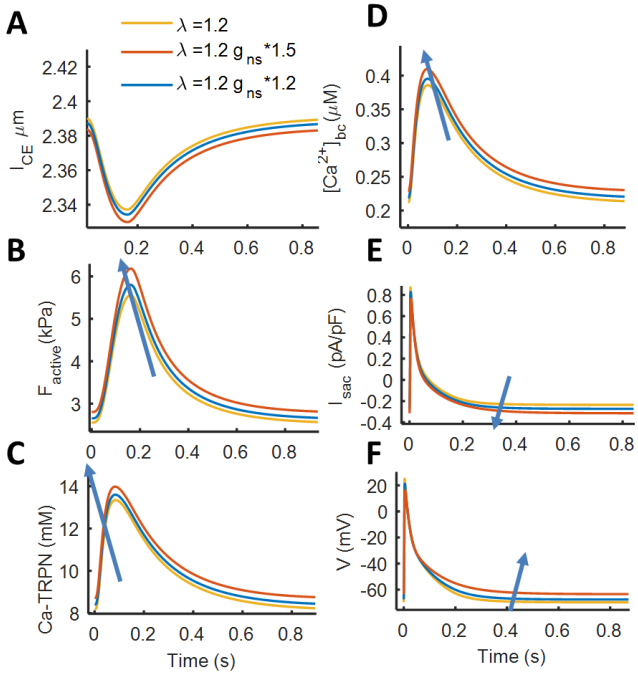

Figure 5.6: Increased conductance g_{ns} of I_{ns} current for λ =1.2 response of model MBS2022. Basal state of the model is in yellow, 20% increase in g_{ns} is in blue, and 50% increase in g_{ns} is in red. A) Length of contractile element (l_{CE}), B) F_{active}, C) concentration of Ca^{2+} bound to TRPN, D) Ca^{2+} transient in the bulk cytosol, E) increasing I_{sac} current, and F) the action potential Vm.

5.3.3 Effect of mechano-electric feedback on rate adaptation

We have analyzed the effect of stretch variation via I_{sac} current on rate adaptation of APD and CaT where the rate varies from BCL=2 to 0.217sec (Fig. 5.7). For λ=1, a large overall shortening of APD_{90} is observed and is shown by the dashed red line in Fig. 5.7A. When the stretch is increased, for λ=1.1 (in yellow dotted line), the APD_{90} demonstrates further shortening with no change in slope. Another rise in λ=1.2 and onwards, the slope of the APD_{90} rate dependent shortening is reversed particularly at BCL=2sec. This can be a consequence of the role of inward current of I_{sac} that becomes prominent only after λ=1.2 and onwards. This depression of APD_{90} with rate is potentially due to the increased outward I_{sac} current contribution in AP for lower λ (Fig. 5.7A) and the change in slope of APD is because of the role of inward I_{sac} that is prominent only for higher λ. Apart from this, the mechanical stretch increases the inward flow of Na^+ ions in the myocytes and hence, can affect the operating modes of Na^+/Ca^{2+} exchanger (I_{NaCa}). Accordingly, we analyzed the time course of I_{NaCa} current for basal rate 1Hz (Fig. 5.7C) and rate dependence of integral of I_{NaCa} current normalized with respect to its BCL (Fig. 5.7D) for all the conditions. Under basal conditions, the rate dependent Na^+ accumulation in the cytosol increases the inward flow of current up to BCL=0.33sec (3Hz on the Fig. 10D) and then there is a shift to outward mode.

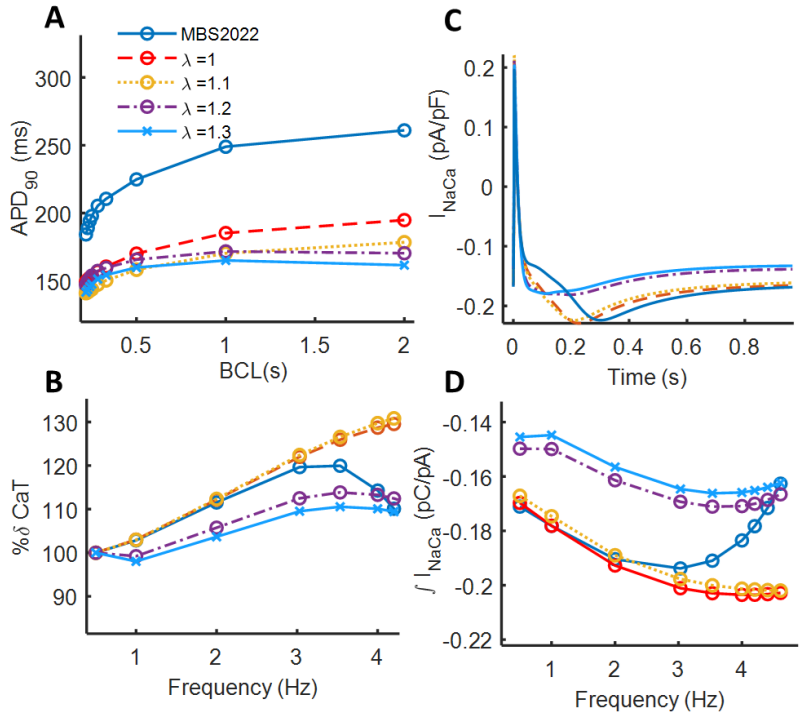

Figure 5.7: Stretch variation response on rate adaptation of APD and CaT. The model was compared under four different simulation settings: control condition as MBS2022 (in blue solid line), λ=1 (in red dashed line), λ=1.1 (in yellow dotted line), λ=1.2 (in purple dot dashed line), and λ=1.3 (solid line with cross). A) appreciates the rate adaptation of APD_{90}; B) shows the rate dependence of percentage change of CaT systolic peaks, and C) shows the time course of I_{NaCa} current and D) integral of I_{NaCa} current trend with rate normalized with respect to each BCL.

The rise in CaT systolic level can be related to the enhanced sensitivity of Ca^{2+}-TRPN bound as was shown in Fig. 5.7C. The rate dependent biphasic behavior of percentage change in CaT_{peak} is shown in Fig. 5.7B (right) where the basal state of the model shows a rise in Ca^{2+} up to 3.5Hz and then a decline. The rate dependency of % change in CaT loses its biphasic trend for lower values of λ=1,1.2 i.e. always increasing however, with the rise in inward I_{sac} current (λ=1.2 and onwards) the biphasic relation is restored at higher frequencies with a trade off of some decreasing current at lower frequency. This trend can be related to the area of I_{NaCa} current normalized with respect to the BCL as shown in Fig. 5.7D. The integral of I_{NaCa} at higher frequencies (from 3Hz and onwards) showing a transition of inward to outward mode of I_{NaCa} current at higher frequencies corresponds to the biphasic relation of CaT. The outward mode of I_{NaCa} allows the entering of Ca^{2+} that via diffusion enters the *bc* and enhances the Ca^{2+}-SR storage that can be depicted by the elevated diastolic level of CaT at λ=1.2 and onwards.

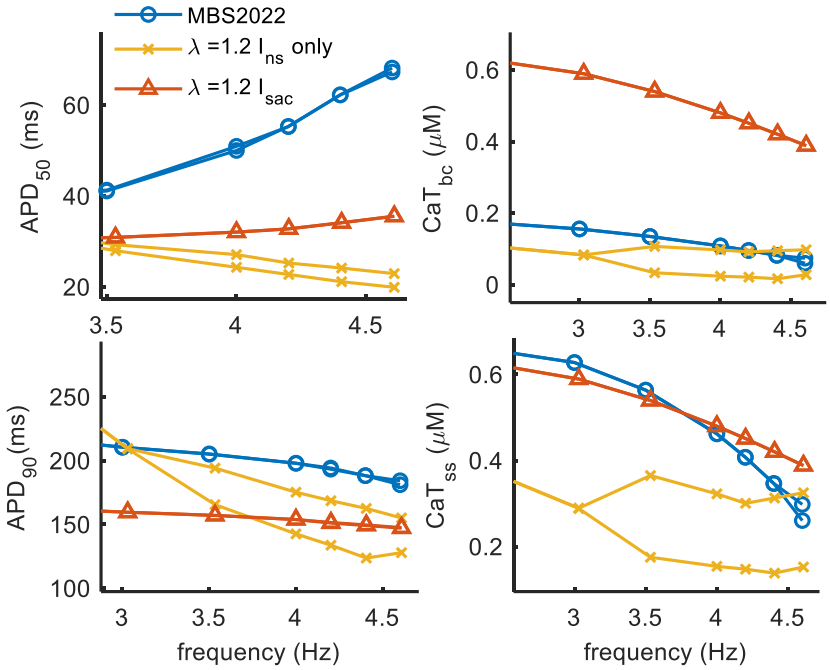

Figure 5.8: Bifurcation diagram illustrating the comparison of basal condition of the model MBS2022 (in blue), under λ=1.2 I_{sac} current (in yellow crosses), and for λ=1.2 I_{ns} only (in red triangles). The divergence of bifurcation branch is a key indicator of alternans incidence in AP biomarkers, APD_{50} (top left), APD_{90} (bottom left), and CaT amplitude in bulk cytosol (bc) (top right) and the subspace (ss) compartments (bottom right).

5.3.4 Stretch strengthens the alternans magnitude

Under isometric conditions, MBS2022 model demonstrates increased vulnerability to alternans incidence when paced for higher rates as shown by the bifurcation diagram in Fig. 5.8. The diagram demonstrates biomarkers for AP, APD_{50} (top left), and APD_{90} (bottom left) and for CaT amplitude both in *bc* and *ss* compartments. The stretch condition at λ=1.2 under I_{sac} (in red triangles) protects the model from both AP and CaT alternans development as was under control condition (in blue). In contrast, the exclusion of outward I_{K0} from I_{sac} current resulted in an

enhanced vulnerability to alternans development as shown by the yellow cross in Fig. 5.8. This shifts the alternans threshold from 4.6Hz to 3.5Hz and has strengthen the magnitude of oscillations (can be seen by increased opening of the branches) for both AP and CaT biomarkers. The exclusion of I_{K0} removes the shortening effect of APD hence, is susceptible to alternans incidence.

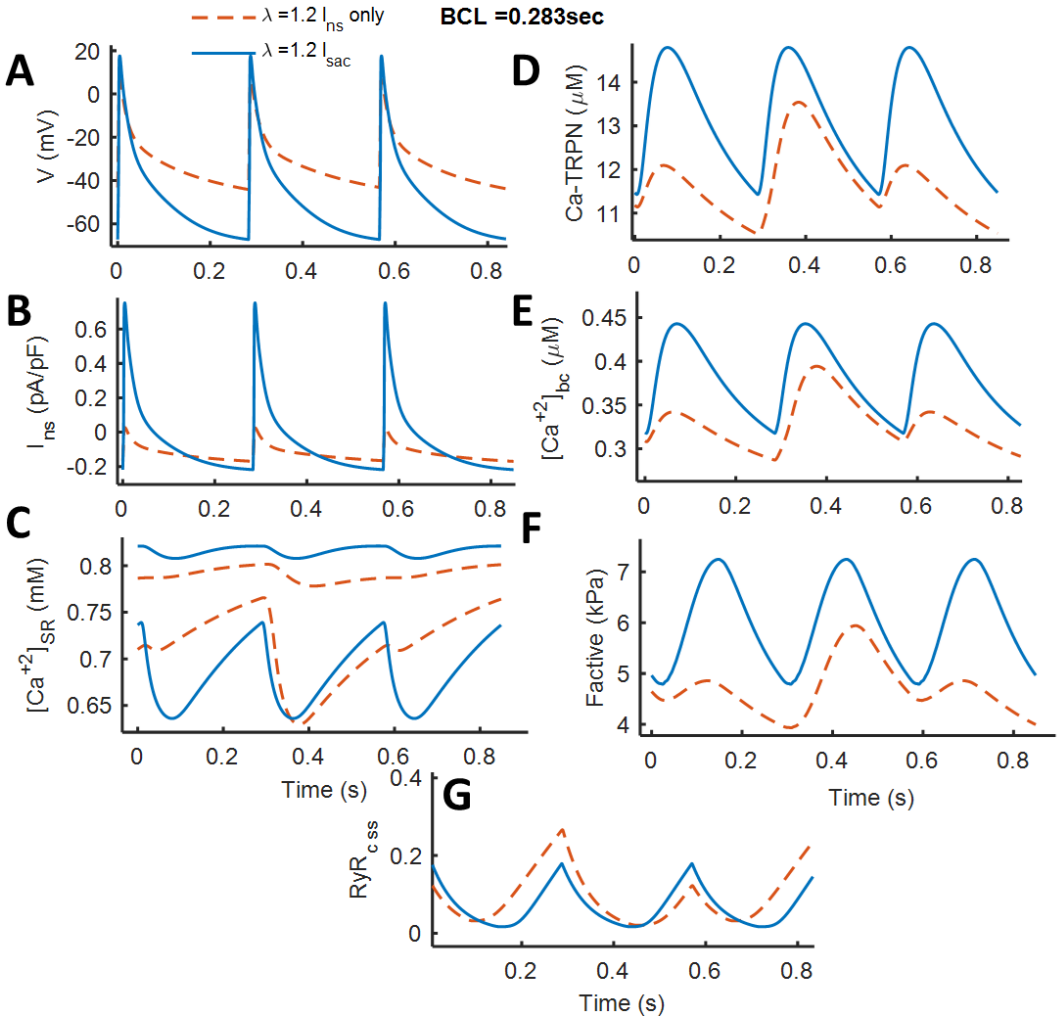

Figure 5.9: Beat-to-beat oscillations appeared at BCL=0.238sec under no preload λ=1 (solid blue lines) and with preload λ=1.2 (dashed red lines) conditions. A) Action potential (AP), B) non-selective cation stretch activated current (I_{ns}), C) SR Ca^{2+} content, D) amount of Ca^{2+} bound to troponin (TRPN), E) Ca^{2+}-transient in subspace ss (large amplitude) vs in bulk cytosol (bc) (small amplitude), F) active force (F_{active}), and G) the steady state inactivation gating variable of RyR_{ss}.

The mechanism behind the stretch induced alternans incidence at BCL 0.283sec (3.5Hz) can be appreciated by Fig. 5.9 under λ=1.2 with I_{sac} (in solid blue line) and with I_{ns} only (in red dashed line). In the basal state of the model, the key mechanism of alternans incidence was the time constant of RyR inactivation gate that determines the availability of the RyRs. Here, since the alternans appeared at 3.5Hz (instead of 4.6Hz as in the basal model) hence resulting into more availability (18%) of RyRs for λ=1 (Fig. 5.9G). On increasing the preload λ=1.2, the recovery from inactivation is not uniform from beat to beat, consequently the availability of RyR gate is alternating between 24% to 11% resulting in short and long CaT respectively (Fig. 5.9E). The stretch induced rise in alternans magnitude can be associated with Ca-TRPN concentration (Fig.

5.9D). As shown before, I_{ns} current increases the binding affinity of Ca^{2+}-TRPN that gets even more enhanced by increasing the preload (Fig. 5.9C). For λ=1.2, for the long beat, the raised diastolic level of Ca^{2+}-TRPN concentration indicates not all the Ca^{2+} is released from the TRPN buffer showing that the sarcomere was not fully relaxed during the diastole. This increased activation of TRPN buffer during the subsequent short beat increases the fraction of bound Ca^{2+}-TRPN that strengthens the cooperative activation of neighboring regulatory units resulting in more strong binding affinity. Thus, an increased Ca^{2+}-TRPN fraction will release small CaT resulting in a relative beat to beat oscillatory mechanism.

5.4 Discussion and Conclusions

In this chapter, we have analyzed the role of stretch level on the characteristics of AP, CaT and F_{active} using a newly developed electromechanically coupled model, MBS2022. The analysis was extended to higher rates to see the stretch induced effect on rate adaptation property of the model and to see its role in alternans development.

Experimental evidence indicates that I_{ns} current plays a role in promoting arrhythmias in intact human atrium (Bode *et al.* 1999), in rat atrial tissue (Tavi *et al.* 1996), and in human atrial myocytes (Kamkin *et al.* 2003). Consistently, at basal frequency of 1Hz, the rise in stretch (for I_{ns} only) lengthens the AP with a depolarized RMP in our model (Fig. 5.5 left panels). In the rat atria, a similar lengthening of APD was demonstrated under the moderate level of stretch applied during the AP diastole (Tavi *et al.* 1998). In contrast, a shortening of APD was also reported in guinea pig atria however, the mechanical stimulus was applied during mid repolarization phase (Nazir & Lab 1996). In experiments, the electrophysiological response to stretch is dependent on timing of the stretch with respect to the AP dynamics. In our model the reversal potential of the I_{ns} current is near the 0mV hence, the model experienced a lengthening effect. The depolarization of RMP resulted in decreased membrane upstroke velocity (dV/dt_{max}) that went even out of the physiological bound for higher stretch conductance (Fig. 5.6). The reduction of cell excitability can be related to the macroscopic mechanism of reduced conduction velocity (CV) for acutely dilated human atrium (Ravelli et al. 2011). By reconstructing atrial CV maps during synchronous atrioventricular node (AV) pacing, Ravelli *et al.* showed that atrial dilation favors conduction heterogeneity in human atrium in form of increased slow conduction spots or the block of intra-atrial conduction sites that occurred mainly in trabecular lateral atrial wall that also confirms the finding of Eijsbouts *et al.* in isolated rabbit hearts (Eijsbouts *et al.* 2003). For higher stretch sensitivity, the model demonstrates a RMP of -63mV (Fig. 5.6 in yellow) that can be related to an increased risk of stretch induced arrhythmia as was found by Kamkin *et al.*, where a correlation between the hypertrophied cardiomyocytes and higher stretch-sensitivity was observed (Kamkin *et al.* 2000). Hence, in hypertrophied myocytes, a smaller mechanical stimulus is required to initiate stretch induced arrhythmia than in healthy hearts.

At basal rate, the varying length elevated the systolic and diastolic levels of the CaT with slight lengthening of the total transient duration. The systolic peak of CaT is highly dependent on the amount of Ca^{2+}-TRPN bound. Increasing length induces small increases in the CaT amplitude and more substantial ones in the amount of Ca^{2+} bound to TRPN. Moreover, the role of individual I_{sac} currents represents that I_{ns} current formulation is more sensitive to verying λ than I_{K0} current

as shown in Fig. 5.5 panel D. In other words, given no rise in CaT peak for I_{K0} current (right panels) for λ=1.3 in purple dot-dashed line, the rise in F_{active} (Fig. 5.5 panel B) is because of increased senisitivty of the thin filament. In contrast, in the presence of I_{ns} current (left panels), the increased CaT peak (for λ=1.2 in yellow dotted line) along with increased affinity of Ca-TRPN bound (Fig. 5.5 panel C) combines to elevate F_{active} (Fig. 5.5 panel B). This result is consistent with experiments by Tavi *et al.* in rat atrial myocytes (Tavi *et al.* 1998) highlighting Ca^{2+} systolic rise and Ca^{2+} buffering by TRPN as the major modulators of contractile force. The enhanced sensitivity of Ca^{2+}-TRPN binding can be explained by the length-dependent increase of contraction (Lookin & Protsenko 2019). The study relates the extent of length dependent activation with both peak systolic CaT and its decaying kinetics.

In our model (based on the RDQ one), as in experiments, the EC_{50} value of force-pCa curve is a linear inverse function of increasing sarcomere length while varying the l_{CE} within the physiological range. Hence, the length dependent decrease in EC_{50} (or increased sensitivity of Ca^{2+} binding to TRPN) results in increased bound Ca^{2+} in the cytosol in spite of quite similar levels of free Ca^{2+}. This length-dependent rise in Ca^{2+} bound to TRPN is further amplified once translated into active force (Fig. 5.4). The model was also able to predict the secondary effects of MEF. First, the decrease of I_{CaL} current in both peak and plateau phases (not shown). The increasing calcium dependent inactivation (CDI) effect, because of increasing J_{relss} peak (not shown), is the main modulator of I_{CaL} inactivation with stretch. On the other hand, Na^{+} accumulation due to stretch increased the inward I_{NaCa} current at basal rate (Fig. 5.7C). Summing up all together, under increasing stretch, increased inward I_{sac}, reduced I_{CaL} and increased I_{NaCa} inward current resulted in the lengthening of APD_{90}.

In conclusion, the stretch can modulate the electrophysiological characteristics owing to the presence of I_{sac} currents. The electrophysiological response to stretch is dependent on timing of the stretch with respect to the AP dynamics. Our model demonstrated a depolarization of RMP with increasing level of stretch that evantually led to reduced cell excitability. For higher rates, the stretch contributes to the increased alternans incidence with higher magnitude and also shifting of alternans incidence threshold to lower frequency. The major mechanism behind this vulnerablity was slow Ca-cycling in the model associated with increasing level of stretch.

Chapter 6

Therapeutic Potential of I_{Kur} channel blockers: Inotropic response in Anti-arrhythmic Treatment

The content of this chapter is re-produced from:

"Automatic Optimization of an in-silico Human Atrial Electromechanical Model and Inotropic Effects in Anti-arrhythmic Treatment."

***Fazeelat Mazhar**, Chiara Bartolucci, Michelangelo Paci, Cristiana Corsi and Stefano Severi.*

Manuscript in preparation phase.

Abstract

Electro-mechanical (EM) coupling is the tight integration of complex regulatory mechanism where it becomes difficult to quantify the role of individual parameters. With the advancement of technology and computational power, cardiac modeling and simulation have become complementary tools to provide complete control of parameters over the integrated system. In this chapter, we aim to optimize and validate the developed human atrial EM cell level model, MBS2022, that captures improvement in the experimental indices while preserving the simplified yet detailed Ca^{2+}-wave like diffusion towards the center, presented in the original work. The parameters related to Ca^{2+}-handling were optimized, and the results were quantified using biomarkers related to Ca^{2+}-transient and contractility. As a result of optimization, SERCA uptake became quite powerful as the flux magnitude was increased by 182%. The therapeutic potential of the model was evaluated by analyzing the anti-arrhythmic effect of atrial-specific I_{Kur} current block. Hence, the model was used to analyze: 1) its effect on action potential (AP) repolarization using a low concentration of I_{Kur}-specific and less specific blockers; 2) drug concentration dependent inotropic response and 3) its effect on rate adaptation of APD. The I_{Kur} selective blockers (4-AP 5 µM) result into a more pronounced plateau than the less selective ones (AVE0118 (10 µM), Acacetin (10 µM)) that results in 57% enhancement of contractility that can be suitable as a treatment for atrial contractile dysfunction arising due to atrial tachyarrhythmias. The reversing of rate dependent shortening effect of APD by I_{Kur} block (Acacetin (10µM)) was because of loss of rate dependent Na^{+} accumulation hence, predicting its potential to disrupt reentrants and to prevent AF recurrence, especially at higher pacing rates by the prolongation of the effective refractory period.

6.1 Introduction

The heart dynamically interlinks numerous physiological processes in a well-orchestrated manner, while simultaneously adapting the varying mechanical conditions. This intrinsic mechanism of 'mechano-electric regulations' is based on feedback and feedforward pathways between the electrical and mechanical activity of the heart (Quinn *et al.* 2021). Due to the complex regulatory mechanisms involved in a tightly integrated system, it becomes experimentally challenging to quantify the role of individual components.

Computational modeling is a powerful tool that provides complete control of parameters along with the visibility of all the individual components of the integrated system (Niederer *et al.* 2019, Trayanova *et al.* 2011). The advancement of computational power has made it possible to simulate the models in a short timeframe, providing the possibility of the increased predictive power of the integrated system. Motivated by this, a better fit of AP and Ca^{2+} transient characteristics to the experimental ranges could be achieved through automatic optimization techniques (Fabbri *et al.* 2017). In literature, many such attempts were made to optimize *in-silico* models for human iPSC derived CMs (Paci *et al.* 2018a, 2018b), for EM coupling of human ventricular CMs (Bartolucci *et al.* 2022) and to better predict the drug action response (Paci *et al.* 2020).

Recently, we have proposed an electro-mechanical model for human atrial CMs (Mazhar *et al.* 2022) namely MBS2022 (*Mazhar-Bartolucci-Severi 2022*). The model encompasses a detailed Ca^{2+}-handling representation adapted from its parent model Koivumäki 2011 (Koivumäki *et al.* 2011) and its integration with a recently developed contraction model by Quarteroni group (Regazzoni *et al.* 2020). The model provides a physiological CaT followed by a physiological twitch having dynamics in agreement with human atrial experimental data range. The model simulates the isometric and iso-sarcometric twitches and highlights the possible role of MEF towards the initiation of atrial arrhythmias by varying stretch levels and sensitivity. However, one of the limitations highlighted was the slow uptake dynamics of the sarcoplasmic reticulum (SR) that makes the Ca^{2+} transient decay slower in the later phase and eventually slowing the twitch relaxation.

In this work, we propose an update in MBS2022 model by fine tuning of a set of model parameters based on an automatic optimization technique. The experimental data used for the optimization was mainly adopted from our previous work (Mazhar *et al.* 2022) with the addition of validation data on atrial specific ultra-rapid delayed rectifier potassium current (I_{Kur}) block. The automatic optimization of MBS2022 mainly affected the SERCA activity of the bulk cytosol (*bc)*, RyR adaptation, and the RyR dependence on SR Ca^{2+} content (RyR SR_{Ca}). Based on this update of the model, we aim to validate the model by analyzing its therapeutic potential through the application of anti-arrhythmic drug (I_{Kur} block) effect on repolarization and contractility.

6.2 Methods

6.2.1 *In-vitro* data

6.2.1.1 Calibration data

For the calibration of MBS2022, we have used biomarkers of Ca^{2+} transient (CaT) and active force (F_{active}) recorded from human atrial CMs (Table 2.1 in Chapter 2). Similarly, biomarkers for AP extracted from human atria were obtained from references in Table 3.3 (Chapter 3). Biomarkers for F_{active} are the time to peak ($ttp_{Factive}$), relaxation time at 50% and 90% of peak ($rt_{50Factive}$ and $rt_{90Factive}$ respectively), and twitch time $TT_{Factive}$. Similarly, CaT biomarkers are the time to peak (ttp_{CaT}), relaxation time at 50% of peak (rt_{50CaT}), and time duration (TT_{CaT}). AP biomarkers are action potential durations at 30%, 50% and 90% of repolarization (APD_{30}, APD_{50} and APD_{90} respectively), amplitude of the upstroke (V_{amp}), resting membrane potential (V_{diast}) and maximum upstroke velocity (dV/dt_{max}). Using this definition, we have computed the biomarkers for MBS2022 original and optimized output. Using the simulation biomarkers, we have made a comparison with experimentally measured values and their data range at the basal frequency of 1Hz as listed in Table A4. A more detailed analysis will be presented later in Section 6.3.1 'Optimized Biomarkers of model'. Among these biomarkers, few are extended for the physiological range of frequencies [0.5 1 2 3 Hz] like percentage change of APD_{90} ($\%\Delta APD_{90}$), of CaT_{max} ($\%\Delta CaT_{max}$), of F_{active} ($\%\Delta F_{active\,max}$), and of SR Ca^{2+} contents ($\%\Delta[Ca^{2+}]_{SR}$) with respect to 1Hz basal frequency (references in Table A3). Using the same definition, we computed the *in-silico* biomarkers in comparison to experimental nominal values with their lower and upper bounds as shown in Table A4 & A5.

6.2.1.2 Validation data

For validation, we simulated the test for I_{Kur} block that was divided into three parts as follows: 1) antiarrhythmic effect of I_{Kur} selective and less selective blockers at basal frequency (Li *et al.* 2008, Wettwer *et al.* 2004, Christ *et al.* 2008), 2) effect of I_{Kur} block concentration dependent response on AP and F_{active} biomarkers (Li *et al.* 2008, Schotten *et al.* 2007), and 3) effect of I_{Kur} block on AP rate adaptation (Li *et al.* 2008). The experimental data used for validation tests are listed in Table 6.1.

Table 6.1: Human atrial *in-vitro* data used for validation test of I_{Kur} current block. The table demonstrates the variety of blockers along with their concentrations used for each study. Biomarkers used for each experiment are AP at 20%, 50%, 75% and 90% of repolarization (APD_{20}, APD_{50}, APD_{75}, APD_{90}), plateau potential (PP), diastolic membrane potential (V_{diast}), effective refractory period (ERP), and $F_{active\ peak}$. Among the biomarkers obtained for basal frequency, few are reported for rate adaptation in form of percentage change with respect to control. The equivalent percentage of relevant current block is also shown.

Sr. No.	**References**	**Drug & concentration**	**Biomarkers**		**Current block**
			1Hz	[0.5 1 2 3] Hz	
1.	Wettwer *et al.* 2004	4-AP (5 µM)	APD_{20}, APD_{90}, PP		I_{Kur}: 80%
		4-AP (25uM) + E-4031 (1uM)	APD_{90}, PP		I_{Kur}: 90% + I_{Kr}: 95%
2.	Schotten *et al.* 2007	AVE0118 ([10 100] µM)	$F_{active\ peak}$		I_{Kur} [12 32 68 90 97] % (Decher et al. 2006)
3.	Christ *et al.* 2008	AVE0118 (10 µM)	APD_{20}, APD_{90}, V_{diast}, ERP		I_{Kur}: 67%, I_{to}: 38%
4.	Li *et al.* 2008	Acacetin ([5 10] µM)	APD_{50}, APD_{75}, APD_{90}		I_{Kur}: 62.5%, I_{to}: 30%, I_{Kur}: 75%, I_{to}: 50%
		Acacetin (10 µM)		%Δ APD_{50}, %Δ APD_{75}, %Δ APD_{90}	I_{Kur}: 75%, I_{to}: 50%

6.2.2 Electro-mechanical model, *MBS2022*

MBS2022 is an EM coupled model where coupling was achieved with two modules: the AP module obtained from a considerable level of modifications in the human atrial cell model Koivumäki 2011 (Koivumäki *et al.* 2011) (KM2011); and a mean-field approximation-based contraction module (Regazzoni *et al.* 2020) (RDQ2020). The detailed description of MBS2022 can be found in Chapter 3. Briefly, the model has a two compartmental setup for cytosol i.e., the sub-space (*ss*) and the bulk cytosol (*bc*) as illustrated by the schematic diagram of MBS2022 model in Figure 3.2. The subspace is near the membrane enclosing all the ionic currents, in particular, the stretch activated current, i.e. I_{sac}. The central part of the cytosol (enclosed inside the dashed rectangle) is the *bc* compartment that contains the buffers, i.e. calmodulin (CMDN) and troponin (TRPN). Apart from this, the SR is also localized near the center, and it contains two compartments as cytosol SR_{ss} and SR_{bc} with their own release (RyR) and uptake (SERCA) units. Since the model lacks t-tubules structure therefore, $[Ca^{2+}]_{SR}$ release is the major source of spatial spread of the Ca^{2+}

signal other than diffusion. The rise in Ca^{2+} level in the bulk binds to TRPN and initiates the contraction, and then unbinds back to its diastolic level that ensures TRPN is now in relaxed or in stretched state. Hence, MBS2022 model is a simplified version of its parent AP model and is capable enough to preserve the characteristics of centripetal Ca^{2+} diffusion and can simulate both MEF (AP by I_{sac}) and MCF (Ca^{2+}-TRPN binding) effects quantitatively.

6.2.3 Optimization of MBS2022 model

6.2.3.1 Step 1: Automatic optimization

The optimization of MBS2022 was carried out using a genetic function (Matlab function *gamultiobj).* Hence, the cost function used for the optimization was a multi-objective genetic algorithm as defined by Paci et al. (Paci *et al.* 2018). The parameters used for the optimization were related to Ca^{2+}-handling (as shown in Table A6): 1) the SERCA activity, expression level and pumping rate for *bc* compartment only, 2) RyR adaptation gate half activation Ca^{2+} concentration and its adaptation maximum and minimum levels for both compartments, 3) RyR activation based on SR_{Ca} half activation and slope for both compartments, and 4) RyR inactivation gate recovery time for both compartments. The contraction related parameters were already optimized (as was described in Section 3.2.6) therefore, are not included in the optimization process for this chapter. We defined objective function based on AP, CaT and F_{active} biomarkers for all rates to minimize a linear cost function *c*,

$$c = \sum_{1}^{N_{biomarkers}} w_i * c_i$$

$$c_i = \frac{(b_{i,sim} < LB_i)(b_{i,sim} - LB_i)^2 + (b_{i,sim} > UB_i)(b_{i,sim} - UB_i)^2}{0.5\,(LB_i + UB_i)}$$

where $b_{i,sim}$ is the *i*th simulated biomarker, LB_i and UB_i is the *i*th lower and upper bound of the experimental data for $b_{i,sim}$, $N_{biomarkers}$ is the total number of biomarkers that were considered during the optimization;for our model the count was 26 i.e. AP (6), CaT (3) and F_{active} (5) for basal rate and $\%\Delta APD_{90}$ (3), $\%\Delta CaT_{max}$ (3), $\%\Delta[Ca^{2+}]_{SR}$ (3), $\%\Delta F_{active\ max}$ (3) for rest of the physiological range of frequencies. The cost of each biomarker was computed as a squared distance between simulated and experimental biomarkers; with the condition that simulated biomarker is out of lower or upper bound; normalized by the center of the mass of $[LB_i + UB_i]$.

The parameter values obtained by the automatic optimization step are compared with the original values in Figure 6.1 using markers: MBS2022 original values are shown by open circles, lower and upper bounds by asterisks, and automatic optimization by triangles. Because of automatic optimization (step 1), the SERCA activity is accelerated in the *bc* compartment since both the SERCA expression levels ($[SERCA]_{bc}$) (first panel on the top) and pumping rate (k_{4bc}) (middle panel on the top) have moved close to their upper bounds. For RyR adaptation levels, the optimized parameters defining maximum (RyR_{a1}) and minimum (RyR_{a2}) levels have increased for both *bc* and *ss* compartments as shown in Figure 6.1 top right panel. Notably, because of the increase in RyR_{a1ss}, the parameter value is now overlapping with the upper bound. A slight reduction in half activation value of both compartments is observed resulting in a more sensitive

RyR adaptation (top right panel). The recovery from inactivation time constant for RyR inactivation gate has slightly lengthened for *ss* and remained the same for *bc* as compared to the original values (bottom left panel). For the optimized RyR SR_{Ca} gate, the *bc* compartment is more $[Ca^{2+}]_{SR}$ sensitive and the relation is less stepper than the *ss* (bottom right panel).

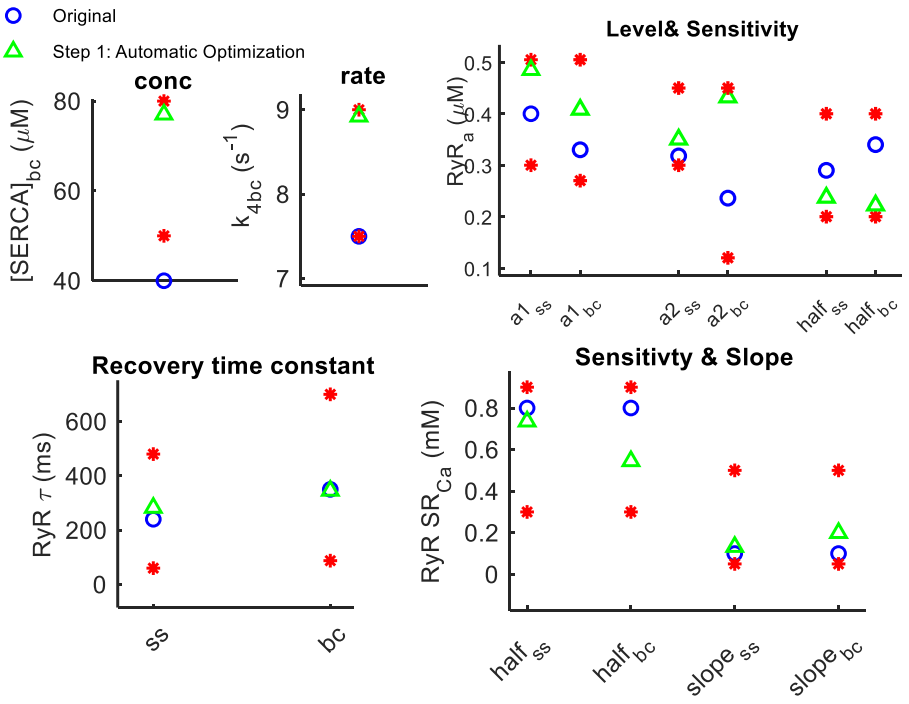

Figure 6.1: Parameter set optimized for MBS2022. The step 1 of optimization, the automatic (triangles) values of parameters are compared with original MBS2022 values (open circles) and their lower and upper bounds (asterisks). Top panels (left and middle) are relevant to SERCA activity of the *bc* compartment, SERCA concentration ($[SERCA]_{bc}$) and the pump rate (k4bc) respectively. Top right panel represents RyR adaptation gate maximum (RyR_{a1}), minimum (RyR_{a2}) levels and their half activation value ($RyR_{a\,half}$). Bottom left panel shows recover from inactivation time constant (τ) for RyR inactivation gate in each compartment. Bottom right panel represents the RyR opening gate based on SR Ca^{2+} content (RyR SRCa) and its half activation value along with slope for both compartments.

The automatic optimization results have ensured that the centripetal Ca^{2+} diffusion phenomena of the AP module is not compromised. This Ca^{2+}-wave like diffusion towards the center was retained by the optimized model as shown in Figure 6.2A. In comparison to the model output, the transverse confocal line scan image and derived local CaTs for rabbit atrial CMs were shown in B panel where a delay in the arrival of peak for the central CaT can be observed. In addition, the Ca^{2+} handling also demonstrated this heterogenous distribution of CaT, i.e. the Ca^{2+} release in the *ss* is still faster, larger in magnitude, and occurs before the *bc* whereas the uptake is slower and smaller in *ss* than *bc* as shown in Figure 6.2. The optimized model is characterized by differences in RyR adaptation and RyR SR_{Ca} gating behavior for the two compartments. The optimized RyR SRCa gate demonstrates a steeper and right shifted (less $[Ca^{2+}]_{SR}$ sensitive) relation for *ss* then *bc* (Figure 6.2E). In addition, the RyR adaptation for *bc* begins for lower Ca^{2+} levels and slightly higher saturation level then *ss* (Figure 6.2F).

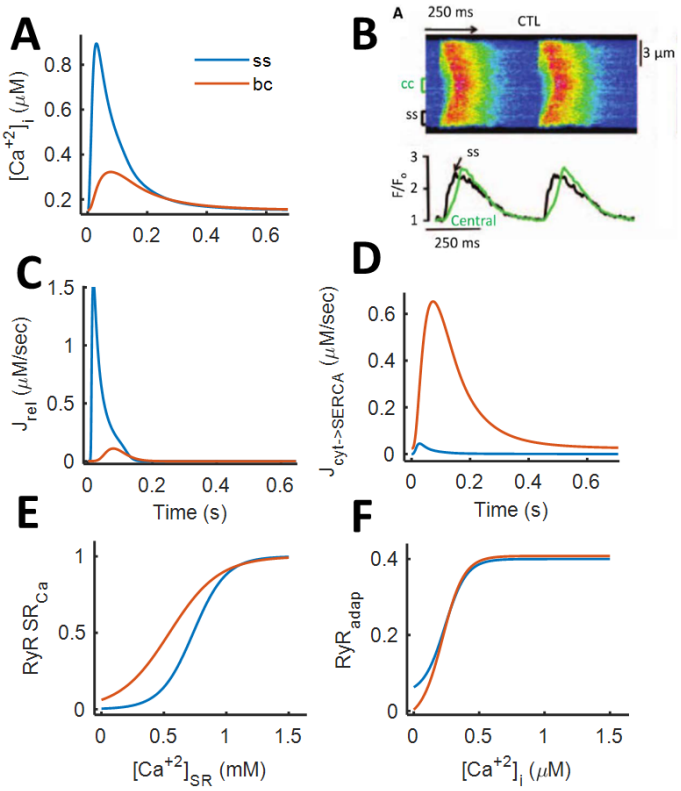

Figure 6.2: Effect of optimization on CaT and Ca^{2+} handling in *ss* (in blue) and *bc* (in red) compartments at basal frequency of 1Hz. (A) CaT in both compartments, reduced and delayed peak of CaT in *bc* than *ss* B) Transverse confocal line scan and derived local CaTs for rabbit atrial cardiomyocytes adopted from (Greiser *et al.* 2014), C) release flux (J_{rel}), (D) uptake flux from cytosol to SERCA ($J_{cyt->SERCA}$); and model characteristics (E) RyR activation based on SR Ca^{2+} content, and F) RyR adaptation (RyR_a) based on $[Ca^{2+}]_i$ both compartments.

6.2.3.2 Step 2: Manual Tuning

At a high rate of 4.2Hz (not included in optimization), we observed an irregular AP and so the CaT waveforms. On further investigation, we determined that irregular $[Ca^{2+}]_{SR}$ release in the *ss* by the RyR activation gate was the major cause of this behavior. In addition, at higher frequency the adaptation gate was already saturated, and it dragged the half activation value of the gate to higher Ca^{2+} levels resulting in an irregular opening of the gate. Hence, we restored the RyR_{a1} back to its original value (0.48 to 0.4) to get rid of this non-uniformity. We chose to have consistent SERCA activity parameters in both compartments. Since, SERCA *ss* has a small flux (Figure 6.2D) and has the least contribution in Ca^{2+}-handling, therefore was not the part of optimization parameters list. Thus, after having optimized parameters for SERCA activity for *bc* compartment, we reused both parameter values for SERCA *ss* too. The rest of all the parameters of the model were the same as was defined in MBS2022.

6.3 Results

6.3.1 Optimized biomarkers of model

The overall effect of optimization on the original MBS2022 model was quantified by comparing the optimized biomarkers after each step with the original model output and

experimental data as shown in Figure 6.3. The biomarkers are represented using various marker labels like original model (open circles), optimized model (triangles), and experimental data: mean values (open squares) and their range (asterisks). The AP biomarker, APD_{90} (Figure 6.3A) demonstrates a shortening after the optimization and is within the defined data bound range even quite near to the mean data value. After the optimization, a shortening effect in APD_{50} (B) and APD_{30} (C) values is observed from the original model biomarkers and APD_{30} is now overlapping on the mean data value. Similarly, the optimized biomarker representing V_{amp} (D) is larger, and dV/dt_{max} (F) is slower whereas V_{diast} (E) is quite comparable to the original model biomarkers. The optimized CaT in the *bc* compartment demonstrates a shortening of ttp_{CaT} (H) and rt_{50CaT} (G) and are out of data bounds but ttp_{CaT} is not too far from the data range. The TT_{CaT} (I), which was too slow for the original model, is now within the data range and even overlapping with the mean data value. The biomarker related to $F_{active\ peak}$ (J) demonstrates a reduced amplitude, overlapping on lower data bound. The optimized $ttp_{Factive}$ (K) is quite close to the mean data value. The optimized relaxation biomarkers are in good agreement with the experimental bounds, like $rt_{50Factive}$ (L) is now within the data range, $rt_{90Factive}$ (M) and $TT_{Factive}$ (N) are quite closer to the upper data bound. A tradeoff between rt_{50CaT} and $rt_{50Factive}$ biomarkers can be seen where one goes out of data bound while fixing the other within the range. In the optimized model, we relied more on F_{active} data limits since it was computed from a good number of data collection whereas, the data for CaT was quite sparse.

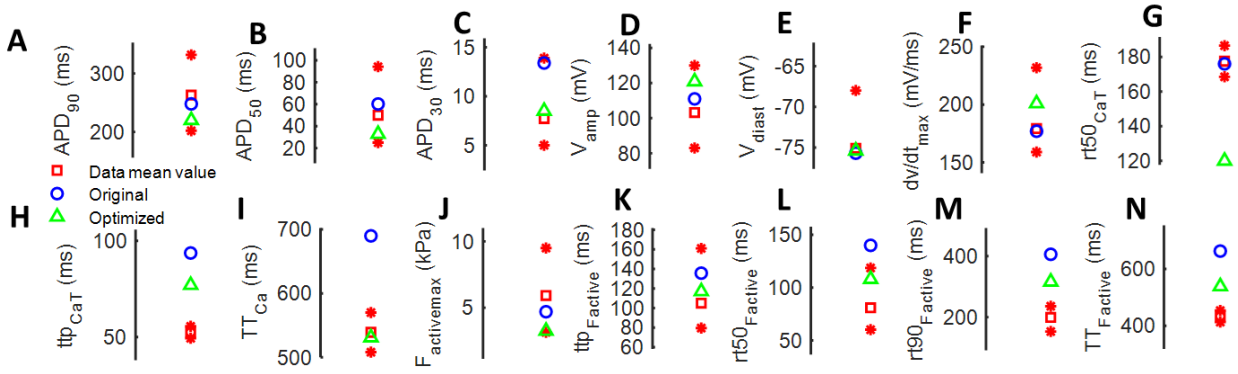

Figure 6.3: Comparison of biomarkers from model output; original (open circles), optimization (triangles), with experimental data range (asterisks) and mean value (open squares). AP biomarkers are related to time; APD_{90} (A), APD_{50} (B) and APD_{30} (C); voltage amplitude (V_{amp}) (D), diastolic potential (V_{diast}) (E); and maximal velocity (dv/dt_{max}) (F). Biomarkers related to CaT in the bulk cytosol are: rt_{50CaT} (G), ttp_{CaT} (H) and TT_{CaT} (I). F_{active} biomarkers are related to peak value $F_{active\ max}$ (J); and time: $ttp_{Factive}$ (K), $rt_{50Factive}$ (L), $rt_{90Factive}$ (M) and $TT_{Factive}$ (N).

6.3.2 Optimized model characteristics

Given the optimized MBS2022 model, we demonstrated the characteristics of AP, CaT and F_{active} in comparison to the original model for basal frequency of 1Hz as shown in Figure 6.4. The AP (Figure 6.4A) for the optimized model has type-3 morphology (Dawodu *et al.* 1996) (as the original model) and a slightly short late repolarization phase. The Ca^{2+} in SR is shown in Figure 6.4B where the release is smaller and slightly delayed in *bc* compartment (in red) then *ss* (in blue) whereas, the uptake is faster than *ss*. In comparison to the original model (not shown), the SR Ca^{2+}

content in *bc* is reduced from 0.62 to 0.52mM with an increase in release magnitude. The optimized CaT in the *ss* has a faster decay with no slight increase in the peak value in comparison to the original output (Figure 6.4C). The optimized CaT in the *bc* (Figure 6.4D) has a reduced systolic and diastolic level resulting in a reduced amplitude from 0.2 to 0.168 µM. Less concentration of CaT_{bc} is bound to TRPN buffer with slightly faster decay (Figure 6.4E) in optimized model output in-line with reduced and fast CaT in the *bc*. The resulting force of Ca^{2+} bound to TRPN, F_{active} has been shifted upward, i.e. raised diastolic level with a more pronounced systolic peak as shown in Figure 6.4F. As stated earlier, the elevated level and fast uptake flux for *bc* compartment, one of the major consequences of optimization, is compared with the original model in Figure 6.4I.

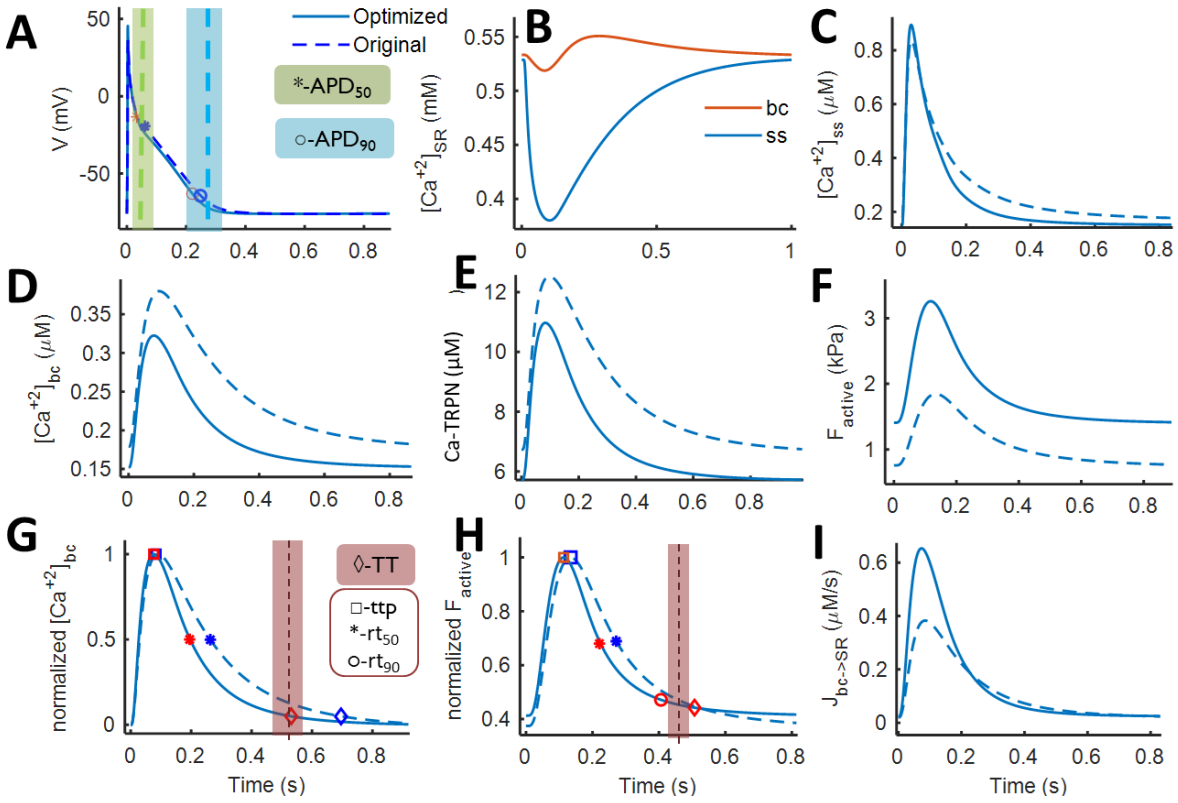

Figure 6.4: Comparison of optimized model characteristics with original AP, CaT and F_{active} at basal frequency of 1Hz. The model biomarkers are compared for the optimized results (in red) with original values (in blue) along with their experimental ranges (shaded regions) as listed in Table 1. Biomarkers are represented using marker labels like ttp_{Ca} or $ttp_{Factive}$ with open squares, APD_{50} or rt_{50Ca} or $rt_{50Factive}$ with asterisks, APD_{90} or $rt_{90Factive}$ with open circles, and TT_{Ca} or $TT_{Factive}$ with diamonds. The color for each shaded area corresponds to the data range of a biomarker as also reported in Table A4. A) Comparison of AP traces for optimized output (solid line) with MBS2022 (dashed line) and with experimental APD_{50} and APD_{90}, B) Ca^{2+} concentration inside the SR obtained after optimization for both *ss* (in blue) and *bc* (in red) sub compartments, C) Comparison of optimized Ca^{2+} transients for *ss*, and for D) *bc* with MBS2022 output, comparison of E) optimized concentration of Ca^{2+} bound to TRPN F) and the F_{active} generated with the original output and, G) normalized Ca^{2+} transient and H) normalized F_{active} compared with optimized and original model biomarkers (ttp_{CaT} and $ttp_{Factive}$, $rt50_{CaT}$ and $rt50_{Factive}$, $rt90_{Factive}$ and TT_{CaT} and $TT_{Factive}$) and experimental data range for TT_{Ca} and $TT_{Factive}$ only, and I) Ca^{2+} uptake flux from *bc* to SERCA SR ($J_{bc->SR}$) are compared for MBS2022 and the optimized output.

A quantitative comparison of model output AP, F_{active} and CaT characteristics using biomarkers measured from MBS2022 original and optimized version was shown in Figure 6.4. For AP, both APD_{50} (asterisk) and APD_{90} (open circle) are shifted slightly upward showing

increased upstroke amplitude of the optimized AP (Figure 6.4A). The normalized CaT in *bc* compartment (Figure 6.4G) compares the biomarkers for optimized (in red) with original model (in blue). Hence, a comparable ttp (open square), a shortened rt_{50} (asterisk) and a shortened TT (diamond) can be seen for optimized model. Notably, the optimized model TT biomarker is now within the data range, overlapping on the mean data value (dashed line). The normalized F_{active} plot (Figure 6.4H) shows that $ttp_{Factive}$ is slightly shortened, all the relaxation time related biomarkers, $rt_{50Factive}$, $rt_{90Factive}$ and the $TT_{Factive}$ are shortened for the optimized model. Moreover, the optimized $TT_{Factive}$ is now quite near the upper bound of the experimental data range in comparison to the original model $TT_{Factive}$.

6.3.3 Positive inotropic effect of anti-arrhythmic treatment: I_{Kur} block

The principal approach for suppressing the occurrence of atrial fibrillation (AF) is the application of antiarrhythmic drug therapy. The I_{Kur} current is considered an atrial-selective target for antiarrhythmic drugs since it contributes only to atrial repolarization with no effect on ventricular AP (Ravens *et al.* 2011). Thus, I_{Kur} channel blockage prolongs the effective refractory period with no chance of inducing ventricular arrhythmias (like long QT syndrome) (Ravens *et al.* 2017).

Given the antiarrhythmic effect of I_{Kur} block, we performed a validation test by blocking I_{Kur} current and analyzing its response on the optimized electrophysiology and contractility. Hence, we designed the validation test as follows: 1) antiarrhythmic effect of I_{Kur} selective and less selective blockers at basal frequency of 1Hz and its effect on AP biomarkers data (Li *et al.* 2008, Wettwer *et al.* 2004, Christ *et al.* 2008), 2) effect of I_{Kur} block concentration dependent response on AP and F_{active} biomarkers (Li *et al.* 2008, Schotten *et al.* 2007), and 3) effect of I_{Kur} block on AP rate adaptation (Li *et al.* 2008). The experimental data used for these validation tests are listed in Table 6.1.

6.3.3.1 Effect on electrophysiology at basal frequency

The characteristic changes in AP parameters were observed with I_{Kur} selective, 4-AP (Wettwer *et al.* 2004) and less selective current blockers, Acacetin (Li *et al.* 2008), and AVE0118 (Christ *et al.* 2008) at basal frequency of 1Hz. The effect of I_{Kur} block on the AP is shown in Figure 6.5A where the control AP (in blue) is transformed from type-3 to type 1 AP morphology (spike and dome) in presence of 4-AP (in yellow dot-dashed lines) whereas, the AP is converted to type-4 (more triangular) for less selective drugs, i.e. AVE0118 (in red dashed line) & Acacetin (in purple dotted line). The equivalent amount of current blocked for the simulation, depending upon each drug and its concentration is listed in Table 6.1. In the presence of less selective blockers (AVE0118 (10µM) and Acacetin (10µM)), the lengthening of early repolarization phase was more pronounced (Figure 6.5A). This can be quantified by the plateau potential (PP) magnitude (Figure 6.5C) computed as average voltage in the time window of 20 to 80ms after the upstroke. The shift from negative potential (under control) to positive value can be appreciated more in the presence of AVE0118 (10 µM) (10.37mV) and Acacetin (10 µM) (18mV not shown) then to 4-AP response (8.3mV), that meets qualitatively with the experimental data response (Christ *et al.* 2008, Wettwer *et al.* 2004). The early repolarization phase response to I_{Kur} block can also be quantified using APD_{20} as shown in Figure 6.5D where the model showed a percentage rise of APD_{20} in good

consideration with the reported data under AVE0118 (10 µM) (model output vs data: 435 vs 370%) and 4-AP (5 µM) (160 vs 151%). In the presence of Acacetin (10 µM), the model demonstrated a prominent rise in APD_{50} than APD_{75} (560 vs 214%) percentage increase that meets qualitatively the experimental data biomarker (Li *et al.* 2008) trend (285 vs 125%). The late repolarization phase is computed using APD_{90} that shows a lengthening response for the model under all the three blockers whereas, the data demonstrated some discrepancy, i.e. a slight shortening under AVE0118 and 4-AP and a lengthening under acacetin blockers. This discrepancy of APD_{90} response to I_{Kur} block will be detailed in the Discussion section.

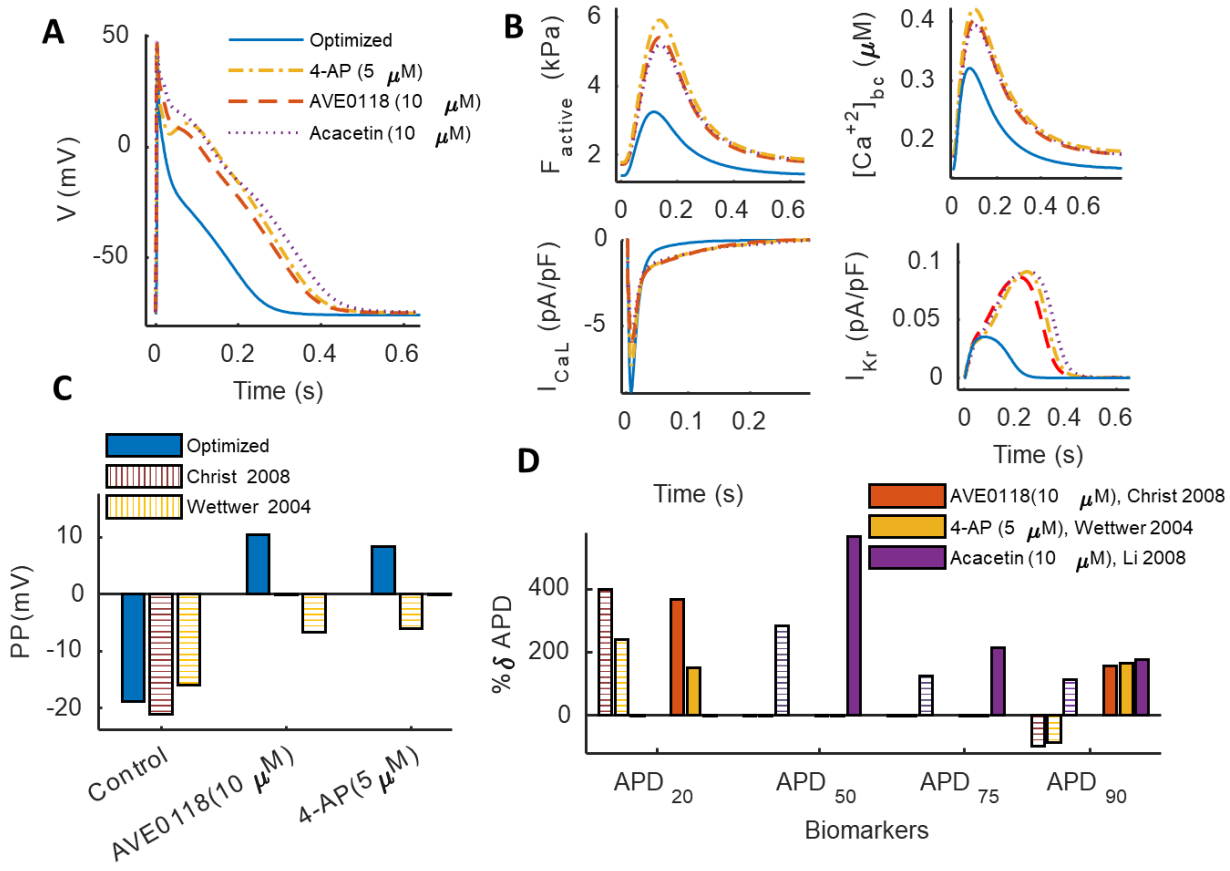

Figure 6.5: Effect of I_{Kur} specific, 4-AP (5 µM) and less specific blockers, AVE0118 (10 µM), and Acacetin (10 µM) on the model repolarization. A) AP for control (in blue solid line) in comparison to 4-AP (in yellow dot-dashed line), AVE0118 (in red dashed line) and Acacetin (in purple dotted line), B) the secondary effect of I_{Kur} block on contractility (F_{active}), CaT_{bc}, I_{CaL} and I_{Kr} ionic currents under all the three drugs and control condition. C) Effect of I_{Kur} block on plateau potential (PP), D) Percentage change in APD_{20}, APD_{50}, APD_{75} and APD_{90} for model output (solid filled bars) in comparison to the experimental data (pattern filled bars) reported in Table 6.1.

The model demonstrated secondary response of I_{Kur} block as shown in Figure 6.5B. The inotropic response of I_{Kur} block is shown by F_{active} plot (top left panel) where the elevation of systolic peak is higher in I_{Kur}-selective blockers than the less selective ones whereas, the diastolic rise is similar for all. Along the same lines, a parallel rise in CaT_{bc} (top right panel) is observed by the model output where the peak value is more appreciated under I_{Kur} specific current blocker. The ionic currents demonstrate a secondary effect, and the major ones are the increased plateau of I_{CaL}

current (bottom left panel), and a rise in I_{Kr} current (bottom right panel). This mechanism behind the I_{Kur} block effect on repolarization will be discussed in detail in the coming section.

6.3.3.2 Concentration dependent effect of I_{Kur} block

The effect of I_{Kur} block on the plateau of AP is concentration dependent hence providing a concentration dependent positive inotropic effect as shown in Figure 6.6. The I_{Kur} less specific blocker, AVE0118 (10µM) increased the F_{active} force in the model by 40%, that is quite inline with 55.4% rise in the experiment by Schotten (Schotten et al. 2007). The concentration dependent positive inotropic effect is achieved by the model as shown in Figure 6.6B where the F_{active} increases up to 10µM concentration of the drug and then saturates for higher concentrations. The inotropic effect is due to the change induced in the AP morphology because of I_{Kur}/I_{to} currents block and a secondary rise in I_{CaL}, and I_{NaCa} reverse mode activity where $I_{NaCa\ outward} > I_{NaCa\ inward}$. This is depicted by the integral of I_{CaL} (in blue) and I_{NaCa} (in red) over the whole-time course for all the concentrations of AVE0118 blocker as shown in Figure 6.6D. Clearly, the integral of I_{NaCa} (in red) shows no dependency on increasing concentration of AVE0118 (upto 10µM), however at 31 µM it gets reduced (being less negative) and eventually restores back to its value at 100 µM. Meanwhile, a sharp increase in I_{CaL} integral for low concentration of AVE0118 (upto 3µM) can be observed and then the current gets saturated. Hence, for very low concentration of AVE0118 (upto 3µM), I_{CaL} is the major source of sharp rise in contractility whereas, for higher concentrations (10 to 100µM) the biphasic response of I_{NaCa} is dominant.

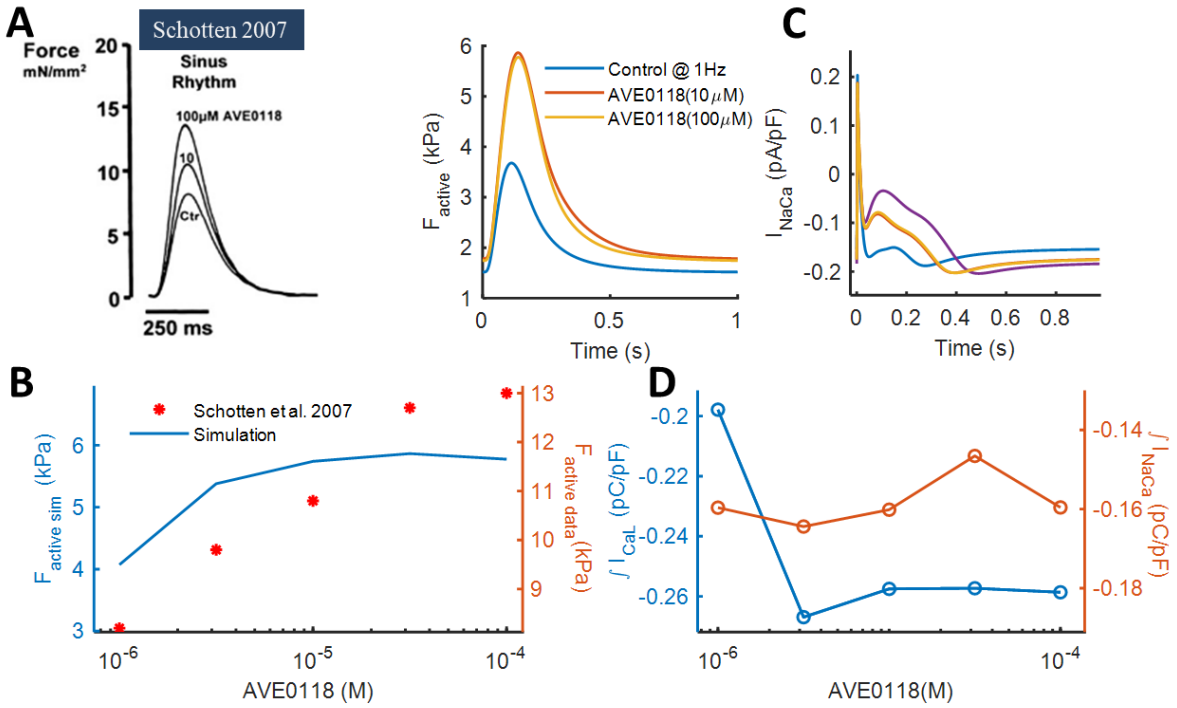

Figure 6.6: Effect of AVE0118 on contractility of optimized model in comparison to human atrial trabeculae data (A on left) (Schotten *et al.* 2007). A) (on right) Compares the F_{active} for control (in blue), AE0118 10 µM (in red) and 100 µM (in yellow), B) shows the simulation results (in blue) of concentration dependent effect on contractility with experimental data (in red asterisks),

C) The secondary role of exchanger current and the mechanism explained by superimposing integrals of I_{CaL} (in blue) and I_{NaCa} (in red) currents.

6.3.3.3 Effect of I_{Kur} block on rate adaptation

Like any conventional antiarrhythmic drug, I_{Kur} blocker, too, exhibits frequency dependency. Hence, to analyze the therapeutic potential of I_{Kur} inhibition at higher rates, we made a simulation to investigate the effect of I_{Kur} inhibition on AP biomarkers at higher rates as encountered in AF condition. The test was subdivided in two, first: concentration dependent effect of Acacetin [5, 10] µM was observed at 2Hz, second: effect of Acacetin (10µM) on AP rate adaptation by varying frequency from 0.5 to 2Hz. Both tests are shown in Figure 6.7 in comparison to the experimental data (Li *et al.* 2008). At 2Hz, the lengthening of AP repolarization phase (Figure 6.7A) is quite long for Acacetin 5µM (in red) then 10µM (in yellow) as compared to control (in blue) and this agrees qualitatively to the experimental AP results (Figure 6.7B). More precisely, Figure 6.7C depicts a quantitative comparison of each phase of repolarization in percentage change with respect to control for acacetin 5µM (in red) and 10µM (in yellow) at 2Hz frequency. The percentage increase in APD_{50} is slightly large at 10µM then at 5µM that is similar to the experimental data trend. The later phase of repolarization is represented by APD_{75} where the varying the Acacetin concentration [5 10] µM produces a small rise (200 vs 230%) that meets qualitatively with experimental results (115 vs 120%). Moving onward, the percentage rise in APD_{90} (168 vs 192%) on varying Acacetin fits qualitatively with the data values (110 vs 115%).

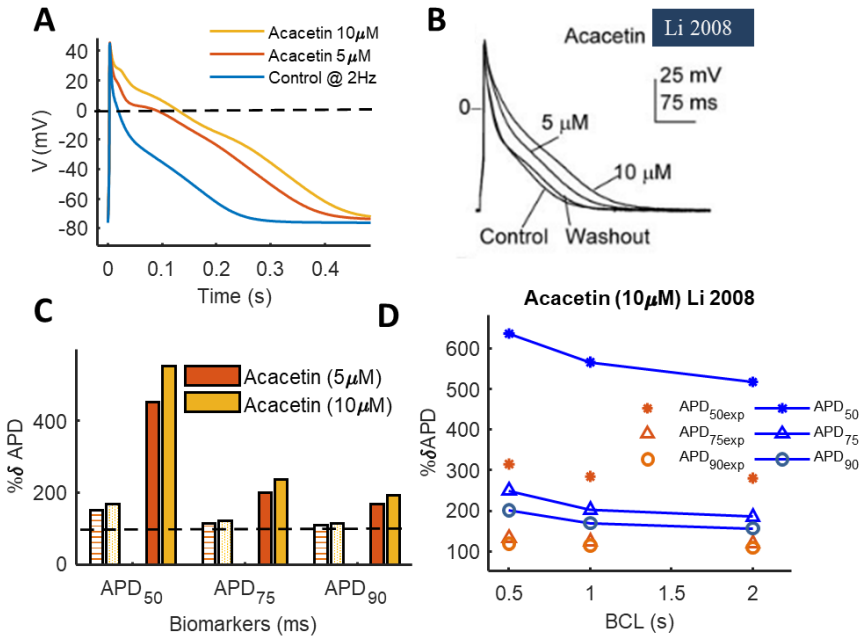

Figure 6.7: Effect of I_{Kur} inhibition at higher rates. Test 1: Acacetin drug concentration dependent response of I_{Kur} block at 2Hz. A) Action potential for control (in blue) in comparison with I_{Kur} blocker 5µM (in red) and 10µM (in yellow) concentrations, B) the experimental APs for control and in presence of acacetin blocker from (Li *et al.* 2008), C) percentage change in APD biomarkers with respect to control for the model (solid filled bars) in comparison to the data (Li *et al.* 2008) (pattern filled bars) for 5µM (in blue) and 10µM (in red) concentration of Acacetin. Test 2: D) Effect of acacetin (10µM) on rate dependent response of APD

biomarkers, APD_{50} (asterisk), APD_{75} (triangles), and APD_{90} (open circles) for model (blue solid line) and data (red data points) from (Li et al. 2008).

The second experiment was performed to analyze the effect of I_{Kur} inhibition on rate adaptation of APD_{50}, APD_{75} and APD_{90} as shown in Figure 6.7D. The model output (in blue solid lines) depicts that the shortening of APD_{90} (open circles) (as seen in experimental data in Figure 3.12B) is now converted into lengthening with rate by the application of Acacetin(10µM). This lengthening of percentage change of APD_{90} fits quantitatively with the experimental data points (in red open circles). Similarly, the percentage increase in APD_{75} (blue solid line with triangles) with rate meets well with the data trend. However, the value of percentage increase of APD_{50} (blue line with asterisk) is quite higher than reported data (in red asterisk) at each frequency but the model APD_{50} is following the trend of percentage increase with increasing rate.

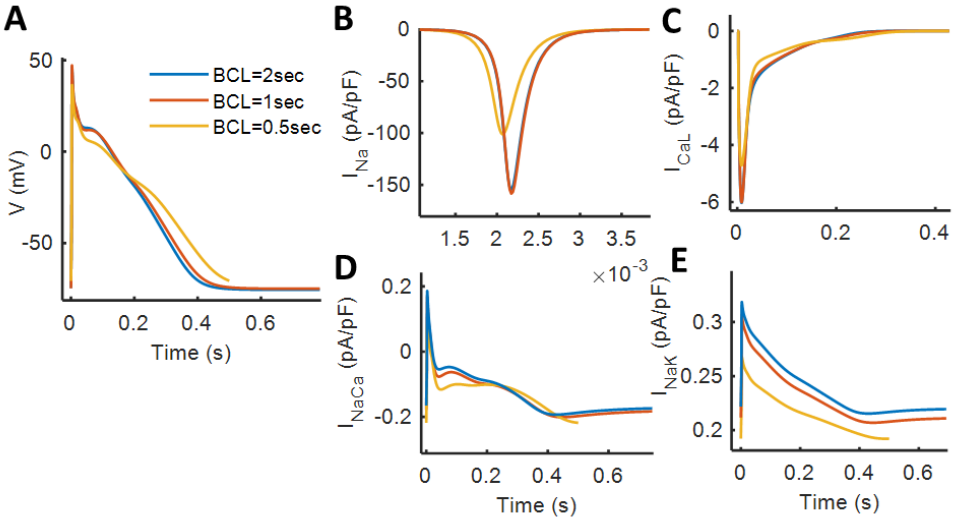

Figure 6.8: Mechanism behind the I_{Kur} block response on AP and ionic currents rate adaptation. A) AP with I_{Kur} block at BCL 2sec (in blue), 1sec (in red) and 0.5sec (in yellow), B) I_{CaL} current rate dependence, C) I_{Na} current, D) I_{NaCa} rate adaptation and E) I_{NaK} current.

6.4 Discussion and Conclusions

In this work, we present the therapeutic potential of I_{Kur} current using optimized MBS2022 model of human atrial electromechanical CMs. Blockade of I_{Kur} current has been proposed as a novel target for the development of effective and safe atrial antiarrhythmic agents. In this work we have assessed the 1) antiarrhythmic effect of I_{Kur} selective and less selective blockers, 2) drug concentration dependent inotropic response, and 3) I_{Kur} block effect on APD rate dependency.

The simulation result comparing the effect of I_{Kur}-selective, 4-AP (5µM) and less selective, AVE0118 (10µM), and Acacetin (10µM) blockers shows the positive inotropic response was slightly more appreciated in the former type (Figure 6.5B). In particular, 4-AP prolonged the APD_{50} more than the less selective drugs with no effect on AP just after the upstroke (resulting in a spike and dome morphology). On the other hand, among less selective drugs, Acacetin (10µM) demonstrates maximum APD prolongation for all phases of repolarization, i.e. APD_{50}, APD_{75} and APD_{90} (Figure 6.5) that can be effective in prolonging APD in AF condition. The I_{Kur} block is

associated with an elevation in plateau region which is more appreciated under less-selective I_{Kur} block type as shown by the biomarker PP (Figure 6.5C). The height of the plateau in turn decides the additional activation (secondary effects) of I_K and I_{CaL} currents. In our model, the sustained I_{CaL} current dominates the raised level of I_{Kr} current with I_{Kur} block hence resulting in a prolongation of APD_{90}. Hence, AP heterogeneity may decide the response of I_{Kur} block on APD_{90} as in experiments, type 1 AP (spike & dome) exhibits APD_{90} shortening (Wettwer *et al.* 2004, Dobrev & Ravens 2003, Ford *et al.* 2016) or no change (Christ *et al.* 2008), whereas the type 3 AP (triangular) shows lengthening effect (Li *et al.* 2008, Wang *et al.* 1993). On the same lines, the human atrial models with type 1 AP morphology like Courtemanche 1998 (Courtemanche *et al.* 1998) demonstrated a shortening effect whereas the type 3 AP like Nygren 1998 (Nygren *et al.* 1998) and the hybrid of two AP types, the Grandi 2011 (Grandi *et al.* 2011), showed a prolongation of APD_{90} as was in our model.

The slowly inactivating I_{CaL} current permits more Ca^{2+} ions to enter the cytosol resulting in elevated Ca^{2+} levels and a positive inotropic response. Meanwhile, in concentration dependent manner, I_{NaCa} shifts its operation mode towards more outward current than inward (Figure 6.6D) resulting in a secondary source of Ca^{2+} ions. Hence, I_{Kur} block can increase the atrial contractility in condition with atrial contractile dysfunction due to atrial tachyarrhythmias.

The effect of I_{Kur} block reverses the rate dependent shortening of APD into lengthening. The mechanism behind this effect is explained well in Figure 6.8 where the major phenomena was two fold: 1) I_{CaL} showed some increase in the late plateau region (Figure 6.8B), 2) The raised inward current of I_{NaCa} and reduced outward current of I_{NaK} (Figure 6.8D&E). The characteristic mechanism of rate dependent Na^+ accumulation is reversed by the I_{Kur} block hence, resulting in a rate dependent reduction in I_{NaK} pump activity and elevated direct mode of I_{NaCa} that combines to prolong the APD_{90} with rate. The primary reduction in I_{Kur} has resulted in secondary effect of reduced Na^+ channel activity (Figure 6.8C) for higher rates. The reduced I_{Na} current can be associated with reduced maximal shortening velocity (dV/dt_{max}) that is highly sensitive to the changes close to V_{diast} value (Skibsbye *et al.* 2016). Hence, a reduced I_{Na} current can be speculated as causing a prolongation of ERP as was shown in canine right atrial tissue preparation (Burashnikov *et al.* 2012). Prolonged ERP is desirable to disrupt reentrants and to prevent AF recurrence especially at higher pacing rates. Hence, our optimized model demonstrates a reduced I_{Na} current resulting in an ERP prolongation at higher frequencies, suggesting that I_{Kur} inhibition can be effective for reversing the AF and reducing the AF burden.

The optimized model was validated based on antiarrhythmic effects of atrial I_{Kur} selective block. Our results suggest that the selective I_{Kur} blockers can be more efficient in reversing the AF induced remodeling effects on electrophysiology and contractility. This optimized coupled model will provide a framework for multi-scale modeling and to gain insights into pathophysiological mechanisms.

Conclusion

The thesis begins with a short state-of-the-art review of human electromechanically coupled computational models. The review confirms the gap in integrated models since the available models are either based on ventricular physiology or are modeled via separate tracks of excitation and contraction. With this motivation, the thesis comprises of a initial study based on coupling of existing human atrial action potential (AP) and contraction models. The study identified that the coupled model showed a incorrect force-frequency relationship that was always decreasing with rate contrary to the dome shaped inotropic response. The major reason behind this discrepancy was the absence of centripetal Ca^{+2} diffusion formulation in the models.

Based on this, we developed a electromechanically coupled model that was calibrated and validated based on human atrial experimental data. The model demonstrated a positive force frequency relationship where the progressive rise of diastolic level of the Ca-transient was the main determinant for a consequent increase in the systolic peak; however, a concurrent progressive decrease with rate of the net Ca^{2+} influx into the bulk cytoplasm takes place, resulting in the overall biphasic rate dependence of the CaT systolic peaks. Using the model, we confirmed that combined rate dependent I_{CaL} reduction and cytosolic Na^{+} accumulation was the major mechanisms behind the APD shortening with rate. In addition, we also observed the AP morphology with a prominent plateau, obtained by I_{Kur} block, was able to enhance the frequency dependent rise in Ca^{+2} concentration via the strong reverse mode current of I_{NaCa} current.

We utilized the model to determine the potential parameters, both from exicitation and contractility, favouring the development of arrhytmogenic substrate for post-operative atrial fibrillation condition. The model demonstrated that with depressed SERCA activity, slow RyR inactivation time was the driving mechanism of alternans incidence at higher rate of 4.2Hz. Using a dynamic alternans pacing protocol we found that CaMKII overexpression was protecting the model from alternans development. The key mechanisms behind the CaMKII based Ca alternans were the SR Ca load and the regulatory kinetics of I_{CaL} current. The absence of MCF effect promted alternans that was because of the lacking dampening effect of Ca-TRPN bound.

The model includes a calibrated parmater set for MEF associated I_{ns} current. Based on the I_{ns} current, the rising level of stretch depolarized the AP the enhanced the contraction plateau. The depolarized resting potential was very sensitive to the upstroke velocity hence to the cell excitability. At higher rates, the rising level of stretch was able to disturb the rate dependent Na^{+} accumulation resulting into reduced I_{NaCa} inward current but a increased reverse mode current. The stretch increased the alternans magnitude and shifted the incidence threshold to lower frequency of 4.2Hz (without MEF alternans appeared at 4.6Hz under control condition). The role of Ca-TRPN increased binding affinity developed because of the increased activation of the TRPN buffer was the underlying mechanism of this raised vulnerability to alternans incidence.

The therapeutic potential of I_{Kur} current block was assessed by comparing I_{Kur}-specific and less specific currents and resulting positive inotropic response. We found that the mide repolarization phase of AP is more important for the coupling or contractility than the late phase.

The I_{Kur}-selective drug produce an AP morphology that produce a inotropic response greater than the less selective blockers. The high frequency response of I_{Kur} block deomostrates the potential for reversing the AF that is speculated by a secondary reduction in I_{Na} current that is desirable to disrupt the reentrants.

The findings and underlying mechanisms shows the developed computational model has the potential to understand the role of each parameter under physiological and pathological conditions. Using the developed model, we have provided a framework for the future studies of integrated mechasims of human atrial cardiomyocytes to understand the causal relationship in a highly non-linear system.

Appendix

Model Equations

Tables

Model Equations

Modified Model equations

The model equations are based on KM2011 and RDQ2020 models. Here we list all those that have been modified or added.

Volume of cytosolic region

$$V_{bc_{Total}} = \sum_{i=1\ to\ 4} V_{bc_i}$$

here V_{bc1}-V_{bc4} is referred to volume of four *bc* compartments in KM2011 model whereas, $V_{bc_{Total}}$ is the total volume of *bc* compartment in MBS2022.

Volume of SR compartment

$$V_{SRss} = 2.25\%(V_{ss} + V_{bc4})$$

$$V_{SRbc} = 2.25\%(sum(V_{bc1}{:}V_{bc3}))$$

Intracellular free Ca^{2+} concentration

$$\frac{dCai_{bc}}{dt} = beta_{nj} * \frac{JCa}{V_{bc_{Total}}}$$

Addition of dynamic troponin effect, $\frac{d[Ca^{2+}]_{TRPN}}{dt}$, in $[Ca^{2+}]_i$:

$$\frac{dCai_{bc}}{dt} = beta_{bc} * \frac{JCa}{V_{bc_{Total}}} - \frac{d[Ca^{2+}]_{TRPN}}{dt}$$

Free Ca^{2+} in SR

$$\frac{dCa_{SR_{ss}}}{dt} = beta_{SR_{ss}} * \left(DCa_{SR} * \left(\frac{-Ca_{SR_{ss}} + Ca_{SR_{bc}}}{dx^2} + \frac{Ca_{SR_{ss}} - Ca_{SR_{bc}}}{2 * 4 * dx^2} \right) + \frac{J_{SRCa_{ss}}}{V_{SR_{ss}}} \right)$$

$$\frac{dCa_{SR_{bc}}}{dt} = beta_{SR_{bc}} * \left(DCa_{SR} * \left(\frac{Ca_{SR_{ss}} - Ca_{SR_{bc}}}{dx^2} + \frac{Ca_{SR_{ss}} - Ca_{SR_{bc}}}{2 * 3 * dx^2} \right) + \frac{J_{SRCa_{bc}}}{V_{SR_{bc}}} \right)$$

I_{Na} current modified as shown,

$$g_{Na} = 350$$

$$E_{Na} = \frac{RT}{F} * \log\left(\frac{Nao}{Nass}\right)$$

$$m_{\infty} = \frac{1}{1 + \exp((V + 36.3)/-7.8)}$$

$$h_{\infty} = \frac{1}{1 + \exp\left(\frac{V + 67}{5.6}\right)}$$

$$m_{tau} = 0.00001 + 0.00013 * \exp\left(-\left(\frac{V + 48}{15}\right)^2\right) + \frac{0.000045}{1 + \exp((V + 42)/-5)}$$

$$h1_{tau} = 0.00007 + \frac{0.034}{1 + \exp\left((V + 41)/5.5\right)} + \exp\left(-\frac{V + 41}{14}\right) + \frac{0.0002}{1 + \exp\left(-(V + 79)/14\right)}$$

$$h2_{tau} = 0.0007 + \frac{0.15}{1 + \exp\left((V + 41)/5.5\right)} + \exp\left(-\frac{V + 41}{14}\right) + \frac{0.002}{1 + \exp\left(-(V + 79)/14\right)}$$

$$I_{Na} = g_{Na} * m * h1 * h2 * (V - E_{Na})$$

Tables

Table A1: Modified parameter values in MBS2022

A. Ionic current related parameters			
Parameter	MBS2022	KM2011	Motivation
g_{Na} (nS)	350	P_{Na}= 0.00182 nL/s	Reformulated according to new experimental data as described in (Skibsbye *et al.* 2016).
g_{CaL} (nS)	14.5	25.3125	To avoid irregular reactivation of I_{CaL} current at the lower frequency of 0.5 Hz
g_{Kur} (nS)	2.35	2.447	To achieve an APD_{50} more inline with the experimental bound as shown in Fig. 4A
g_{K1} (nS)	3.44	3.44	-
g_{to} (nS)	8.175	8.175	-
g_{INaCa} (nS)	0.0083	0.0084 (pA/(mmol/L)^4)	As suggested by Skibsbye et al. 2016.
g_{Cab} (nS)	0.085	0.0952	
k_{Ca} (mM)	0.6e-3	1e-3	
B. CaMKII related parameters			
$CaMK_0$ (-)	0.05		
K_{mCaM} (mM)	0.0015		
K_{mCaMK} (-)	0.15		
α_{CaMK} (s^{-1})	50		
β_{CaMK} (s^{-1})	0.68		
C. Stretch activated current parameters			
K_{ns} (-)	1300		
α_{ns} (-)	427		
g_{ns} (nS)	0.513e-6		
f_{CE} (kPa)	100		
f_{PE} (kPa)	0.006		
f_{SE} (kPa)	2.8		
k_{SE} (μm^{-1})	14.6		
k_{PE} (μm^{-1})	14.6		

Table A2: References used for cell capacitances in experimental data for human atria. *Represents capacitance after compensation.

Reference	Mean	Error	Sample Size
Voigt *et al.* 2012	114.8	5.9	46
Wettwer *et al.* 2004	101	6.5	29
Gulais *et al.* 2004	99.4	9.5	16
Dobrev *et al.* 2001	92	12	30
Voigt *et al.* 2010	90	5	40
Christ *et al.* 2004	88.1	1.9	276
Dobrev *et al.* 2002	83	8	42
Feng *et al.* 1998	79	3.8	35
Fermini *et al.* 1992	78.9	8.4	10
	73.7*	7.7	10
Fakuade *et al.* 2021	75		50
Wang *et al.* 1993	74.3	7.6	34
Kamkin *et al.* 2003	72.4	6.4	14
Schotten *et al.* 2002	72	3	167
Li *et al.* 1997	71	6	35
	67*	6	
Wagoner *et al.* 1999	67.6	2.9	86
Madsen *et al.* 2004	58	7.8	16
Giles *et al.* 1988	54.3	5.87	5
Nygren *et al.* 1998	51.9	3.5	52
Wang *et al.* 1999	29.6	1.8	

Table A2: Human atrial experimental data used for calibration of contraction parameters in the Electro-mechanical model. F_{max}: peak tension, F_{min}: diastolic tension, $ttp_{Factive}$: time to F_{max}, $TT_{Factive}$: twitch time, $rt_{50Factive}$, $rt_{90Factive}$: relaxation time at 50% and 90% of F_{max}, CaT_{max}: Calcium transient peak, CaT_{min}: Calcium transient diastolic, CaT_{amp}: Calcium transient amplitude, rt_{50CaT}: relaxation time at 50% of CaT_{max}, ttp_{CaT}: time to CaT_{max}, Decay time: τ.ecay time: CaT_{min}: Calcium transient diastolic

Reference	**Tissue preparation**	**Biomarker**	**Frequency dependent Biomarkers**
Schotten *et. al* 2002	Muscle strips obtained from right atrial appendages from patients of mitral valve surgery at 1Hz, 37°C. (n=31)	F_{max}, $rt_{90Factive}$	F_{max}, $rt_{90Factive}$
Schwinger *et al.* 1998	Right atrial trabeculae from patients who underwent aortocoronary bypass operations at 1Hz, 37°C. (n=9)	F_{max}	F_{max}
Sossalla *et al.* 2009	Thin right atrial trabeculae were micro-dissected (n=79)	F_{max}, $ttp_{Factive}$, $rt_{50Factive}$, $rt_{90Factive}$	F_{max}, $ttp_{Factive}$, $rt_{50Factive}$, $rt_{90Factive}$
L S. Maier *et al.* 2000	Muscle strips from right atrial trabeculae obtained from patients undergoing aortocoronary bypass operation at 37°C. (n=15)	F_{max}, $TT_{Factive}$, $ttp_{Factive}$, $rt_{50Factive}$, $rt_{90Factive}$, CaT_{max}	F_{max}, CaT_{max}
Flesch *et al.* 1997	Isolated electrically driven human right atrial trabecula from non-failing hearts at 1Hz, 37°C. (n=15)	$ttp_{Factive}$, $rt_{50Factive}$	
Brixius *et al.* 1997	Right atrial tissue from patients having aortocoronary bypass surgery. (n=19)	$ttp_{Factive}$, $rt_{50Factive}$, CaT_{max}	
Schotten *et al.* 2006	Muscle strip preparations from atrial trabeculae obtained from right atrial appendages at 1Hz, 37°C. (n=14)	F_{max}	
Brixius *et al.* 1999	Auricular trabeculae were selected from right atrial tissue. Using Fura-2 ratio method for Ca transient and force in muscle strips at 37°C, 1Hz.	F_{max}, F_{min}, $ttp_{Factive}$, $rt_{50Factive}$, CaT_{max}, CaT_{min}, ttp_{CaT}, rt_{50CaT}	F_{max}, F_{min}, $ttp_{Factive}$, $rt_{50Factive}$, CaT_{max}, CaT_{min}, ttp_{CaT}, rt_{50CaT}
Voigt *et al.* 2012	Human atrial myocytes isolated from right atrial appendage at 37°C for 40 myocytes extracted from 20 patients.	CaT_{min}, CaT_{sys}, CaT_{amp}, τ	

Voigt *et al.* 2014	Human atrial appendages from 73 patients were isolated at 37°C.	$CaT_{min,}$ CaT_{sys}, CaT_{amp}, τ
Heijman *et al.* 2020	71 out of 149 RA-appendages were subject to cardiomyocytes isolation at 37°C.	$CaT_{min,}$ CaT_{sys}, CaT_{amp}, τ
Grandi *et al.* 2011	Atrial myocytes extracted from right atrial appendages were isolated using enzymatic dissociation at 37°C.	$CaT_{min,}$ CaT_{sys}, CaT_{amp}
Fakuade *et al.* 2021	Myocytes (n=78) were isolated from 38 patients extracted from right atrial appendages.	$CaT_{min,}$ CaT_{sys}, CaT_{amp}, τ

Table A4: Human atrial experimental biomarkers used for calibration in comparison to model original and optimized output at 1Hz frequency. The data is shown by mean value along with their lower and upper bounds. Biomarkers for action potential are: duration at 30%, 50% and 90% of repolarization (APD_{30}, APD_{50}, APD_{90}), amplitude (V_{amp}), diastolic (V_{diast}), and maximum upstroke velocity (dV/dt_{max}); for CaT are: relaxation time at 50% of the peak (rt_{50CaT}), time to peak (ttp_{CaT}), and total time (TT_{CaT}); for F_{active} maximum peak value ($F_{active\ max}$), time to peak ($ttp_{Factive}$), relaxation at 50% and 90% of peak ($rt_{50Factive}$, $rt_{90Factive}$), and the twitch time ($TT_{Factive}$).

Type	Biomarker		Mean value [LB UB]	Original Value	Optimized Output
AP	APD_{90}	(ms)	263.05 [202 332]	248	220
	APD_{50}	(ms)	50.02 [25 94.14]	60.2	32.8
	APD_{30}	(ms)	7.725 [5 13.9]	13.4	8.5
	V_{amp}	(mV)	103.266 [83 130]	111	120.9
	V_{diast}	(mV)	-75.1 [-68 -75.1]	-75.7	-75.4
	dV/dt_{max}	(mV/ms)	179.23 [159 231.9]	177	201
CaT	CaT_{max}	(μM)		0.38	0.32
	CaT_{min}	(μM)		0.178	0.152
	rt_{50CaT}	(ms)	177.5 [168.5 186.5]	176	120
	ttp_{CaT}	(ms)	52.5 [49.4 55.6]	93.7	77
	TT_{CaT}	(ms)	539.1 [508.1 570.1]	690	531
F_{active}	$F_{active\ max}$	(kPa)	5.92 [3.14 9.5]	4.7	3.25
	$ttp_{Factive}$	(ms)	104.98 [79. 161]	135.7	117
	$rt_{50Factive}$	(ms)	80.92 [60.2 118.6]	140	108
	$rt_{90Factive}$	(ms)	199 [153 235.9]	406	316
	$TT_{Factive}$	(ms)	433.3 [413.1 453.5]	663	538.6

Table A5: Human atrial experimental biomarkers in comparison to model original used for calibration for rate varying from 0.5, 1, 2 and 3Hz. The data is shown as mean value with their lower and upper bounds. The biomarkers for AP are: percentage change in APD_{90} ($\%\Delta APD_{90}$); for CaT: percentage change in CaT_{max} ($\%\Delta CaT_{max}$), and $[Ca^{2+}]_{SR}$ ($\%\Delta[Ca^{2+}]_{SR}$); and for F_{active}: percentage change in F_{active} peak ($\%\Delta F_{active\ max}$).

Type	Biomarker	Frequency	Mean value [LB UB]	Original Value
AP	$\%\Delta APD_{90}$	0.5	118.34 [114.90 121.78]	102.6
		2	72.1 [58.17 85.84]	92
		3	61.71 [47.09 76.33]	85.9
CaT	$\%\Delta CaT_{max}$	0.5	64.95 [49.45 80.45]	97.3
		2	125.31 [87.71 162.91]	109.1
		3	113.94 [63.43 163.3]	118.9
	$\%\Delta[Ca^{2+}]_{SR}$	0.5	86.2 [76.2 96.2]	97.36
		2	107 [103.77 110.23]	113.58
		3	118 [105 131]	127
F_{active}	$\%\Delta F_{active\ max}$	0.5	72.36 [68.74 75.9]	95.75
		2	110.6 [105.1 116.2]	115.7
		3	90.35 [85.8 94.86]	135.46

Table A6: Parameters list used for optimization with their original values and allowed window of variations with optimization output.

Type	Parameters	Original value [LB UB]	Optimized Output
SERCA	concentration in *bc* (µM)	40 [50 80]	77
	pumping rate in *bc* (s^{-1})	7.5 [7.5 9]	8.92
RyR	Adaptation max and min in *bc* (µM)	0.33 [0.27 0.5]	0.408
		0.236 [0.12 0.45]	0.432
	Adaptation max and min in *ss* (µM)	0.4 [0.3 0.5]	0.4
		0.318 [0.3 0.45]	0.35
	Adaption half activation in *bc* (µM)	0.34 [0.2 0.4]	0.22
	Adaption half activation in *ss* (µM)	0.29 [0.2 0.4]	0.237
	SR_{Ca} half activation in *bc* (mM)	0.8 [0.3 0.9]	0.544
	SR_{Ca} half activation in *ss* (mM)	0.8 [0.3 0.9]	0.735
	SR_{Ca} slope in *ss* (mM)	0.1 [0.05 0.5]	0.13
	SR_{Ca} slope in *bc* (mM)	0.1 [0.05 0.5]	0.19
	Recovery time *ss* (ms)	240 [60 480]	282
	Recovery time *bc* (ms)	350 [87.5 700]	345

References

Barral, Y.S.H., Shuttleworth, J.G., Clerx, M., Whittaker, D.G., Wang, K., Polonchuk, L., Gavaghan, D.J. and Mirams, G.R., (2022). A parameter representing missing charge should be considered when calibrating action potential models. *Frontiers in Physiology*, p.616.

Bartolucci, Chiara, Mohamadamin Forouzandehmehr, Stefano Severi, and Michelangelo Paci. "A Novel In-Silico Electromechanical Model of Human Ventricular Cardiomyocyte." *Frontiers in Physiology* (2022): 1056.

Becker, Anton E. "How structurally normal are human atria in patients with atrial fibrillation?." *Heart Rhythm* 1, no. 5 (2004): 627-631.

Benardeau, A., S. N. Hatem, C. Rucker-Martin, B. Le Grand, L. Mace, P. Dervanian, J. J. Mercadier, and E. Coraboeuf. "Contribution of Na+/Ca2+ exchange to action potential of human atrial myocytes." *American Journal of Physiology-Heart and Circulatory Physiology* 271, no. 3 (1996): H1151-H1161.

Benjamin, Emelia J., Philip A. Wolf, Ralph B. D'Agostino, Halit Silbershatz, William B. Kannel, and Daniel Levy. "Impact of atrial fibrillation on the risk of death: the Framingham Heart Study." *Circulation* 98, no. 10 (1998): 946-952.

Bers, Donald M., and Eleonora Grandi. "CaMKII regulation of cardiac ion channels." *Journal of cardiovascular pharmacology* 54, no. 3 (2009): 180.

Bers, Donald. Excitation-contraction coupling and cardiac contractile force. Vol. 237. *Springer Science & Business Media*, 2001.

Blatter, Lothar A. "The intricacies of atrial calcium cycling during excitation-contraction coupling." *Journal of General Physiology* 149, no. 9 (2017): 857-865.

Blatter, Lothar A., Jens Kockskämper, Katherine A. Sheehan, Aleksey V. Zima, Jörg Hüser, and Stephen L. Lipsius. "Local calcium gradients during excitation–contraction coupling and alternans in atrial myocytes." *The Journal of physiology* 546, no. 1 (2003): 19-31.

Bode, Frank, Alexander Katchman, Raymond L. Woosley, and Michael R. Franz. "Gadolinium decreases stretch-induced vulnerability to atrial fibrillation." *Circulation* 101, no. 18 (2000): 2200-2205.

Bokník, P., Unkel, C., Kirchhefer, U., Kleideiter, U., Klein-Wiele, O., Knapp, J., Linck, B., Lüss, H., Ulrich Müller, F., Schmitz, W. and Vahlensieck, U., (1999). Regional expression of phospholamban in the human heart. *Cardiovascular research*, 43(1), pp.67-76.

Bootman, Martin D., Daniel R. Higazi, Stephen Coombes, and H. Llewelyn Roderick. "Calcium signalling during excitation-contraction coupling in mammalian atrial myocytes." *Journal of cell science* 119, no. 19 (2006): 3915-3925.

Bootman, Martin D., Ioannis Smyrnias, Rüdiger Thul, Stephen Coombes, and H. Llewelyn Roderick. "Atrial cardiomyocyte calcium signalling." *Biochimica et Biophysica Acta (BBA)-Molecular Cell Research* 1813, no. 5 (2011): 922-934.

Bosch, Ralph F., Xiaorong Zeng, Joachim B. Grammer, Katarina Popovic, Christian Mewis, and Volker Kühlkamp. "Ionic mechanisms of electrical remodeling in human atrial fibrillation." *Cardiovascular research* 44, no. 1 (1999): 121-131.

Brette, Fabien, and Clive Orchard. "T-tubule function in mammalian cardiac myocytes." *Circulation research* 92, no. 11 (2003): 1182-1192.

Briston, Sarah J., Katharine M. Dibb, R. John Solaro, David A. Eisner, and Andrew W. Trafford. "Balanced changes in Ca buffering by SERCA and troponin contribute to Ca handling during β-adrenergic stimulation in cardiac myocytes." *Cardiovascular research* 104, no. 2 (2014): 347-354.

Brixius, Klara, Marcus Pietsch, Susanne Hoischen, Jochen Müller-Ehmsen, and Robert HG Schwinger. "Effect of inotropic interventions on contraction and Ca^{2+} transients in the human heart." *Journal of Applied Physiology* 83, no. 2 (1997): 652-660.

Brixius, Klara, Marcus Pietsch, Susanne Hoischen, Jochen Müller-Ehmsen, and Robert HG Schwinger. "Effect of inotropic interventions on contraction and Ca^{2+} transients in the human heart." *Journal of Applied Physiology* 83, no. 2 (1997): 652-660.

Brocklehurst, Paul, Ismail Adeniran, Dongmin Yang, Yong Sheng, Henggui Zhang, and Jianqiao Ye. "A 2D electromechanical model of human atrial tissue using the discrete element method." *BioMed Research International* 2015 (2015).

Burashnikov, Alexander, Hector Barajas-Martinez, Dan Hu, Eyal Nof, Jonathan Blazek, and Charles Antzelevitch. "Atrial-selective prolongation of refractory period with AVE0118 is due principally to inhibition of sodium channel activity." *Journal of Cardiovascular Pharmacology* 59, no. 6 (2012): 539.

Calaghan, S. C., and E. White. "The role of calcium in the response of cardiac muscle to stretch." *Progress in biophysics and molecular biology* 71, no. 1 (1999): 59-90.

Callewaert, Geert, L. Cleemann, and M. Morad. "Caffeine-induced Ca^{2+} release activates Ca^{2+} extrusion via Na^{+}-Ca^{2+} exchanger in cardiac myocytes." *American Journal of Physiology-Cell Physiology* 257, no. 1 (1989): C147-C152.

Campbell, Stuart G., Fred V. Lionetti, Kenneth S. Campbell, and Andrew D. McCulloch. "Coupling of adjacent tropomyosins enhances cross-bridge-mediated cooperative activation in a markov model of the cardiac thin filament." *Biophysical journal* 98, no. 10 (2010): 2254-2264.

Carpenito, Myriam, Diego Fanti, Simona Mega, Giovanni Benfari, Maria Caterina Bono, Andrea Rossi, Flavio Luciano Ribichini, and Francesco Grigioni. "The central role of left atrium in heart failure." *Frontiers in Cardiovascular Medicine* 8 (2021): 704762.

Cazorla, Olivier, Caroline Pascarel, Didier Garnier, and Jean-Yves Le Guennec. "Resting tension participates in the modulation of active tension in isolated guinea pig ventricular myocytes." *Journal of molecular and cellular cardiology* 29, no. 6 (1997): 1629-1637.

Cherry, Elizabeth M., Harold M. Hastings, and Steven J. Evans. "Dynamics of human atrial cell models: restitution, memory, and intracellular calcium dynamics in single cells." *Progress in biophysics and molecular biology* 98, no. 1 (2008): 24-37.

Christ, T., E. Wettwer, N. Voigt, O. Hala, S. Radicke, K. Matschke, A. Varro, D. Dobrev, and U. Ravens. "Pathology-specific effects of the $I_{Kur}/I_{to}/I_{K,ACh}$ blocker AVE0118 on ion channels in human chronic atrial fibrillation." *British journal of pharmacology* 154, no. 8 (2008): 1619-1630.

Christ, T., P. Boknik, S. Wohrl, E. Wettwer, E. M. Graf, R. F. Bosch, M. Knaut, W. Schmitz, U. Ravens, and D. Dobrev. "L-type Ca^{2+} current downregulation in chronic human atrial fibrillation is associated with increased activity of protein phosphatases." *Circulation* 110, no. 17 (2004): 2651-2657.

Colman, Michael A., Oleg V. Aslanidi, Sanjay Kharche, Mark R. Boyett, Clifford Garratt, Jules C. Hancox, and Henggui Zhang. "Pro-arrhythmogenic effects of atrial fibrillation-induced electrical remodelling: insights from the three-dimensional virtual human atria." *The Journal of physiology* 591, no. 17 (2013): 4249-4272.

Courtemanche, Marc, Rafael J. Ramirez, and Stanley Nattel. "Ionic mechanisms underlying human atrial action potential properties: insights from a mathematical model." *American Journal of Physiology-Heart and Circulatory Physiology* 275, no. 1 (1998): H301-H321.

Courtemanche, Marc, Rafael J. Ramirez, and Stanley Nattel. "Ionic targets for drug therapy and atrial fibrillation-induced electrical remodeling: insights from a mathematical model." *Cardiovascular research* 42, no. 2 (1999): 477-489.

Dawodu, Amos Adeyemo, Francesco Monti, Katsunori Iwashiro, Michele Schiariti, Roberta Chiavarelli, and Paolo Emilio Puddu. "The shape of human atrial action potential accounts for different frequency-related changes in vitro." *International journal of cardiology* 54, no. 3 (1996): 237-249.

Decher, Niels, Pradeep Kumar, Teresa Gonzalez, Bernard Pirard, and Michael C. Sanguinetti. "Binding site of a novel Kv1.5 blocker: a “foot in the door” against atrial fibrillation." *Molecular pharmacology* 70, no. 4 (2006): 1204-1211.

Del-Canto, Irene, Lidia Gómez-Cid, Ismael Hernández-Romero, María S. Guillem, María Eugenia Fernández-Santos, Felipe Atienza, Luis Such, Francisco Fernández-Avilés, Francisco J. Chorro, and Andreu M. Climent. "Ranolazine-Mediated Attenuation of Mechanoelectric Feedback in Atrial Myocyte Monolayers." *Frontiers in Physiology* 11 (2020): 922.

Díaz, Mary E., Stephen C. O’neill, and David A. Eisner. "Sarcoplasmic reticulum calcium content fluctuation is the key to cardiac alternans." *Circulation research* 94, no. 5 (2004): 650-656.

Dobesh, David P., John P. Konhilas, and Pieter P. De Tombe. "Cooperative activation in cardiac muscle: impact of sarcomere length." *American Journal of Physiology-Heart and Circulatory Physiology* 282, no. 3 (2002): H1055-H1062.

Dobrev, D., E. Graf, E. Wettwer, H. M. Himmel, O. Hala, C. Doerfel, T. Christ, S. Schuler, and U. Ravens. "Molecular basis of downregulation of G-protein–coupled inward rectifying K+ current (IK, ACh) in chronic human atrial fibrillation: Decrease in Girk4 mRNA correlates with reduced IK, ACh and muscarinic receptor–mediated shortening of action potentials." *Circulation* 104, no. 21 (2001): 2551-2557.

Dobrev, Dobromir, and Ursula Ravens. "Remodeling of cardiomyocyte ion channels in human atrial fibrillation." *Basic research in cardiology* 98, no. 3 (2003): 137-148.

Dobrev, Dobromir, Martin Aguilar, Jordi Heijman, Jean-Baptiste Guichard, and Stanley Nattel. "Postoperative atrial fibrillation: mechanisms, manifestations and management." *Nature Reviews Cardiology* 16, no. 7 (2019): 417-436.

Eckardt, Lars, Paulus Kirchhof, Gerold Mönnig, Günter Breithardt, Martin Borggrefe, and Wilhelm Haverkamp. "Modification of stretch-induced shortening of repolarization by streptomycin in the isolated rabbit heart." *Journal of cardiovascular pharmacology* 36, no. 6 (2000): 711-721.

Eijsbouts, Sabine CM, Mohamed Majidi, Marc van Zandvoort, and Maurits A. Allessie. "Effects of acute atrial dilation on heterogeneity in conduction in the isolated rabbit heart." *Journal of cardiovascular electrophysiology* 14, no. 3 (2003): 269-278.

Eiras, S., N. A. Narolska, R. B. Van Loon, N. M. Boontje, R. Zaremba, C. R. Jimenez, F. C. Visser, W. Stooker, J. van Der Velden, and G. J. M. Stienen. "Alterations in contractile protein composition and function in human atrial dilatation and atrial fibrillation." *Journal of molecular and cellular cardiology* 41, no. 3 (2006): 467-477.

El-Armouche, Ali, Peter Boknik, Thomas Eschenhagen, Lucie Carrier, Michael Knaut, Ursula Ravens, and Dobromir Dobrev. "Molecular determinants of altered Ca^{2+} handling in human chronic atrial fibrillation." *Circulation* 114, no. 7 (2006): 670-680.

Ellinwood, Nicholas, Dobromir Dobrev, Stefano Morotti, and Eleonora Grandi. "In silico assessment of efficacy and safety of IKur inhibitors in chronic atrial fibrillation: role of kinetics and state-dependence of drug binding." *Frontiers in pharmacology* 8 (2017): 799.

Fabbri, Alan, Matteo Fantini, Ronald Wilders, and Stefano Severi. "Computational analysis of the human sinus node action potential: model development and effects of mutations." *The Journal of physiology* 595, no. 7 (2017): 2365-2396.

Fabiato, Alexandre. "Calcium-induced release of calcium from the cardiac sarcoplasmic reticulum." *American Journal of Physiology-Cell Physiology* 245, no. 1 (1983): C1-C14.

Fakuade, Funsho E., Vanessa Steckmeister, Fitzwilliam Seibertz, Judith Gronwald, Stefanie Kestel, Julia Menzel, Julius Ryan D. Pronto et al. "Altered atrial cytosolic calcium handling

contributes to the development of postoperative atrial fibrillation." *Cardiovascular research* 117, no. 7 (2021): 1790-1801.

Feng, Jianlin, Lixia Yue, Zhiguo Wang, and Stanley Nattel. "Ionic mechanisms of regional action potential heterogeneity in the canine right atrium." *Circulation research* 83, no. 5 (1998): 541-551.

Flesch, Markus, Heiko Kilter, Bodo Cremers, Olaf Lenz, Michael Südkamp, Ferdinand Kuhn-Regnier, and Michael Böhm. "Acute effects of nitric oxide and cyclic GMP on human myocardial contractility." *Journal of Pharmacology and Experimental Therapeutics* 281, no. 3 (1997): 1340-1349.

Ford, John, James Milnes, Said El Haou, Erich Wettwer, Simone Loose, Klaus Matschke, Benoit Tyl, Patrick Round, and Ursula Ravens. "The positive frequency-dependent electrophysiological effects of the IKur inhibitor XEN-D0103 are desirable for the treatment of atrial fibrillation." *Heart Rhythm* 13, no. 2 (2016): 555-564.

Forouzandehmehr, Mohamadamin, Jussi T. Koivumäki, Jari Hyttinen, and Michelangelo Paci. "A mathematical model of hiPSC cardiomyocytes electromechanics." *Physiological reports* 9, no. 22 (2021): e15124.

Franz, Michael R., and Frank Bode. "Mechano-electrical feedback underlying arrhythmias: the atrial fibrillation case." *Progress in biophysics and molecular biology* 82, no. 1-3 (2003): 163-174.

Frisk, Michael, Jussi T. Koivumäki, Per A. Norseng, Mary M. Maleckar, Ole M. Sejersted, and William E. Louch. "Variable t-tubule organization and Ca^{2+} homeostasis across the atria." *American Journal of Physiology-Heart and Circulatory Physiology* 307, no. 4 (2014): H609-H620.

Gamble, James, Paul Brian Taylor, and Kenji Alan Kenno. "Myocardial stretch alters twitch characteristics and Ca^{2+} loading of sarcoplasmic reticulum in rat ventricular muscle." *Cardiovascular research* 26, no. 9 (1992): 865-870.

Gao, Wei Dong, Peter H. Backx, Michelle Azan-Backx, and Eduardo Marban. "Myofilament Ca^{2+} sensitivity in intact versus skinned rat ventricular muscle." *Circulation research* 74, no. 3 (1994): 408-415.

Grandi, Eleonora, Sandeep V. Pandit, Niels Voigt, Antony J. Workman, Dobromir Dobrev, José Jalife, and Donald M. Bers. "Human atrial action potential and Ca^{2+} model: sinus rhythm and chronic atrial fibrillation." *Circulation research* 109, no. 9 (2011): 1055-1066.

Greiser, Maura, Benoît-Gilles Kerfant, George SB Williams, Niels Voigt, Erik Harks, Katharine M. Dibb, Anne Giese et al. "Tachycardia-induced silencing of subcellular Ca^{2+} signaling in atrial myocytes." *The Journal of clinical investigation* 124, no. 11 (2014): 4759-4772.

Györke, Inna, and Sandor Györke. "Regulation of the cardiac ryanodine receptor channel by luminal Ca^{2+} involves luminal Ca^{2+} sensing sites." *Biophysical journal* 75, no. 6 (1998): 2801-2810.

Harrison, Simon M., and Mark R. Boyett. "The role of the Na (+)-Ca^{2+} exchanger in the rate-dependent increase in contraction in guinea-pig ventricular myocytes." *The Journal of physiology* 482, no. 3 (1995): 555-566.

Hatem, Stephane N., Agnes Benardeau, Catherine Rucker-Martin, Isabelle Marty, Patricia de Chamisso, Michel Villaz, and Jean-Jacques Mercadier. "Different compartments of sarcoplasmic reticulum participate in the excitation-contraction coupling process in human atrial myocytes." *Circulation research* 80, no. 3 (1997): 345-353.

Heijman, Jordi, Azinwi Phina Muna, Tina Veleva, Cristina E. Molina, Henry Sutanto, Marcel Tekook, Qiongling Wang et al. "Atrial myocyte NLRP3/CaMKII nexus forms a substrate for postoperative atrial fibrillation." *Circulation research* 127, no. 8 (2020): 1036-1055.

Heijman, Jordi, Henry Sutanto, Harry JGM Crijns, Stanley Nattel, and Natalia A. Trayanova. "Computational models of atrial fibrillation: Achievements, challenges, and perspectives for improving clinical care." *Cardiovascular Research* 117, no. 7 (2021): 1682-1699.

Heijman, Jordi, Pegah Erfanian Abdoust, Niels Voigt, Stanley Nattel, and Dobromir Dobrev. "Computational models of atrial cellular electrophysiology and calcium handling, and their role in atrial fibrillation." *The Journal of physiology* 594, no. 3 (2016): 537-553.

Hill, Archibald Vivian. "The heat of shortening and the dynamic constants of muscle." Proceedings of the Royal Society of London. *Series B-Biological Sciences* 126, no. 843 (1938): 136-195.

Hindricks, Gerhard, Tatjana Potpara, Nikolaos Dagres, Elena Arbelo, Jeroen J. Bax, Carina Blomström-Lundqvist, Giuseppe Boriani et al. "2020 ESC Guidelines for the diagnosis and management of atrial fibrillation developed in collaboration with the European Association for Cardio-Thoracic Surgery (EACTS) The Task Force for the diagnosis and management of atrial fibrillation of the European Society of Cardiology (ESC) Developed with the special contribution of the European Heart Rhythm Association (EHRA) of the ESC." *European heart journal* 42, no. 5 (2021): 373-498.

Ho, Siew Yen, José Angel Cabrera, and Damian Sanchez-Quintana. "Left atrial anatomy revisited." *Circulation: Arrhythmia and Electrophysiology* 5, no. 1 (2012): 220-228.

Hoit, Brian D. "Left atrial size and function: role in prognosis." *Journal of the American College of Cardiology* 63, no. 6 (2014): 493-505.

Hołda, Jakub, Katarzyna Słodowska, Kamil Tyrak, Filip Bolechała, Katarzyna A. Jasińska, Mateusz Koziej, Mateusz K. Hołda, and Jerzy A. Walocha. "Topographical anatomy of the right atrial appendage vestibule and its isthmuses." *Journal of Cardiovascular Electrophysiology* 31, no. 12 (2020): 3199-3206.

Huke, Sabine, and Björn C. Knollmann. "Increased myofilament Ca^{2+}-sensitivity and arrhythmia susceptibility." *Journal of molecular and cellular cardiology* 48, no. 5 (2010): 824-833.

Hüser, J., S. L. Lipsius, and L. A. Blatter. "Calcium gradients during excitation-contraction coupling in cat atrial myocytes." *The Journal of physiology* 494, no. 3 (1996): 641-651.

Hüser, J., Wang, Y.G., Sheehan, K.A., Cifuentes, F., Lipsius, S.L. and Blatter, L.A., (2000). Functional coupling between glycolysis and excitation—contraction coupling underlies alternans in cat heart cells. *The Journal of physiology*, 524(3), pp.795-806.

Hussain, M., G. A. Drago, J. Colyer, and C. H. Orchard. "Rate-dependent abbreviation of Ca^{2+} transient in rat heart is independent of phospholamban phosphorylation." *American Journal of Physiology-Heart and Circulatory Physiology* 273, no. 2 (1997): H695-H706.

Huxley, Andrew F. "Muscle structure and theories of contraction." Prog. Biophys. Biophys. Chem 7 (1957): 255-318.

Iribe, Gentaro, and Peter Kohl. "Axial stretch enhances sarcoplasmic reticulum Ca^{2+} leak and cellular Ca^{2+} reuptake in guinea pig ventricular myocytes: experiments and models." *Progress in biophysics and molecular biology* 97, no. 2-3 (2008): 298-311.

Jakob, Dorothee, Alexander Klesen, Benoit Allegrini, Elisa Darkow, Diana Aria, Ramona Emig, Ana Simon Chica et al. "Piezo1 and BKca channels in human atrial fibroblasts: Interplay and remodelling in atrial fibrillation." *Journal of Molecular and Cellular Cardiology* 158 (2021): 49-62.

Ji, Yanyan Claire, Richard A. Gray, and Flavio H. Fenton. (2015). Implementation of contraction to electrophysiological ventricular myocyte models, and their quantitative characterization via post-extrasystolic potentiation. *PloS one* 10.8, e0135699.

Kamkin, A., I. Kiseleva, and G. Isenberg. "Stretch-activated currents in ventricular myocytes: amplitude and arrhythmogenic effects increase with hypertrophy." *Cardiovascular research* 48, no. 3 (2000): 409-420.

Kamkin, Andre, Irina Kiseleva, Kay-Dietrich Wagner, Jürgen Bohm, Heinz Theres, Joachim Günther, and Holger Scholz. "Characterization of stretch-activated ion currents in isolated atrial myocytes from human hearts." *Pflügers Archiv* 446, no. 3 (2003): 339-346.

Kanaporis, Giedrius, and Lothar A. Blatter. "Membrane potential determines calcium alternans through modulation of SR Ca^{2+} load and L-type Ca^{2+} current." *Journal of molecular and cellular cardiology* 105 (2017): 49-58.

Kentish, Jonathan C., and Antoni Wrzosek. "Changes in force and cytosolic Ca^{2+} concentration after length changes in isolated rat ventricular trabeculae." *The Journal of physiology* 506, no. Pt 2 (1998): 431.

Kim, Donghee. "Novel cation-selective mechanosensitive ion channel in the atrial cell membrane." *Circulation research* 72, no. 1 (1993): 225-231.

Kirchhof, Paulus, Stefano Benussi, Dipak Kotecha, Anders Ahlsson, Dan Atar, Barbara Casadei, Manuel Castella et al. "2016 ESC Guidelines for the management of atrial fibrillation developed in collaboration with EACTS." *Kardiologia Polska (Polish Heart Journal)* 74, no. 12 (2016): 1359-1469.

Kockskämper, Jens, Dirk von Lewinski, Mounir Khafaga, Andreas Elgner, Michael Grimm, Thomas Eschenhagen, Philip A. Gottlieb, Frederick Sachs, and Burkert Pieske. "The slow force response to stretch in atrial and ventricular myocardium from human heart: functional relevance and subcellular mechanisms." *Progress in biophysics and molecular biology* 97, no. 2-3 (2008): 250-267.

Kohl, Peter, and Frederick Sachs. "Mechanoelectric feedback in cardiac cells." *Philosophical Transactions of the Royal Society of London. Series A: Mathematical, Physical and Engineering Sciences* 359, no. 1783 (2001): 1173-1185.

Kohl, Peter, Jean-Yves LeGuennec, and White Ed. "Diastolic (dys-) function and electrophysiology." *Cardiology Clinics* 18, no. 3 (2000): 637-651.

Koivumäki, J.T., Takalo, J., Korhonen, T., Tavi, P. and Weckström, M., (2009). Modelling sarcoplasmic reticulum calcium ATPase and its regulation in cardiac myocytes. *Philosophical Transactions of the Royal Society A: Mathematical, Physical and Engineering Sciences*, 367(1896), pp.2181-2202.

Koivumäki, Jussi T., Gunnar Seemann, Mary M. Maleckar, and Pasi Tavi. "In silico screening of the key cellular remodeling targets in chronic atrial fibrillation." *PLoS computational biology* 10, no. 5 (2014): e1003620.

Koivumäki, Jussi T., Topi Korhonen, and Pasi Tavi. "Impact of sarcoplasmic reticulum calcium release on calcium dynamics and action potential morphology in human atrial myocytes: a computational study." *PLoS computational biology* 7, no. 1 (2011): e1001067.

Kornej, Jelena, Christin S. Börschel, Emelia J. Benjamin, and Renate B. Schnabel. "Epidemiology of atrial fibrillation in the 21st century: novel methods and new insights." *Circulation research* 127, no. 1 (2020): 4-20.

Kuijpers, Nico HL, Huub MM ten Eikelder, Peter HM Bovendeerd, Sander Verheule, Theo Arts, and Peter AJ Hilbers. "Mechanoelectric feedback leads to conduction slowing and block in acutely dilated atria: a modeling study of cardiac electromechanics." *American Journal of Physiology-Heart and Circulatory Physiology* 292, no. 6 (2007): H2832-H2853.

LAB, MAX J. "Transient depolarisation and action potential alterations following mechanical changes in isolated myocardium." *Cardiovascular Research* 14, no. 11 (1980): 624-637.

Lagrutta, Armando, Jixin Wang, Bernard Fermini, and Joseph J. Salata. "Novel, potent inhibitors of human Kv1. 5 K+ channels and ultrarapidly activating delayed rectifier potassium current." *Journal of Pharmacology and Experimental Therapeutics* 317, no. 3 (2006): 1054-1063.

Land, Sander, and Steven Alexander Niederer. "Influence of atrial contraction dynamics on cardiac function." *International journal for numerical methods in biomedical engineering* 34, no. 3 (2018): e2931.

Lee, Eun-Jeong, Joshua Nedrud, Peter Schemmel, Michael Gotthardt, Thomas C. Irving, and Henk L. Granzier. "Calcium sensitivity and myofilament lattice structure in titin N2B KO mice." *Archives of biochemistry and biophysics* 535, no. 1 (2013): 76-83.

Lee, Yongjae, Barış Cansız, and Michael Kaliske. "Computational modelling of mechano-electric feedback and its arrhythmogenic effects in human ventricular models." *Computer Methods in Biomechanics and Biomedical Engineering* (2022): 1-17.

Li, G.R. and Nattel, S.T.A.N.L.E.Y., (1997). Properties of human atrial ICa at physiological temperatures and relevance to action potential. *American Journal of Physiology-Heart and Circulatory Physiology*, 272(1), pp.H227-H235.

Li, Gui-Rong, Hong-Bing Wang, Guo-Wei Qin, Man-Wen Jin, Qiang Tang, Hai-Ying Sun, Xin-Ling Du et al. "Acacetin, a natural flavone, selectively inhibits human atrial repolarization potassium currents and prevents atrial fibrillation in dogs." *Circulation* 117, no. 19 (2008): 2449-2457.

Liu, Zhao, J. Emanuel Finet, Julie A. Wolfram, Mark E. Anderson, Xun Ai, and J. Kevin Donahue. "Calcium/calmodulin-dependent protein kinase II causes atrial structural remodeling associated with atrial fibrillation and heart failure." *Heart Rhythm* 16, no. 7 (2019): 1080-1088.

Llach, Anna, Cristina E. Molina, Jacqueline Fernandes, Josep Padró, Juan Cinca, and Leif Hove-Madsen. "Sarcoplasmic reticulum and L-type Ca^{2+} channel activity regulate the beat-to-beat stability of calcium handling in human atrial myocytes." *The Journal of physiology* 589, no. 13 (2011): 3247-3262.

Lookin, Oleg, and Yuri Protsenko. "Length-dependent activation of contractility and Ca-transient kinetics in auxotonically contracting isolated rat ventricular cardiomyocytes." *Frontiers in Physiology* 10 (2019): 1473.

Lyon, Aurore, Lauren J. Dupuis, Theo Arts, Harry JGM Crijns, Frits W. Prinzen, Tammo Delhaas, Jordi Heijman, and Joost Lumens. "Differentiating the effects of β-adrenergic stimulation and stretch on calcium and force dynamics using a novel electromechanical cardiomyocyte model." *American Journal of Physiology-Heart and Circulatory Physiology* 319, no. 3 (2020): H519-H530.

Maier, Lars S., Paul Barckhausen, Jutta Weisser, Ivo Aleksic, Mersa Baryalei, and Burkert Pieske. "Ca^{2+} handling in isolated human atrial myocardium." *American Journal of Physiology-Heart and Circulatory Physiology* 279, no. 3 (2000): H952-H958.

Margara, Francesca, Zhinuo J. Wang, Francesc Levrero-Florencio, Alfonso Santiago, Mariano Vázquez, Alfonso Bueno-Orovio, and Blanca Rodriguez. "In-silico human electro-mechanical ventricular modelling and simulation for drug-induced pro-arrhythmia and inotropic risk assessment." *Progress in biophysics and molecular biology* 159 (2021): 58-74.

Mazhar, Fazeelat, Chiara Bartolucci, Francesco Regazzoni, Luca Dedè, Alfio Quarteroni, Cristiana Corsi, and Stefano Severi. " A Detailed Mathematical Model of the Human Atrial Cardiomyocyte: Integration of Electrophysiology and Cardiomechanics" Under Revision in special issue 'Cardiac Mechano-Electric Crosstalk', *Journal of physiology*.

Mazhar, Fazeelat, Francesco Regazzoni, Chiara Bartolucci, Cristiana Corsi, Luca Dedè, Alfio Quarteroni, and Stefano Severi. "Electro-Mechanical Coupling in Human Atrial Cardiomyocytes: Model Development and Analysis of Inotropic Interventions." In *2021 Computing in Cardiology (CinC)*, vol. 48, pp. 1-4. IEEE, 2021.

Methawasin, Mei, Kirk R. Hutchinson, Eun-Jeong Lee, John E. Smith III, Chandra Saripalli, Carlos G. Hidalgo, Coen AC Ottenheijm, and Henk Granzier. "Experimentally increasing titin compliance in a novel mouse model attenuates the Frank-Starling mechanism but has a beneficial effect on diastole." *Circulation* 129, no. 19 (2014): 1924-1936.

Michailova, A., DelPrincipe, F., Egger, M. and Niggli, E., (2002). Spatiotemporal features of Ca^{2+} buffering and diffusion in atrial cardiac myocytes with inhibited sarcoplasmic reticulum. *Biophysical journal*, 83(6), pp.3134-3151.

Miyasaka, Yoko, Marion E. Barnes, Bernard J. Gersh, Stephen S. Cha, Kent R. Bailey, Walter P. Abhayaratna, James B. Seward, and Teresa SM Tsang. "Secular trends in incidence of atrial fibrillation in Olmsted County, Minnesota, 1980 to 2000, and implications on the projections for future prevalence." *Circulation* 114, no. 2 (2006): 119-125.

Morano, Ingo, Holger Arndt, C. Gärtner, and J. C. Rüegg. "Skinned fibers of human atrium and ventricle: myosin isoenzymes and contractility." *Circulation research* 62, no. 3 (1988): 632-639.

Morotti, Stefano, Caroline Liu, Bence Hegyi, Haibo Ni, Alex Fogli Iseppe, Lianguo Wang, Marco Pritoni et al. "Quantitative cross-species translators of cardiac myocyte electrophysiology: Model training, experimental validation, and applications." *Science advances* 7, no. 47 (2021): eabg0927.

Namana, Vinod, Sushilkumar Satish Gupta, Nitin Sabharwal, and Gerald Hollander. "Clinical significance of atrial kick." *QJM: An International Journal of Medicine* (2018).

Narayan, Sanjiv M., Michael R. Franz, Paul Clopton, Etienne J. Pruvot, and David E. Krummen. "Repolarization alternans reveals vulnerability to human atrial fibrillation." *Circulation* 123, no. 25 (2011): 2922-2930.

Narolska, N. A., R. B. Van Loon, N. M. Boontje, Ruud Zaremba, S. Eiras Penas, J. Russell, S. R. Spiegelenberg et al. "Myocardial contraction is 5-fold more economical in ventricular than in atrial human tissue." *Cardiovascular research* 65, no. 1 (2005): 221-229.

Nazir, Sirfraz A., and Max J. Lab. "Mechanoelectric feedback and atrial arrhythmias." *Cardiovascular research* 32, no. 1 (1996): 52-61.

Nazir, Sirfraz A., and Max J. Lab. "Mechanoelectric feedback in the atrium of the isolated guinea-pig heart." *Cardiovascular research* 32, no. 1 (1996): 112-119.

Neef, Stefan, Nataliya Dybkova, Samuel Sossalla, Katharina R. Ort, Nina Fluschnik, Kay Neumann, Ralf Seipelt, Friedrich A. Schöndube, Gerd Hasenfuss, and Lars S. Maier. "CaMKII-dependent diastolic SR Ca^{2+} leak and elevated diastolic Ca^{2+} levels in right atrial myocardium of patients with atrial fibrillation." *Circulation research* 106, no. 6 (2010): 1134-1144.

Neves, João S., André M. Leite-Moreira, Manuel Neiva-Sousa, João Almeida-Coelho, Ricardo Castro-Ferreira, and Adelino F. Leite-Moreira. "Acute myocardial response to stretch: what we (don't) know." *Frontiers in physiology* 6 (2016): 408.

Ni, Haibo, Dominic G. Whittaker, Wei Wang, Wayne R. Giles, Sanjiv M. Narayan, and Henggui Zhang. "Synergistic anti-arrhythmic effects in human atria with combined use of sodium blockers and acacetin." *Frontiers in Physiology* 8 (2017): 946.

Ni, Haibo, Stefano Morotti, Xianwei Zhang, Dobromir Dobrev, and Eleonora Grandi. "Integrative human atrial modeling unravels interactive PKA and CaMKII signaling as key determinant of atrial arrhythmogenesis." *bioRxiv* (2022).

Niederer, Steven A., Kenneth S. Campbell, and Stuart G. Campbell. "A short history of the development of mathematical models of cardiac mechanics." *Journal of molecular and cellular cardiology* 127 (2019): 11-19.

Nygren, Anders, Céline Fiset, Ludwik Firek, John W. Clark, Douglas S. Lindblad, Robert B. Clark, and Wayne R. Giles. "Mathematical model of an adult human atrial cell: the role of K+ currents in repolarization." *Circulation research* 82, no. 1 (1998): 63-81.

O'Hara, Thomas, László Virág, András Varró, and Yoram Rudy. "Simulation of the undiseased human cardiac ventricular action potential: model formulation and experimental validation." *PLoS computational biology* 7, no. 5 (2011): e1002061.

Paci, Michelangelo, Elisa Passini, Aleksandra Klimas, Stefano Severi, Jari Hyttinen, Blanca Rodriguez, and Emilia Entcheva. "In silico populations optimized on optogenetic recordings predict drug effects in human induced pluripotent stem cell-derived cardiomyocytes." *In 2018 Computing in Cardiology Conference (CinC)*, vol. 45, pp. 1-4. IEEE, 2018.

Paci, Michelangelo, Elisa Passini, Aleksandra Klimas, Stefano Severi, Jari Hyttinen, Blanca Rodriguez, and Emilia Entcheva. "All-optical electrophysiology refines populations of in silico human iPSC-CMs for drug evaluation." *Biophysical journal* 118, no. 10 (2020): 2596-2611.

Paci, Michelangelo, Risto-Pekka Pölönen, Dario Cori, Kirsi Penttinen, Katriina Aalto-Setälä, Stefano Severi, and Jari Hyttinen. "Automatic optimization of an in-silico model of human iPSC derived cardiomyocytes recapitulating calcium handling abnormalities." *Frontiers in physiology* 9 (2018): 709.

Peyronnet, Rémi, Jeanne M. Nerbonne, and Peter Kohl. "Cardiac mechano-gated ion channels and arrhythmias." *Circulation research* 118, no. 2 (2016): 311-329.

Pfeiffer, Emily R., Jared R. Tangney, Jeffrey H. Omens, and Andrew D. McCulloch. "Biomechanics of cardiac electromechanical coupling and mechanoelectric feedback." *Journal of biomechanical engineering* 136, no. 2 (2014): 021007.

Picht, Eckard, Jaime DeSantiago, Lothar A. Blatter, and Donald M. Bers. "Cardiac alternans do not rely on diastolic sarcoplasmic reticulum calcium content fluctuations." *Circulation research* 99, no. 7 (2006): 740-748.

Pieske, Burkert, Bodo Kretschmann, Markus Meyer, Christian Holubarsch, Jörg Weirich, Herbert Posival, Kazatomo Minami, Hanjörg Just, and Gerd Hasenfuss. "Alterations in intracellular calcium handling associated with the inverse force-frequency relation in human dilated cardiomyopathy." *Circulation* 92, no. 5 (1995): 1169-1178.

Piroddi, N., Belus, A., Scellini, B., Tesi, C., Giunti, G., Cerbai, E., Mugelli, A. and Poggesi, C., (2007). Tension generation and relaxation in single myofibrils from human atrial and ventricular myocardium. *Pflügers Archiv-European Journal of Physiology*, 454(1), pp.63-73.

Pueyo, Esther, Michele Orini, José F. Rodríguez, and Peter Taggart. "Interactive effect of beta-adrenergic stimulation and mechanical stretch on low-frequency oscillations of ventricular action potential duration in humans." *Journal of Molecular and Cellular Cardiology* 97 (2016): 93-105.

Qu, Zhilin, and James N. Weiss. "Cardiac Alternans: From Bedside to Bench and Back." *Circulation Research* 132, no. 1 (2023): 127-149.

Quinn, T. Alexander, and Peter Kohl. "Cardiac mechano-electric coupling: acute effects of mechanical stimulation on heart rate and rhythm." *Physiological reviews* 101, no. 1 (2021): 37-92.

Ravelli, Flavia, and Maurits Allessie. "Effects of atrial dilatation on refractory period and vulnerability to atrial fibrillation in the isolated Langendorff-perfused rabbit heart." *Circulation* 96, no. 5 (1997): 1686-1695.

Ravelli, Flavia, Marcello Disertori, Fulvio Cozzi, Renzo Antolini, and Maurits A. Allessie. "Ventricular beats induce variations in cycle length of rapid (type II) atrial flutter in humans. Evidence of leading circle reentry." *Circulation* 89, no. 5 (1994): 2107-2116.

Ravelli, Flavia, Michela Masè, Maurizio Del Greco, Massimiliano Marini, and Marcello Disertori. "Acute atrial dilatation slows conduction and increases AF vulnerability in the human atrium." *Journal of cardiovascular electrophysiology* 22, no. 4 (2011): 394-401.

Ravelli, Flavia. "Mechano-electric feedback and atrial fibrillation." *Progress in biophysics and molecular biology* 82, no. 1-3 (2003): 137-149.

Ravens, Ursula, and Erich Wettwer. "Ultra-rapid delayed rectifier channels: molecular basis and therapeutic implications." *Cardiovascular research* 89, no. 4 (2011): 776-785.

Ravens, Ursula, and Katja E. Odening. "Atrial fibrillation: therapeutic potential of atrial K^+ channel blockers." *Pharmacology & Therapeutics* 176 (2017): 13-21.

Ravens, Ursula. "Mechano-electric feedback and arrhythmias." *Progress in biophysics and molecular biology* 82, no. 1-3 (2003): 255-266.

Regazzoni, Francesco, Luca Dedè, and Alfio Quarteroni. "Active force generation in cardiac muscle cells: mathematical modeling and numerical simulation of the actin-myosin interaction." *Vietnam Journal of Mathematics* 49, no. 1 (2021): 87-118.

Regazzoni, Francesco, Luca Dedè, and Alfio Quarteroni. "Biophysically detailed mathematical models of multiscale cardiac active mechanics." *PLoS computational biology* 16, no. 10 (2020): e1008294.

Reiser, P.J., Portman, M.A., Ning, X.H. and Moravec, C.S., (2001). "Human cardiac myosin heavy chain isoforms in fetal and failing adult atria and ventricles." *American Journal of Physiology-Heart and Circulatory Physiology*, 280(4), pp.H1814-H1820.

Rice, J. Jeremy, Raimond L. Winslow, and William C. Hunter. "Comparison of putative cooperative mechanisms in cardiac muscle: length dependence and dynamic responses." *American Journal of Physiology-Heart and Circulatory Physiology* 276, no. 5 (1999): H1734-H1754.

Robertson, S. P., J. DAVID Johnson, and J. D. Potter. (1981). The time-course of Ca^{2+} exchange with calmodulin, troponin, parvalbumin, and myosin in response to transient increases in Ca^{2+} . *Biophysical journal* 34.3, pp.559-569.

Ruf, Thorsten, Heiner Schulte-Baukloh, Jens Lüdemann, Herbert Posival, Friedhelm Beyersdorf, Hanjörg Just, and Christian Holubarsch. "Alterations of cross-bridge kinetics in human atrial and ventricular myocardium." *Cardiovascular research* 40, no. 3 (1998): 580-590.

Sachse, Frank B., Gunnar Seemann, Kraisorn Chaisaowong, and D. A. N. I. E. L. WEIß. "Quantitative reconstruction of cardiac electromechanics in human myocardium: assembly of electrophysiologic and tension generation models." *Journal of cardiovascular electrophysiology* 14 (2003): S210-S218.

Sah, Rajan, Rafael J. Ramirez, Gavin Y. Oudit, Dominica Gidrewicz, Maria G. Trivieri, Carsten Zobel, and Peter H. Backx. "Regulation of cardiac excitation–contraction coupling by action potential repolarization: role of the transient outward potassium current (Ito)." *The Journal of physiology* 546, no. 1 (2003): 5-18.

Schotten, U., de Haan, S., Verheule, S., Harks, E.G., Frechen, D., Bodewig, E., Greiser, M., Ram, R., Maessen, J., Kelm, M. and Allessie, M., (2007). "Blockade of atrial-specific K+-currents increases atrial but not ventricular contractility by enhancing reverse mode Na+/Ca^{2+}-exchange." *Cardiovascular research*, 73(1), pp.37-47.

Schotten, Ulrich, Hans-Ruprecht Neuberger, and Maurits A. Allessie. "The role of atrial dilatation in the domestication of atrial fibrillation." *Progress in biophysics and molecular biology* 82, no. 1-3 (2003): 151-162.

Schotten, Ulrich, Maura Greiser, Dirk Benke, Kai Buerkel, Britta Ehrenteidt, Christoph Stellbrink, Jaime F. Vazquez-Jimenez, Friedrich Schoendube, Peter Hanrath, and Maurits Allessie. "Atrial fibrillation-induced atrial contractile dysfunction: a tachycardiomyopathy of a different sort." *Cardiovascular research* 53, no. 1 (2002): 192-201.

Schwinger, Robert HG, Michael Böhm, Andrea Koch, Rainer Uhlmann, Peter Überfuhr, Eckhart Kreuzer, Bruno Reichart, and Erland Erdmann. "Force-frequency-relation in human atrial and ventricular myocardium." *In Cellular Function and Metabolism*, pp. 73-78. Springer, Boston, MA, 1993.

Severi, Stefano, Cristiana Corsi, and Elisabetta Cerbai. "From in vivo plasma composition to in vitro cardiac electrophysiology and in silico virtual heart: the extracellular calcium enigma." *Philosophical Transactions of the Royal Society A: Mathematical, Physical and Engineering Sciences* 367, no. 1896 (2009): 2203-2223.

Shannon, Thomas R., Kenneth S. Ginsburg, and Donald M. Bers. "Potentiation of fractional sarcoplasmic reticulum calcium release by total and free intra-sarcoplasmic reticulum calcium concentration." *Biophysical journal* 78, no. 1 (2000): 334-343.

Shannon, Thomas R., Kenneth S. Ginsburg, and Donald M. Bers. "Reverse mode of the sarcoplasmic reticulum calcium pump and load-dependent cytosolic calcium decline in voltage-clamped cardiac ventricular myocytes." *Biophysical Journal* 78, no. 1 (2000): 322-333.

Shettigar, Vikram, Bo Zhang, Sean C. Little, Hussam E. Salhi, Brian J. Hansen, Ning Li, Jianchao Zhang et al. "Rationally engineered Troponin C modulates in vivo cardiac function and performance in health and disease." *Nature communications* 7, no. 1 (2016): 1-13.

Shkryl, Vyacheslav M., and Lothar A. Blatter. "Ca^{2+} release events in cardiac myocytes up close: insights from fast confocal imaging." *PLoS One* 8, no. 4 (2013): e61525.

Shkryl, Vyacheslav M., Joshua T. Maxwell, Timothy L. Domeier, and Lothar A. Blatter. "Refractoriness of sarcoplasmic reticulum Ca^{2+} release determines Ca^{2+} alternans in atrial myocytes." *American Journal of Physiology-Heart and Circulatory Physiology* 302, no. 11 (2012): H2310-H2320.

Skibsbye, Lasse, Thomas Jespersen, Torsten Christ, Mary M. Maleckar, Jonas van den Brink, Pasi Tavi, and Jussi T. Koivumäki. "Refractoriness in human atria: Time and voltage dependence of sodium channel availability." *Journal of molecular and cellular cardiology* 101 (2016): 26-34.

Smith, G.L. and Eisner, D.A., (2019). "Calcium buffering in the heart in health and disease." *Circulation*, 139(20), pp.2358-2371.

Soltis, Anthony R., and Jeffrey J. Saucerman. "Synergy between CaMKII substrates and β-adrenergic signaling in regulation of cardiac myocyte Ca^{2+} handling." *Biophysical journal* 99, no. 7 (2010): 2038-2047.

Sossalla, Samuel, Birte Kallmeyer, Stefan Wagner, Marek Mazur, Ulrike Maurer, Karl Toischer, Jan D. Schmitto et al. "Altered Na+ currents in atrial fibrillation: effects of ranolazine on arrhythmias and contractility in human atrial myocardium." *Journal of the American College of Cardiology* 55, no. 21 (2010): 2330-2342.

Stern, Michael D., Long-Sheng Song, Heping Cheng, James SK Sham, Huang Tian Yang, Kenneth R. Boheler, and Eduardo Ríos. "Local control models of cardiac excitation–contraction coupling: a possible role for allosteric interactions between ryanodine receptors." *The Journal of general physiology* 113, no. 3 (1999): 469-489.

Sutanto, Henry, and Jordi Heijman. "Integrative Computational Modeling of Cardiomyocyte Calcium Handling and Cardiac Arrhythmias: Current Status and Future Challenges." *Cells* 11, no. 7 (2022): 1090.

Sutanto, Henry, Aurore Lyon, Joost Lumens, Ulrich Schotten, Dobromir Dobrev, and Jordi Heijman. "Cardiomyocyte calcium handling in health and disease: Insights from in vitro and in silico studies." *Progress in Biophysics and Molecular Biology* 157 (2020): 54-75.

Swartz, Michael F., Gregory W. Fink, Charles J. Lutz, Steven M. Taffet, Omer Berenfeld, Karen L. Vikstrom, Kimberly Kasprowicz et al. "Left versus right atrial difference in dominant frequency, K+ channel transcripts, and fibrosis in patients developing atrial fibrillation after cardiac surgery." *Heart Rhythm* 6, no. 10 (2009): 1415-1422.

Taggart, Peter, and Peter MI Sutton. "Cardiac mechano-electric feedback in man: clinical relevance." *Progress in biophysics and molecular biology* 71, no. 1 (1999): 139-154.

Tanaami, Takeo, Hideyuki Ishida, Hidetaka Seguchi, Yuki Hirota, Toshie Kadono, Chokoh Genka, Hiroe Nakazawa, and William H. Barry. "Difference in propagation of Ca^{2+} release in atrial and ventricular myocytes." *The Japanese journal of physiology* (2005): 0504270003-0504270003.

Tavi, P., M. Laine, and M. Weckström. "Effect of gadolinium on stretch-induced changes in contraction and intracellularly recorded action-and afterpotentials of rat isolated atrium." *British journal of pharmacology* 118, no. 2 (1996): 407-413.

Tessier, Sophie, Peter Karczewski, Ernst-Georg Krause, Yves Pansard, Christophe Acar, Michel Lang-Lazdunski, Jean-Jacques Mercadier, and Stéphane N. Hatem. "Regulation of the transient outward K+ current by Ca^{2+}/calmodulin-dependent protein kinases II in human atrial myocytes." *Circulation research* 85, no. 9 (1999): 810-819.

Timmermann, Viviane, Lars A. Dejgaard, Kristina H. Haugaa, Andrew G. Edwards, Joakim Sundnes, Andrew D. McCulloch, and Samuel T. Wall. "An integrative appraisal of mechano-electric feedback mechanisms in the heart." *Progress in biophysics and molecular biology* 130 (2017): 404-417.

Trayanova, Natalia A., and John Jeremy Rice. "Cardiac electromechanical models: from cell to organ." *Frontiers in physiology* 2 (2011): 43.

Tsai, Chia-Ti, Fu-Tien Chiang, Chuen-Den Tseng, Chih-Chieh Yu, Yi-Chih Wang, Ling-Ping Lai, Juey-Jen Hwang, and Jiunn-Lee Lin. "Mechanical stretch of atrial myocyte monolayer decreases sarcoplasmic reticulum calcium adenosine triphosphatase expression and increases susceptibility to repolarization alternans." *Journal of the American College of Cardiology* 58, no. 20 (2011): 2106-2115.

Tsang, Teresa SM, Walter P. Abhayaratna, Marion E. Barnes, Yoko Miyasaka, Bernard J. Gersh, Kent R. Bailey, Stephen S. Cha, and James B. Seward. "Prediction of cardiovascular outcomes with left atrial size: is volume superior to area or diameter?." *Journal of the American College of Cardiology* 47, no. 5 (2006): 1018-1023.

Vagos, Márcia, Ilsbeth GM van Herck, Joakim Sundnes, Hermenegild J. Arevalo, Andrew G. Edwards, and Jussi T. Koivumäki. "Computational modeling of electrophysiology and pharmacotherapy of atrial fibrillation: recent advances and future challenges." *Frontiers in Physiology* 9 (2018): 1221.

Van der Velden, J., L. J. Klein, M. Van Der Bijl, M. A. J. M. Huybregts, W. Stooker, J. Witkop, L. Eijsman, C. A. Visser, F. C. Visser, and G. J. M. Stienen. "Isometric tension development and its calcium sensitivity in skinned myocyte-sized preparations from different regions of the human heart." *Cardiovascular research* 42, no. 3 (1999): 706-719.

Van Wagoner, David R., Amber L. Pond, Michelle Lamorgese, Sandra S. Rossie, Patrick M. McCarthy, and Jeanne M. Nerbonne. "Atrial L-type Ca^{2+} currents and human atrial fibrillation." *Circulation research* 85, no. 5 (1999): 428-436.

Varela, Marta, Aditi Roy, and Jack Lee. "A survey of pathways for mechano-electric coupling in the Atria." *Progress in Biophysics and Molecular Biology* 159 (2021): 136-145.

Verdonck, Fons, Kanigula Mubagwa, and Karin R. Sipido. "[Na+] in the subsarcolemmal 'fuzzy'space and modulation of $[Ca^{2+}]$i and contraction in cardiac myocytes." *Cell Calcium* 35, no. 6 (2004): 603-612.

Voigt, Niels, Jordi Heijman, Qiongling Wang, David Y. Chiang, Na Li, Matthias Karck, Xander HT Wehrens, Stanley Nattel, and Dobromir Dobrev. "Cellular and molecular mechanisms of atrial arrhythmogenesis in patients with paroxysmal atrial fibrillation." *Circulation* 129, no. 2 (2014): 145-156.

Voigt, Niels, Na Li, Qiongling Wang, Wei Wang, Andrew W. Trafford, Issam Abu-Taha, Qiang Sun et al. "Enhanced sarcoplasmic reticulum Ca^{2+} leak and increased Na+-Ca^{2+} exchanger function underlie delayed afterdepolarizations in patients with chronic atrial fibrillation." *Circulation* 125, no. 17 (2012): 2059-2070.

Wakili, Reza, Yung-Hsin Yeh, Xiao Yan Qi, Maura Greiser, Denis Chartier, Kunihiro Nishida, Ange Maguy et al. "Multiple potential molecular contributors to atrial hypocontractility caused

by atrial tachycardia remodeling in dogs." *Circulation: Arrhythmia and Electrophysiology* 3, no. 5 (2010): 530-541.

Walden, A.P., Dibb, K.M. and Trafford, A.W., 2009. "Differences in intracellular calcium homeostasis between atrial and ventricular myocytes." *Journal of molecular and cellular cardiology*, 46(4), pp.463-473.

Wang, G. X., R. Schmied, F. Ebner, and M. Korth. "Intracellular sodium activity and its regulation in guinea-pig atrial myocardium." *The Journal of Physiology* 465, no. 1 (1993): 73-84.

Wang, Zhiguo, Bernard Fermini, and Stanley Nattel. "Sustained depolarization-induced outward current in human atrial myocytes. Evidence for a novel delayed rectifier K+ current similar to Kv1. 5 cloned channel currents." *Circulation research* 73, no. 6 (1993): 1061-1076.

Weiss, James N., Alain Karma, Yohannes Shiferaw, Peng-Sheng Chen, Alan Garfinkel, and Zhilin Qu. "From pulsus to pulseless: the saga of cardiac alternans." *Circulation research* 98, no. 10 (2006): 1244-1253.

Wettwer, Erich, Ottó Hála, Torsten Christ, Jürgen F. Heubach, Dobromir Dobrev, Michael Knaut, András Varró, and Ursula Ravens. "Role of I_{Kur} in controlling action potential shape and contractility in the human atrium: influence of chronic atrial fibrillation." *Circulation* 110, no. 16 (2004): 2299-2306.

Wilhelms, Mathias, Hanne Hettmann, Mary M. Maleckar, Jussi T. Koivumäki, Olaf Dössel, and Gunnar Seemann. "Benchmarking electrophysiological models of human atrial myocytes." *Frontiers in physiology* 3 (2013): 487.

Workman, Antony J., Kathleen A. Kane, and Andrew C. Rankin. "Characterisation of the Na, K pump current in atrial cells from patients with and without chronic atrial fibrillation." *Cardiovascular research* 59, no. 3 (2003): 593-602.

Xie, Eric, Ricky Yu, Bharath Ambale-Venkatesh, Hooman Bakhshi, Susan R. Heckbert, Elsayed Z. Soliman, David A. Bluemke et al. "Association of right atrial structure with incident atrial fibrillation: a longitudinal cohort cardiovascular magnetic resonance study from the Multi-Ethnic Study of Atherosclerosis (MESA)." *Journal of Cardiovascular Magnetic Resonance* 22, no. 1 (2020): 1-10.

Xie, Lai-Hua, Daisuke Sato, Alan Garfinkel, Zhilin Qu, and James N. Weiss. "Intracellular Ca alternans: coordinated regulation by sarcoplasmic reticulum release, uptake, and leak." *Biophysical journal* 95, no. 6 (2008): 3100-3110.

Zabel, Markus, Bettina S. Koller, Frederick Sachs, and Michael R. Franz. "Stretch-induced voltage changes in the isolated beating heart: importance of the timing of stretch and implications for stretch-activated ion channels." *Cardiovascular research* 32, no. 1 (1996): 120-130.

Zhan, Heqing, and Ling Xia. "Excitation-contraction coupling between human atrial myocytes with fibroblasts and stretch activated channel current: a simulation study." *Computational and Mathematical Methods in Medicine 2013* (2013).

Zhan, Heqing, Jingtao Zhang, Anquan Jiao, and Qin Wang. "Stretch-activated current in human atrial myocytes and Na+ current and mechano-gated channels' current in myofibroblasts alter myocyte mechanical behavior: A computational study." *Biomedical engineering online* 18, no. 1 (2019): 1-15.

Zhang, Shanzhuo, Qince Li, Lufang Zhou, Kuanquan Wang, and Henggui Zhang. "Development of a novel Markov chain model for oxidative-dependent CaMKIIδ activation." *In 2015 Computing in Cardiology Conference (CinC)*, pp. 881-884. IEEE, 2015.

Zhao, Na, Qince Li, Haibo Sui, and Henggui Zhang. "Role of oxidation-dependent CaMKII activation in the genesis of abnormal action potentials in atrial cardiomyocytes: a simulation study." *BioMed research international 2020* (2020).

Zile, Melanie A., and Natalia A. Trayanova. "Increased thin filament activation enhances alternans in human chronic atrial fibrillation." *American Journal of Physiology-Heart and Circulatory Physiology* 315, no. 5 (2018): H1453-H1462.

Zile, Melanie A., and Natalia A. Trayanova. "Rate-dependent force, intracellular calcium, and action potential voltage alternans are modulated by sarcomere length and heart failure induced-remodeling of thin filament regulation in human heart failure: A myocyte modeling study." *Progress in biophysics and molecular biology* 120, no. 1-3 (2016): 270-280.